# STUDY ON REAL-TIME TSUNAMI INUNDATION, WAVEFORMS, AND WAVEFIELDS FORECASTING

**Ardiansyah Fauzi**

# STUDY ON REAL-TIME TSUNAMI INUNDATION, WAVEFORMS, AND WAVEFIELDS FORECASTING

Ardiansyah Fauzi

Supervised by
Prof. Norimi MIZUTANI

A THESIS SUBMITTED TO
THE FACULTY OF ENGINEERING
OF NAGOYA UNIVERSITY
IN PARTIAL FULFILMENT OF THE REQUIREMENTS FOR THE DEGREE OF
DOCTOR OF ENGINEERING

June 2020

# Abstract

The best method to forecast tsunami waveforms, inundation, and wavefields caused by a submarine earthquake is by conducting linear or non-linear tsunami simulation. However, these methods have the disadvantages of a relatively high computational cost and the necessity for immediate warning announcements when a tsunami is imminent. The main objective of this study is to forecast tsunami inundation, waveforms, and wavefields in a timely manner shortly after an earthquake occurs.

In the first part of this study, tsunami inundation is forecasted by utilizing a database. The method aims to provide tsunami inundation forecasts without conducting non-linear tsunami model. The database consists of tsunami inundation and waveforms from multiple fault scenarios. The system is divided into two stages. In the first stage, preliminary earthquake information is used to find the appropriate tsunami inundation scenario in the database. In the second stage, a real-time tsunami waveform simulation is conducted to find the best-case scenario by minimizing the error between computed tsunami waveforms and those in database. Furthermore, this method is able to produce good tsunami inundation forecasts in a reliable time.

The second part of this study involves machine learning algorithms for tsunami inundation forecasting. Two machine learning models, a convolutional neural network and a multilayer perceptron, are used to estimate tsunami inundation in real-time. Non-linear tsunami simulation from same fault scenarios as mentioned in the first part of this study is conducted. The result of the maximum tsunami amplitude in a low-resolution grid and the associated tsunami inundation in a high-resolution grid are then stored in the database. The convolutional neural network selects tsunami inundation in the high-resolution grid as the forecast based on pattern similarity between the input, which is the results of linear forward modeling in the low-resolution grid, and the precomputed patterns in

the database. Slightly different from the convolutional neural network, instead of selecting the best-fit scenario in the database, the multilayer perceptron directly generates the inundation forecast based on knowledge acquired during the training process. The methods have been conducted by using the hypothetical future Nankai megathrust earthquake with Atashika and Owase Bays in Japan as the study cases. The results show that the proposed methods are extremely fast (less than 1 s) and comparable with nonlinear forward modeling. Therefore, the proposed methods can be used as a deterministic model for real-time simulation.

In the third part of this study, the performance of three data-driven models, including unfine- and fine-tuned probabilistic regularized extreme learning machines, and a support vector machine are examined to forecast tsunami waveform at coastal stations in real-time. The proposed methods are applied to an experimental case with the 2004 Kii (M7.5) and the 2011 Tohoku earthquake (M9.0). The results show that a fine-tuned probabilistic regularized extreme learning machine can produce better prediction accuracy compared to the conventional tsunami waveform inversion and the other data-driven models with quick calculation time. The support vector machine is also a promising method as the maximum tsunami height prediction is closer to the observation than the other models. Furthermore, the proposed data-driven models are also compared with a conventional waveform inversion, and the results show that the proposed models provide a better general approximation. Therefore, the proposed methods can be used as a surrogate for the deterministic model for real-time computation. Furthermore, our proposed methods produce a consistent prediction which is an important factor for the real-time warning system.

The last part of this study is integrating a deep predictive coding network with the data assimilation method. Unlike the original data assimilation, which continuously compute the wavefield when the observed data is available, this study only use a short sequence of the previously assimilated wavefields to forecast the future wavefields. Since the predictions are computed through matrix multiplication, the future wavefields can be estimated in seconds. The proposed method is applied to the simple bathymetry case and the 2011 Tohoku tsunami. The results show that the proposed method is very fast and comparable to the original data assimilation. Therefore, the proposed method is promising to be integrated with the data assimilation to reduce the computational cost.

# Acknowledgement

Firstly, I would like to express my deepest gratitude to my academic advisor, Prof. Norimi Mizutani, for his guidance, assistance, and advice throughout my study period at Nagoya University. It is such a honor to be allowed to join his laboratory and to work with one of leaders in the field of coastal engineering.

I would also like to thank the committee members, Assoc. Prof. Tomoaki Nakamura, Prof. Yuji Toda, Prof. Takashi Tomita, and Prof. Yasuhiro Suzuki for their valuable feedback and critics which improves the quality of the dissertation. I thank Asst. Prof. Cho Yong-Hwan for his assistance in many things during the research period.

In addition, I would like to thank the Forefront program's staff, Mrs. Hiroko Kawahara, for her assistance during my initial life in Nagoya. I also thank to the members of the Coastal and Ocean Engineering laboratory: Dr. Kim Shin-Woong (currently a research professor at Halla University, South Korea) for his help related to the research work as well as daily life, Kanta Yamamoto, Kana Hibino, Rei Akahoshi, Hiroyuki Watanabe, Long Rui, Zhang Chu, and Wataru Anzai for making my initial life in Nagoya, especially at laboratory, fruitful. Finally, I would like to thank my wife and sons who sacrifice their time far from home to accompany my study at Nagoya University.

This study is conducted under the financial support provided by the Ministry of Education, Culture, Sports, Science and Technology (MEXT).

# Declaration

I hereby certify that the work presented in this dissertation is the result of my own research during the PhD research. Text and results obtained from other sources are referenced and properly acknowledged.

*Ardiansyah Fauzi*
*July 2020*

# Table of Contents

# List of Figures

# List of Tables

# List of Abbreviations

| | |
|---|---|
| **CNN** | Convolutional Neural Network |
| **ConvLSTM** | Convolutional Long-Short Term Memory |
| **CPU** | Central Processing Unit |
| **DA** | Data Assimilation |
| **DART** | Deep-ocean Assessment and Reporting Tsunami |
| **ELM** | Extreme Learning Machine |
| **ELU** | Exponential Linear Unit |
| **GEBCO** | General Bathymetric Chart of the Ocean |
| **GPS** | Global Positioning System |
| **JAMSTEC** | Japan Agency for Marine Earth Science and Technology |
| **JMA** | Japan Meteorological Agency |
| **KKT** | Karush-Kuhn-Tucker |
| **LLW** | Linear Long-Wave |
| **MLIT** | Ministry of Land, Infrastructure, Transport and Tourism |
| **MLP** | Multilayer Perceptron |
| **MOST** | Method of Splitting Tsunami |
| **NearTIF** | Near-field Tsunami Inundation Forecasting |
| **NN** | Neural Network |
| **NIED** | National Research Institute for Earth Science and Disaster Prevention |
| **OBP** | Ocean Bottom Pressure |
| **PARI** | Port and Airport Research Institute |
| **PRELM** | Probabilistic Regularized Extreme Learning Machine |

| | |
|---|---|
| **PRELM-FT** | Probabilistic Regularized Extreme Learning Machine Fine-Tuned |
| **RELU** | Rectified Linear Unit |
| **RBF** | Radial Basis Function |
| **RMSE** | Root Mean Square Error |
| **RTK** | Real Time Kinematic |
| **SSIM** | Structural Similarity Index Measurement |
| **SVM** | Support Vector Machine |
| **TEWS** | Tsunami Early Warning System |
| **TUNAMI** | Tohoku University's Numerical Analysis Model for Investigation of near-field tsunami |
| **TWI** | Tsunami Waveform Inversion |
| **USGS** | United States Geological Survey |

# Chapter 1

# Introduction

## 1.1 Background

Tsunami is one of the most disastrous natural events in the world. Unlike the other natural disasters, the tsunamis have a tremendous impact on the loss of lives, property damages, and economic disruption. In 2004, a strong earthquake with a magnitude of about Mw 9.0∼9.3 (Lay et al., 2005) called Sumatra-Andaman earthquake, generated the most powerful tsunami ever recorded in human history. The tsunami caused a great loss of property and human lives. From ∼280,000 confirmed fatalities which spreads in South and South East Asian, and African countries, ∼250,000 fatalities were only in Indonesia. Another significant tsunami, the 2011 Tohoku tsunami, which is the most powerful earthquake recorded in Japanese history, caused more than 20,000 people died and missing, destroyed 126,602 buildings and caused economic damage of $ 210 billion (Ranghieri, 2014). One of the reasons why tsunamis are incredibly destructive, other than because of their power, tsunamis are difficult to predict. Before the 2011 Tohoku earthquake event, most tsunami warning systems are depending on the earthquake prediction and integrated with the earthquake forecasting system. Since there is a high degree of uncertainty in predicting earthquake sources in real-time, it also results in the inaccuracy of tsunami prediction.

After the 2011 Tohoku earthquake, the attention of many earthquakes and tsunamis researchers is moved to the Nankai region for a possible future megathrust earthquake. The Nankai Trough is one of the most active subduction zones in the world. Many massive submarine earthquakes have been generated and well

recorded in this region. Based on historical records, Ishibashi (2004) showed that earthquakes in this zone have a recurrence interval between 100 and 150 years. Five major earthquakes in the Nankai Trough have been identified (see Fig. 1.1): the 1707 Hoei earthquake, the 1854 Ansei Tokai and Ansei Nankai earthquakes, the 1944 Tonankai earthquake, and the 1946 Nankai earthquake. Among those earthquakes, the 1707 Hoei event marked the strongest earthquake in the preindustrial history of Japan, and a giant tsunami followed it. Three main fault segments are in this region: the Tokai, the Tonankai, and the Nankai. In those historical earthquakes, the three segments ruptured individually or simultaneously. In the future, it is expected that the three segments will rupture simultaneously and generate a massive earthquake. Because the Nankai Trough is relatively close to the coast of southeastern Japan (less than 150 km away), if the earthquake induces a tsunami, it will reach the coast in a very short time. Therefore, a fast and robust tsunami early warning system is required to prevent large casualties caused by Nankai Trough earthquakes in the future.

Over the last decades, the development of the real-time tsunami warning system has been advancing, as a derivative of the rapid development of computational technologies. Various numerical modeling frameworks have been developed in the past (Baba et al., 2016, Imamura et al., 2006, Titov et al., 2016) and still become the main tools to assess the impact caused by the tsunamis. However, since those methods require a relatively high computational load, especially for real-time simulation, a novel method is badly needed to cut the computational cost. Recently, machine learning algorithms gain popularity not only in the computer science field but also in the other field. Unfortunately, the application of such frameworks is limited in tsunami research. This study presents methods to predict tsunami inundation, waveforms, and wavefields. Those three goals are examined by using different approaches. Tsunami inundation prediction is divided into two parts, one of them using machine learning frameworks. Furthermore, both tsunami waveform and wavefield predictions are assessed by using different types of machine learning frameworks. Even though those proposed methods are evaluated by using different frameworks, the basis of the algorithms are similar, all of those goals are utilizing database which consists of precomputed simulation from multiple scenarios. In this study, convolutional neural network (CNN) and multilayer perceptron (MLP) are used to forecast tsunami inundation, extreme learning machine (ELM) and support vector machine (SVM) are used to forecast tsunami waveform, and finally a deep predicting coding network is used to predict tsunami wavefield.

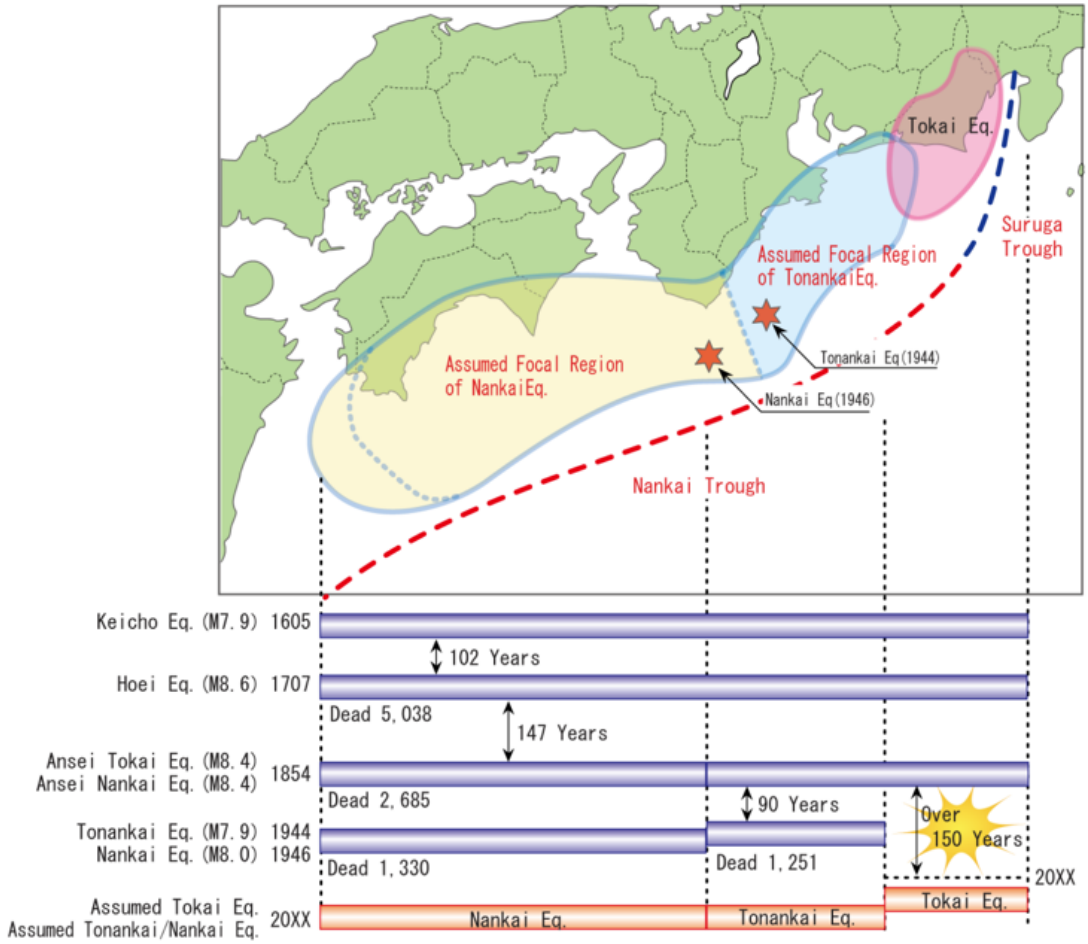


Figure 1.1: Past earthquakes in Nankai Subduction zone (Source: `http://www.jma.go.jp/jma/en/Activities/earthquake.html` accessed on June 1st, 2018)

## 1.2 Objectives

The primary objective of this study is to forecast tsunami inundation, waveforms, and wavefields promptly after a submarine earthquake occurs. In this study, several previous earthquakes in the Nankai and Japan trench region, namely, the 1944 Tonankai, the 2004 Nankai, the 2011 Tohoku, the predicted future Nankai megathrust earthquakes are used as study cases.

This study is conducted with the following motivations. First, this study attempts to reduce the computational time of the previous methods in forecasting tsunami. Many studies have been proposed; however, most of them still require a high computational cost. To accommodate this problem, a high-performance computer is usually used to speed up the computational time. However, with the limited availability of such facilities, espescially in developing countries, a light yet reliable tsunami warning system is preferable.

Second, this study attempts to develop a new approach that can be used as an alternative to forecast tsunami, which has similar performance to the deterministic model. Currently, the best method to predict tsunami is by running a linear and/or non-linear tsunami model. However, a high computational cost is generally required, as mentioned in the first objective. In this study, several methods are evaluated and compared with the conventional tsunami simulation. The proposed are trained by using the results of the tsunami model. Hence, it is acknowledged these new methods to be applied for real-time tsunami forecasting.

## 1.3 Limitations of the study

In many parts of this study, the initial sea surface caused by earthquake-generated seafloor deformation is used. However, this study doesn't consider the complex behaviour of the seafloor deformation. The seafloor deformation in this study is calculated from a well-verified model (Okada, 1985) and assummed as the initial sea surface elevation for tsunami simulation.

## 1.4 Thesis outline

Chapter 1 explains the background of the study, motivations, objectives, and the expected outputs of the study. A brief literature review is also explained, as a more detailed review will be shown at the beginning of the each later chapter.

Chapter 2 discusses the first attempt to forecast tsunami inundation in real-time by using a database. Mie and Aichi Prefecture are selected as the study case of the study. The development of the tsunami inundation and waveform database are presented in this chapter. At the first stage of warning, the system only requires the location of the earthquake to extract tsunami inundation from the database as the forecast. When a fixed earthquake information is available, the prediction is improved by comparing simulated and precomputed waveforms at virtual observation stations to find out the best-fit scenario in the database.

Chapter 3 is an extension of Chapter 2. In this chapter, tsunami inundation database as in Chapter 1 is used. There are two proposed machine learning frameworks in this study, the CNN and MLP. CNN is proposed to replace the second stage of the warning system in Chapter 2. At the same time, the MLP

is used to directly generate the tsunami inundation forecast based on learned knowledge during the training process.

Chapter 4 discusses the application of the ELM and SVM for tsunami waveform prediction. The performance of both methods are compared to the conventional tsunami waveform inversion (TWI). Unlike the traditional ELM in which parameters the first layer of the network is determined randomly, in this study, are trained by using the backpropagation approach to reduce the model uncertainty.

Chapter 5 presents an algorithm, a deep predictive coding network, for spatiotemporal prediction of tsunami wavefield. The method is proposed to cut the computational time required by tsunami data assimilation. Various statistical measures are conducted to evaluate the performance of the model.

Chapter 6 presents the conclusions of this study. Detail summary for each chapter (Chapter 2, Chapter 3, Chapter 4, and Chapter 5) is also presented.

# References

Baba, T., Ando, K., Matsuoka, D., Hyodo, M., Hori, T., Takahashi, N., Obayashi, R., Imato, Y., Kitamura, D., Uehara, H., Kato, T., and Saka, R. (2016). Large-scale, high-speed tsunami prediction for the Great Nankai Trough Earthquake on the K computer. *International Journal of High Performance Computing Applications*, 30(1):71–84.

Imamura, F., Yalçiner, A. C., and Ozyurt, G. (2006). Tsunami modelling manual. *Tsunami Modelling Manual*.

Ishibashi, K. (2004). Status of historical seismology in Japan. *Annals of Geophysics*, 47(2-3):339–368.

Lay, T., Kanamori, H., Ammon, C. J., Nettles, M., Ward, S. N., Aster, R. C., Beck, S. L., Bilek, S. L., Brudzinski, M. R., Butler, R., Deshon, H. R., Ekström, G., Satake, K., and Sipkin, S. (2005). The great Sumatra-Andaman earthquake of 26 December 2004.

Okada, Y. (1985). Surface deformation due to shear and tensile faults in a half-space. *Bulletin of the Seismological Society of America*, 75(4):1135–1154.

Ranghieri, F. (2014). Learning from megadisasters: Lessons learnt from the great

east Japan earthquake and tsunami. *Economics and Policy of Energy and the Environment*.

Titov, V., Kânoğlu, U., and Synolakis, C. (2016). Development of MOST for Real-Time Tsunami Forecasting. *Journal of Waterway, Port, Coastal, and Ocean Engineering*, 142(6).

# Chapter 2

# Database-based tsunami inundation forecasting

## 2.1 Problem description

The 2011 Tohoku earthquake left more than 15,000 people dead or missing (Kazama and Noda, 2012). It was the biggest earthquake followed by a tsunami ever recorded in Japanese history. Tsunami warnings and advisories were issued for areas along the coast of Hokkaido to Kyushu and the Ogasawara Islands (Ozaki, 2011). The Japan Meteorological Agency (JMA) estimated that the initial earthquake magnitude was Mjma 7.9, obtained within three minutes after the earthquake. Then, it was revised to be Mjma 8.4 in more than an hour after the earthquake (Ohta et al., 2012). Further study revealed that those magnitudes underestimated the actual earthquake magnitude of Mw 9.0 (Gusman et al., 2012, Satake et al., 2013).

On the basis of experiences during the 2011 Tohoku tsunami and the possibility of a tsunami generated by a future great interplate earthquake of the Nankai Trough, a robust and accurate tsunami inundation forecast system is required. Tang et al. (2008) developed a tsunami forecast model for the Pacific and Atlantic coasts by using a tsunami source function database. DART (Deep-ocean Assessment and Reporting of Tsunami) data were used as the main input of the system. When an earthquake occurred, the data obtained from DART were used to compute a tsunami source for real-time tsunami simulation. Abe and Imamura (2012) applied a tsunami inundation database for a tsunami inundation forecast-

ing system in the case of the 2011 Tohoku earthquake. Real-time tsunami height information obtained from GPS buoys was used as an additional constraint to produce an accurate inundation forecast. However, because of the limited number of GPS buoys, when a GPS buoy is located far from the forecasted area, it may produce the wrong inundation forecast. Similar to the study of Abe and Imamura (2012), Tomita and Takagawa (2014) enhanced the system by utilizing a graphic processing unit to quickly estimate tsunami propagation and inundation. Gusman et al. (2014) proposed a new real-time tsunami inundation forecast system called NearTIF (Near-field Tsunami Inundation Forecasting), also with the study case of the 2011 Tohoku earthquake. This system uses a database that consists of a tsunami inundation map and tsunami waveform at the virtual comparison points. The database was developed by assuming a number of hypothetical thrust-type earthquake scenarios in a subduction zone. Van Veen et al. (2014) implemented an early warning system in Sumatra called RiskMap. This system was also constructed based on 1,250 hypothetical earthquake locations. This system was purposed not only to produce tsunami inundation forecast but also to warn residents by turning on sirens for the warning and evacuation process. Those previous studies have a similar assumption in developing their database; they assume simple fault model scenarios as tsunami sources and compute them by solving a nonlinear shallow water equation. The method proposed by Tang et al. (2008) may be suitable for far-field tsunamis in which DARTs are located far from the coast, while the methods proposed by Abe and Imamura (2012), Gusman et al. (2014) and Van Veen et al. (2014) are more appropriate for near-field tsunamis, as their methods utilize an observational system that is close to the coast. Earthquake information is not necessary for the method of Gusman et al. (2014) but is still required for the other methods. Oishi et al. (2015) conducted direct tsunami numerical simulation by using the K supercomputer, one of the most powerful supercomputers in the world, which is installed at the RIKEN Advanced Institute for Computational Science, Kobe, Japan. It requires only 1.5 minutes to obtain accurate tsunami inundation in Sendai City.

From those previous studies, it can be concluded that there are two main types of tsunami inundation forecasting systems: those that utilize a database and those that conduct direct numerical forward modeling. For direct forward modeling, a high-performance computer or supercomputer is usually used to shorten computational time. But access to the government supercomputer is limited, and there are difficulties using the supercomputer itself, especially in a real event. By using a database, government agencies in developing countries with limited equipment can develop their own systems easily. Simulated tsunami inundation from

hypothetical earthquake scenarios is widely used as a main part of the database.

The basic concept of our forecasting system using a database is a combination of those from previous studies: when an earthquake occurs, the system will find the nearest position between the actual earthquake coordinate and scenarios in the database as similarly used by Van Veen et al. (2014) and Abe and Imamura (2012) for the initial stage. This stage is expected to be essential for the early warning and evacuation process. Additionally, we apply the assumption proposed by Gusman et al. (2014) for the next stage in which if different earthquakes produce similar tsunami waveforms near the coastal area, they will produce similar tsunami inundation. Therefore, our database not only consists of tsunami inundation but also tsunami waveform.

Owase is one of the cities in Mie Prefecture, located in the southeastern Kii Peninsula, directly facing the Pacific Ocean (Fig. 2.1). Many regional and interregional tsunamis that have severely damaged the city have been recorded. The tsunami sources mostly came from off the Kii Peninsula, which is usually called the Tonankai segment. In 1960, a far-field Chilean tsunami also hit Owase with a maximum inundation depth of about 1 m (Hatori et al., 1981). Because it experienced many destructive tsunamis, and previous tsunami inundation depth data were available, this city was selected as a study case in this study. Here, we evaluate the performance and applicability of a tsunami inundation forecast system by using a database in Owase, Mie Prefecture, as it is expected to be one of the most damaged areas in the event of a future Nankai Trough earthquake. One previous earthquake and two predicted future earthquake scenarios are used for evaluation. The results of the tsunami inundation forecast then compared with the observation field data and forward modeling.

## 2.2 Methodology

The hydrodynamics characteristics and behavior of onshore tsunami are strongly influenced by nearshore bathymetry and tsunami waveform. Tsunami height and period in the nearshore strongly affected the result of inundation on the land. Various tsunami numerical models have been developed, such as, Method of Splitting Tsunami (MOST) (Titov et al., 2016) and the Tohoku University's Numerical Analysis Model for the Investigation of Near–field tsunamis (TUNAMI) (Imamura et al., 2006). Even though each other of the numerical models are rela-

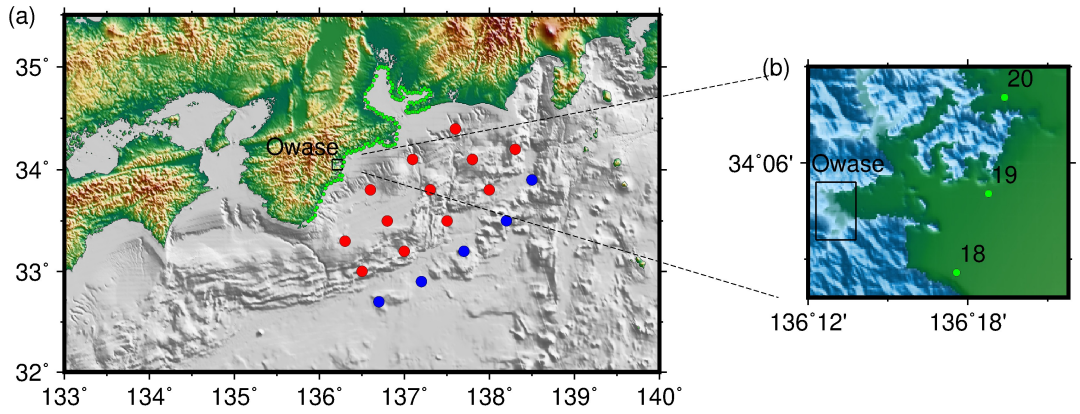


Figure 2.1: (a) Location of hypothetical earthquake scenarios for database. Red circles indicate the coordinate of earthquake epicenter for thrust-type and "tsunami earthquake" scenarios. Blue circles indicate the coordinate of earthquake epicenter for reverse-type scenarios. Small green circles along the coast indicate the location of virtual comparison points. The outermost boundary shows computational domain A (coarsest grid) and the black rectangle shows computational domain D (finest grid). (b) The black rectangle indicates the location of Owase. Virtual comparison point number 18, 19, and 20 are shown as a green circle.

tively different, but some of the results of tsunami inundation are closely similar. Based on this characteristic, it is assumed that if different earthquakes produce similar waveform in nearshore region, then they would produce similar tsunami inundation. Following this assumption, a real-time tsunami inundation forecast system by using database is developed. The database is made up of precomputed tsunami inundation and tsunami waveforms from multiple hypothetical earthquake sources. The earthquake information such as earthquake location, depth, and magnitude are still needed in the system. Once the earthquake information is available, a real-time tsunami waveform simulation can be done. By minimizing the root mean square error (RMSE) between the simulated tsunami waveform and the pre-computed tsunami waveform in the database, a site-specific scenario can be obtained. Then, the tsunami inundation from the selected scenario can be assumed as the tsunami inundation forecast.

The real-time tsunami inundation forecast system is divided into two stages. The details of each stage are explained below as well as in Fig. 2.2.

- Stage 1: When an earthquake occurs, preliminary earthquake information (earthquake coordinate, magnitude, and depth) will be available shortly and can be accessed in JMA or the U.S. Geological Survey (USGS) bulletin.

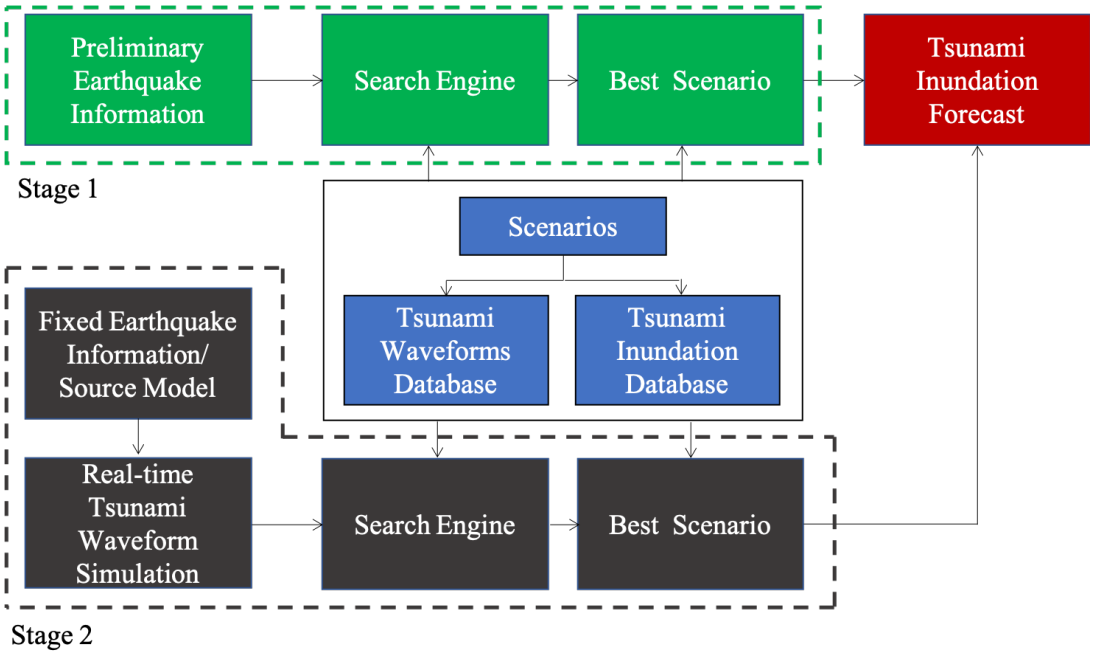


Figure 2.2: Flowchart of the proposed system

This information then is used as input for Stage 1. In this stage, the system will find coordinates and round up the magnitude to the nearest scenario in the database and then select the corresponding tsunami inundation as the tsunami inundation forecast. This stage can be repeated until fixed earthquake information or the tsunami source becomes available.

- Stage 2: Once the fixed earthquake information or tsunami source becomes available (e.g., through W-phase or tsunami waveform inversion), a real-time tsunami waveform simulation by solving a linear shallow water equation can be done. The results of the tsunami waveform simulation at virtual comparison points are then compared with the precomputed tsunami waveform in the database. The system will search and select a tsunami inundation forecast by minimizing RMSE between a real-time tsunami waveform and a precomputed tsunami waveform. If tsunami inundation forecasts from this stage are different from those of Stage 1, then tsunami inundation forecasts from Stage 1 are replaced with those from this stage. In some cases, the wave period of the simulated tsunami waveform and precomputed tsunami waveform are significantly different. To avoid this problem and to obtain a reliable tsunami inundation scenario in the database, a time shift method is applied. This method is adopted from Gusman et al. (2014) and proven to be effective in order to find appropriate scenario in database. For example, if two similar waveforms have different wave-phase, the resulted RMSE between those two waveforms will be high. Therefore, the

waveforms need to be manually shifted in time domain to produce a more reasonable misfit results. During the 2011 Tohoku earthquake and tsunami, JMA failed to catch reliable fixed earthquake information as a result of the magnitude threshold in the JMA system. This happened because, previously, Japan had no experience with earthquakes of magnitudes more than Mw 8.5. However, USGS could provide fixed and accurate earthquake information in 20 min after the earthquake, whereas JMA required 134 min (Goda and Abilova, 2016). Now, JMA has modified its system, and Stage 2 is expected to be conducted at less than 20 min after earthquake.

### 2.2.1 Bathymetry and topography data

Various studies explained the importance of high-resolution bathymetric and topographic data for assessment of tsunami (e.g. Mofjeld et al., 2001, Tang et al., 2008). The bathymetry, topography, and levee elevation data in the spherical coordinate system covering the coastal area in Mie and Aichi Prefectures were obtained from the G-Spatial Information Center of Japan. Then, the levee elevation data were integrated to the topography and bathymetry data for the input of tsunami simulation. The combination of these data was divided into four grid sizes: 30 arc-sec for domain A as the coarsest grid, 10 arc-sec for domain B, 3.33 arc-sec for domain C, and 1.11 arc-sec for domain D as the finest grid. Bathymetry and distribution of computational domains are shown in Fig 2.1a. For clarity, only computational domains applicable to Owase are shown.

### 2.2.2 Fault model scenarios

A tsunami inundation and waveform database is constructed from hypothetical earthquake scenarios. Earthquake models from those scenarios are assumed as simple rectangular fault models. The mechanism of an earthquake-induced tsunami within the Nankai Trough usually can be explained by using thrust fault mechanism. However, further study revealed that the other fault mechanisms could have possibly occurred in the Nankai Trough zone. Satake (2015) believed that the 1605 Keicho earthquake, with its source near the Nankai Trough axis, was a “tsunami earthquake,” because it generated a considerably large tsunami, yet no groundbreaking records were documented. A number of high-angle thrust-faulting earthquakes were also observed in the outer-rise region of the Nankai

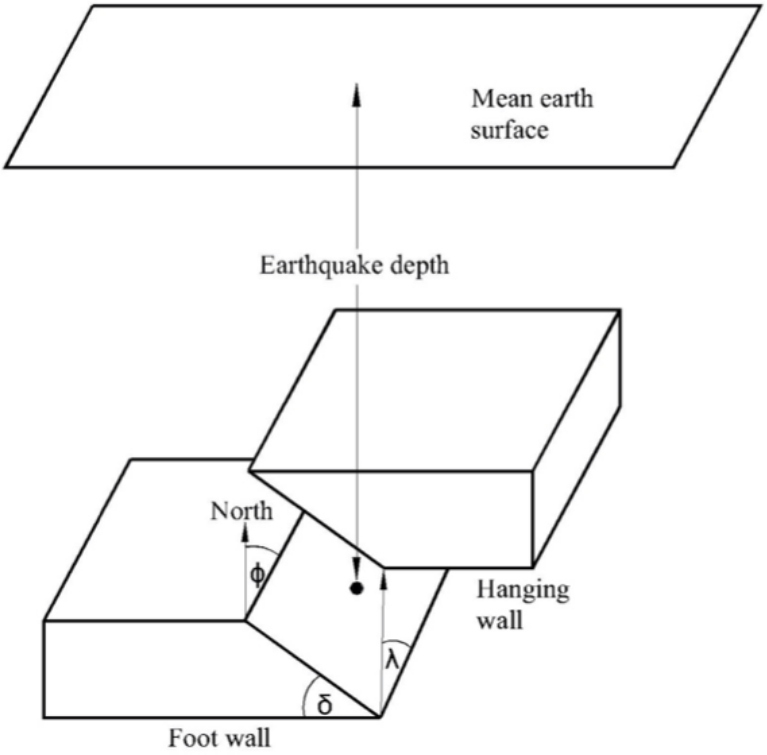


Figure 2.3: Rectangular fault model. Black dot represent the hypocenter of earthquake

trough with relatively shallow depth (Craig et al., 2014). Three types of fault model scenarios are used in this study—thrust fault, reverse fault, and tsunami earthquake—to accommodate all possibilities of fault mechanism in the Nankai Trough zone. Thrust fault and tsunami earthquake types are located on the plate interface of the Nankai Trough, and the reverse fault is located in the outer-rise region. For one site, there are 72 scenarios of the thrust fault mechanism, 96 scenarios of the tsunami earthquake type, and 160 scenarios of the reverse fault mechanism. Detail explanation of rectangular fault model is shown in the Fig. 2.3. The strike angle ($\phi$) of 225° is applied in all scenarios as an average strike angle in the Nankai Trough subduction zone, and the rake angle ($\lambda$) is set to 90° as an ideal degree for a subduction tsunami. Slab1.0 (Hayes et al., 2012), a slab model for subduction zone, is used to determine the dip angle ($\delta$) for thrust fault scenarios, whereas $\delta$ = 10° is used for the tsunami earthquake type and $\delta$ = 45° for the reverse fault scenarios. Slab1.0 is also used to determine the fault depth for thrust fault and tsunami earthquake scenarios. In the Slab1.0 model, previous earthquake depths are relatively similar to slab depth Fig. 2.4; therefore slab depth is to be assumed to be the depth of the earthquake. For the reverse fault type, fault depth ranges from 5 to 20 km, based on a previous study that the depth of outer-rise earthquakes ranged from 6 to 18 km (Craig et al., 2014).

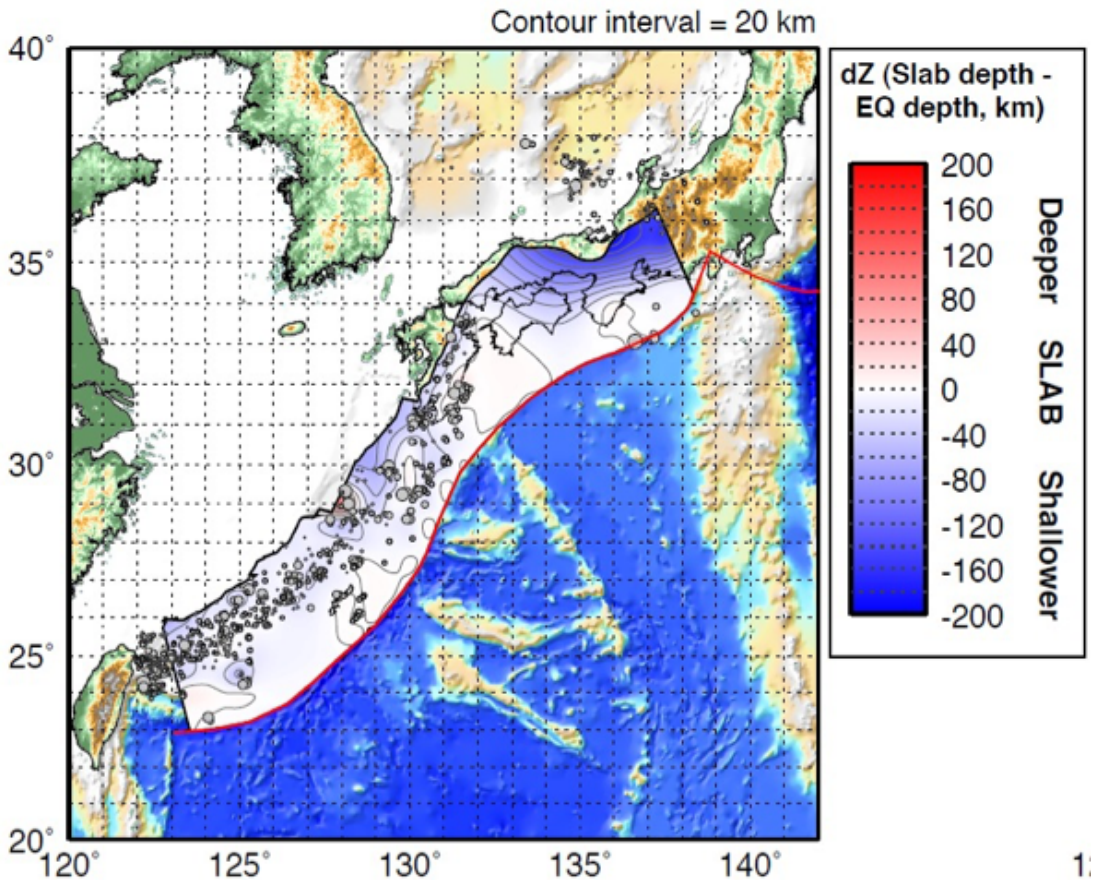


Figure 2.4: A comparison between the depth of earthquakes and the average depth of earthquakes (Source: Hayes et al. (2012))

Earthquakes of magnitude Mw 8.0–9.0 are selected for the thrust fault type and 7.0–8.4 for tsunami earthquake and reverse fault–type scenarios (Table 2.1). In this study the depth of the earthquake/fault is placed in the middle of a rectangular plane to accommodate the fault centroid depth, whereas most previous studies placed the earthquake depth at the top center edge of the fault plane. The locations of hypothetical earthquakes are selected by following the characteristics of the Nankai Trough subduction zone (Fig. 2.1a).

Table 2.1: Fault parameters of earthquake scenarios

| **Fault type** | **Magnitude** ($M_w$) | **Depth** (km) | **Strike** (°) | **Dip** (°) | **Rake** (°) |
|---|---|---|---|---|---|
| Thrust | 8.0-9.0 | SLAB1.0 | 225 | SLAB1.0 | 90 |
| Tsunami earthquake | 7.0-8.4 | SLAB1.0 | 225 | 10 | 90 |
| Reverse | 7.0-8.4 | 5,10,15,20 | 225 | 45 | 90 |

To calculate the size of the fault plane, a magnitude scaling relation is used.

Several magnitude scaling relations have been developed and tested in previous research. Wells and Coppersmith (1994), Hanks and Bakun (2002), and Blaser et al. (2010) developed widely used scaling relations. Gusman et al. (2015) concluded that the Hanks and Bakun relation was the most appropriate relation to represent the major slip for the 2011 Tohoku tsunami. In this study, the scaling relation for the plate-boundary earthquake (Eq. 2.1) by Murotani et al. (2013) was used. This scaling relation was originally developed by utilizing 26 plate-boundary earthquakes with magnitudes ranging from Mw 6.7 to Mw 8.8 Murotani et al. (2008) and modified by adding seven giant earthquakes (Mw ∼9.0). This scaling relation was tested to be able to explain the fault size of earthquakes in the Nankai Trough region.

$$S = 1.34 \times 10^{-10} M_o^{2/3} \tag{2.1}$$

where $S$ is the rupture area (in kilometers squared) and $M_o$ is the seismic moment (in Newton meters). Length and width of the fault plane can be directly derived from the scaling relation by using a simple relationship where the length is equal to twice the width. However, for the tsunami earthquake type, fault width is typically much shorter than fault length. Hence, fault width is assumed to be less than 50 km for tsunami earthquake scenarios Tanioka and Satake (1996).

### 2.2.3 Tsunami inundation and waveform database

The tsunami inundations and waveforms in the database are simulated by solving a nonlinear shallow water equation on a staggered grid leap-frog scheme (Gusman et al., 2009). Spherical coordinate system is used to calculate tsunami propagation with the origin at the Earth's center. By assuming the Earth is to be a sphere, $r$ is constant and equal to the Earth's radius $R$. Latitude ($\theta$) and longitude ($\varphi$) is covering Earth sphere. The shallow water or the long wave theory is explained by the following equations:

$$\frac{\partial \eta}{\partial t} + \frac{1}{Rcos\theta}\left[\frac{\partial M}{\partial \varphi} + \frac{\partial N}{\partial \varphi}(cos\theta)\right] = 0 \tag{2.2}$$

$$\begin{aligned}\frac{\partial M}{\partial t} + \frac{1}{Rcos\theta}\left[\frac{\partial}{\partial \varphi}\left(\frac{M^2}{D}\right) + \frac{\partial}{\partial \theta}\left(\frac{MN}{D}\right)cos\theta\right] = \\ fN - \frac{gD}{Rcos\theta}\frac{\partial \eta}{\partial \varphi} - \frac{C_f}{D^2}M\sqrt{M^2+N^2}\end{aligned} \tag{2.3}$$

$$\begin{aligned}\frac{\partial N}{\partial t} + \frac{1}{Rcos\theta}\left[\frac{\partial}{\partial \varphi}\left(\frac{MN}{D}\right) + \frac{\partial}{\partial \theta}\left(\frac{N^2}{D}\right)cos\theta\right] = \\ fM - \frac{gD}{R}\frac{\partial \eta}{\partial \theta} - \frac{C_f}{D^2}N\sqrt{M^2+N^2}\end{aligned} \tag{2.4}$$

The tsunami run-up heights and inundation are calculated by solving non-linear momentum conservation equation with bottom friction terms. By using analogy to the quadratic friction law in uniform flow, the bottom friction terms in the equation are explained. Then, the shallow water or the long wave theory in the Cartesian coordinate system is explained by the following expressions:

$$\frac{\partial M}{\partial t} + \frac{\partial}{\partial x}\left(\frac{M^2}{D}\right) + \frac{\partial}{\partial y}\left(\frac{MN}{D}\right) + gD\frac{\partial \eta}{\partial x} + \frac{C_f}{D^2}M\sqrt{M^2+N^2} = 0 \qquad (2.5)$$

$$\frac{\partial N}{\partial t} + \frac{\partial}{\partial x}\left(\frac{MN}{D}\right) + \frac{\partial}{\partial y}\left(\frac{N^2}{D}\right) + gD\frac{\partial \eta}{\partial y} + \frac{C_f}{D^2}N\sqrt{M^2+N^2} = 0 \qquad (2.6)$$

Manning's roughness coefficient $n$ is used to calculate the non-dimensional frictional coefficient $C_f = gn^2/D^{1/3}$. Constant $n$ value of 0.025 is applied homogeneously in the whole computational domain. In the equations, $M$ and $N$ are discharge fluxes along latitude and longitude axes, respectively, $t$ is the time, $\eta$ is the water level, $g$ is the gravitational constant, $D$ is the total water depth, and $f$ is the coefficient of Coriolis. The edge of computational domain is used as open boundary.

A moving boundary condition is applied to determine wet and dry cells for tsunami inundation. Calculation of discharge between two cells is done when elevation in the dry cell is lower than water level in the wet cell. Otherwise, the discharge will be defined as zero. A time step of 0.5 sec is used to satisfy the numerical stability condition. Manning's roughness coefficient of 0.025 is chosen and applied homogeneously for all domains. This Manning's roughness coefficient is widely used for tsunami simulation (Imamura, 2009). In this simulation, 134 virtual tsunami comparison points along the coastal area are selected (Fig. 2.1a). From these virtual comparison points, searching for the best-case scenario of tsunami inundation can be done. Tsunami simulation is conducted for 2 hours, and the results of the tsunami waveform at each virtual comparison point are then stored in the database as a precomputed tsunami waveform.

## 2.3 Results and discussion

To test the performance of the database, one previous earthquake, the 1944 Tonankai earthquake, is used as a tsunami source model. The slip distribution of that earthquake was estimated on small subfaults (10×10 km) by using the tsunami waveform inversion method (Baba and Cummins, 2005). And also two scenarios of expected future earthquakes, the Tokai–Tonankai and Nankai

Megathrust earthquakes, are used to test the capability of the database. The slip distributions of those earthquakes were obtained from G-Spatial Information Center of Japan (`https://www.geospatial.jp/gp_front/`). The Nankai Trough is divided into three major segments, which are the Tokai, Tonankai, and Nankai segments. For the Tokai–Tonankai earthquake model, the Tokai and Tonankai segments are assumed to rupture together. This scenario may represent the highest earthquake threat that would cause the most severe damage to Mie and Aichi prefectures. For the Nankai Megathrust earthquake model, the Tokai, Tonankai, and Nankai segments are assumed to be ruptured at the same time, making this the worst-case scenario of a Nankai Trough earthquake.

To calculate initial sea surface elevation for tsunami simulation, a surface deformation in an elastic half-space model (Okada, 1985) is used by utilizing parameters from those earthquake slip distributions (strike, slip, dip, rake, depth, length, and width). Sea surface deformation is assumed to be the same as seafloor deformation.

### 2.3.1 The 1944 Tonankai earthquake

Owase in Mie Prefecture is selected as a study case and virtual comparison point no. 19, which represents the nearest virtual comparison point chosen to find the best-case scenario in the database. For consistency of the results, we have chosen the three nearest virtual comparison points, and all of them produced the same results. Accordingly, only virtual comparison point no. 19 is selected in this study.

For the first stage, let us assume that preliminary earthquake information (earthquake magnitude and coordinate) is the same as fixed earthquake information. Then, by using this information, a scenario with similar earthquake magnitudes and coordinates is selected as the tsunami inundation forecast. Because there are two fault mechanism scenarios (thrust fault and tsunami earthquake) with the same coordinate, it is difficult to determine which scenario is more appropriate. This condition may be confusing in a real event in which a quick decision is needed, especially when many fault types and scaling relations are considered. However, in this case, the scenario from the tsunami earthquake fault type is selected as the tsunami inundation forecast because of larger inundation coverage (Fig. 2.5). The maximum depth of the tsunami inundation forecast obtained from stage 1 is about 5.5 m. The result strongly overestimates the field survey,

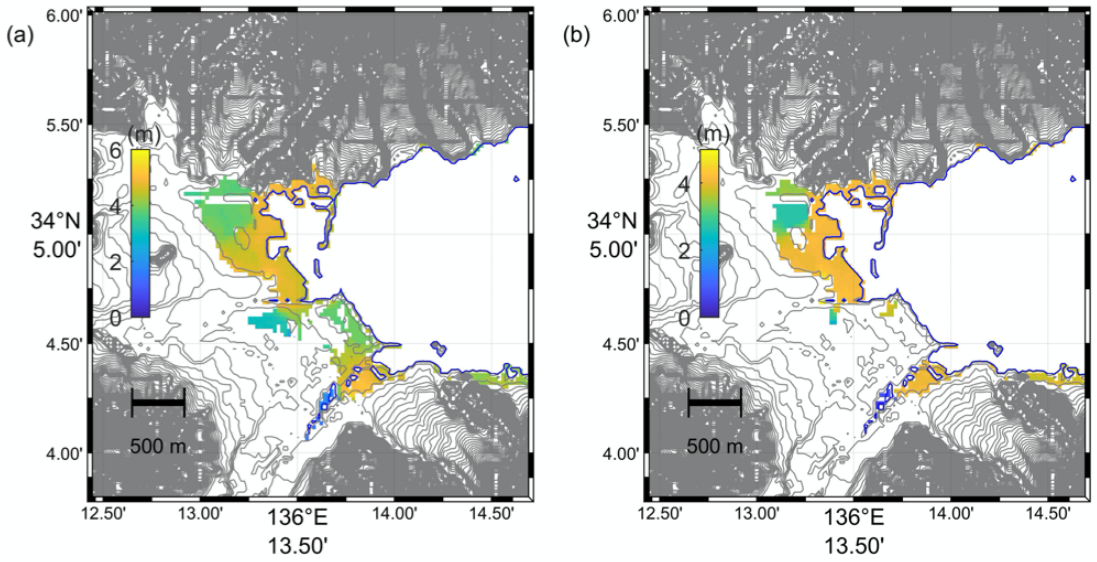


Figure 2.5: Tsunami inundation forecasts of the 1944 Tonankai earthquake case from stage 1 results: (a) a tsunami inundation forecast selected from the tsunami earthquake scenario; (b) a tsunami inundation forecast selected from the thrust scenario

where actual maximum tsunami inundation was 2.8 m (Hatori et al., 1981)(Fig. 2.6). This also shows that the forecast accuracy of tsunami inundation may be low even when using the same epicenter coordinate and earthquake magnitude as fixed earthquake information. Therefore, obtaining a reliable tsunami inundation forecast by using only earthquake coordinates and magnitudes is not sufficient.

Stage 2 can be performed when fixed earthquake information or a reliable tsunami source becomes available. By using earthquake information (magnitude, coordinate, depth, rake, dip, slip), a simple rectangular fault model can be assumed to create initial sea surface for real-time tsunami waveform simulation. To calculate the size of the fault plane, the same scaling relation as used in developing the tsunami inundation database can be used. A tsunami source model using a simple rectangular fault plane to calculate the real-time tsunami waveform is still included in this study by considering limited tsunami observational systems (e.g., GPS buoys) around the Tonankai segment, which is not sufficient to produce a reliable tsunami source by using more advanced methods, such as a waveform inversion. In a real event, if a more reliable tsunami source is available, it can be used to substitute the tsunami source from this simple rectangular assumption to simulate a real-time tsunami waveform. However, the tsunami source model obtained by Baba and Cummins (2005) is used in this experiment and assumed as a real tsunami source. The result of the simulated tsunami waveform is then

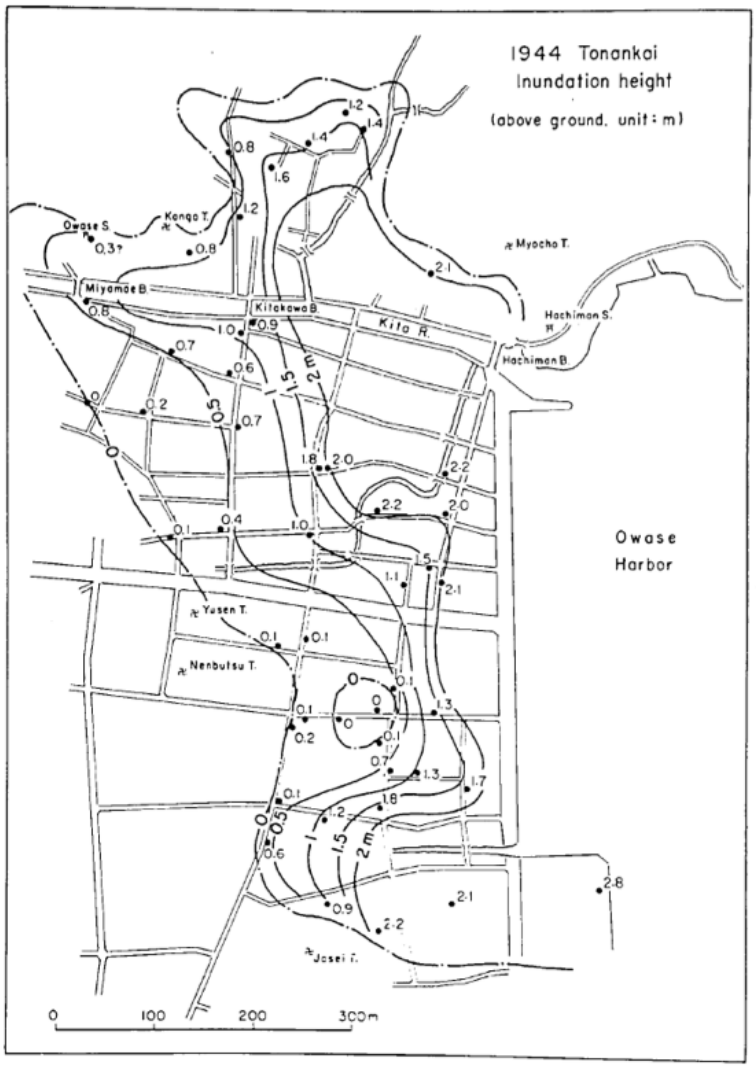


Figure 2.6: Tsunami inundation map from field survey in Owase City due to the 1944 Tonankai earthquake. (Source: Hatori et al. (1981))

compared with a pre-computed tsunami waveform in the database at virtual comparison points to select the best-case scenario. In this case, time shift method is selected from $-10$ to 10 min with a 1 min interval.

The comparison between the real-time tsunami waveform and the precomputed waveform in the database is shown in Fig. 2.7a. The lowest RMSE from the time shift method is 0.469 at a time shift of eight minutes, and it is shown as the initial gap of the simulated waveform in the figure. Then, the search engine selects the corresponding scenario as the best-case scenario from database. The searching algorithm requires less than one second to find the best-case scenario in the database for one site, whereas real-time tsunami waveform simulation requires a time of about one minute. To give enough waveform information of a near-field tsunami, 60-minute data are used. The first negative phase of the precomputed

waveform may be caused by a simple rectangular fault model assumption in developing the database, and the virtual comparison point is located close to the negative initial water surface in the tsunami source model. The maximum precomputed tsunami wave height is very close to the maximum tsunami wave height from the real-time waveform simulation. From the best-fit scenario in the database, the tsunami wave will reach the coast of Owase in less than 20 minutes, whereas the required time to obtain fixed earthquake information is 20 minutes based on the 2011 Tohoku earthquake event. Even the database can provide good estimation of tsunami inundation, but a quick tsunami source model is required in minutes in order to calculate the real-time tsunami waveform as soon as possible. In the future, quick and reliable earthquake information such as by utilizing W-phase solutions (e.g., Gusman and Tanioka (2013)) is promising to reduce the required time to obtain a tsunami source model. The maximum tsunami inundation depth from a selected scenario in the database is 2.74 m (Fig. 2.7b), which is very similar to that from the field survey. The forecasted tsunami inundation coverage and depth are also similar to the tsunami inundation result calculated from forward modeling (Fig. 2.7c). The maximum tsunami inundation depth from forward modeling is 2.62 m, slightly underestimating the maximum inundation depth from the field survey by 0.2 m. This may also indicate the good validity of the forward modeling results to the actual tsunami inundation. Overall, the tsunami inundation forecast is good enough to reproduce actual tsunami inundation induced by the 1944 Tonankai earthquake.

### 2.3.2 Predicted future Tokai–Tonankai earthquake

Recently, the Nankai Trough has been considered to be the best location to study the mechanism of a great interplate earthquake with well-documented historical records. In the near future, it is expected that a Mw 8.0-class earthquake would occur (Yokota et al., 2015). The predicted future Tokai–Tonankai earthquake scenario is assumed to be a tremendous earthquake that would severely damage Mie and Aichi Prefectures. Slip distribution of the Tokai–Tonankai earthquake consists of 553 subfaults of different size. The earthquake magnitude is equal to Mw 8.5 by assuming a rigidity of $5 \times 10^{10}$ Nm. Because there is no information about the earthquake's location in this case, only stage 2 is conducted.

The result of tsunami inundation forecast and waveform comparison is shown in Fig. 2.8. The optimum time shift is obtained at one minute with an RMSE of 0.549 (Fig. 2.8a). Similar to the 1944 Tonankai earthquake case, the initial

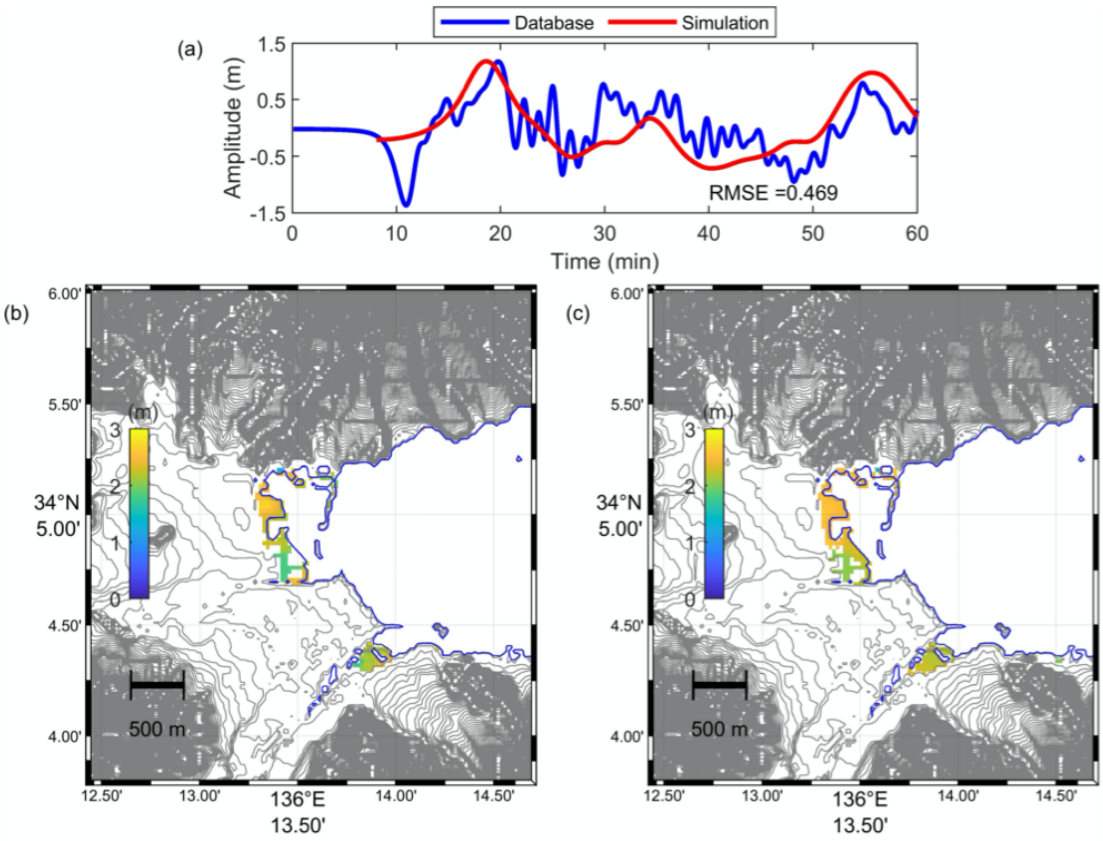


Figure 2.7: The stage 2 results of the 1944 Tonankai earthquake case: (a) comparison between the precomputed tsunami waveform from the selected scenario and the simulated tsunami waveform; (b) a tsunami inundation forecast from the selected scenario. (c) a tsunami inundation from forward modeling.

negative amplitude of a precomputed waveform is caused by the tsunami source model. It indicates that the virtual comparison point is located inside the tsunami source model. A selected precomputed tsunami waveform database can catch the maximum wave height of a simulated waveform very well. The wave phase of a precomputed tsunami waveform is also similar to a simulated waveform, especially for the first wave. Even though the database was built based on a simple rectangular fault model, it still can resemble the characteristics of a tsunami waveform from an earthquake model that is assumed to be a real event. The maximum tsunami inundation depth from the best-case scenario in the database is 4.90 m (Fig 2.8b). This result underestimates the maximum tsunami inundation depth (5.51 m) calculated from forward modeling using the same earthquake model (Fig. 2.8c). However, inundation coverage is almost identical. From the selected scenario, a tsunami wave will reach the Owase coastal area in less than 15 minutes. During this short time, a reliable tsunami source model is required immediately in order to announce warning and evacuation processes

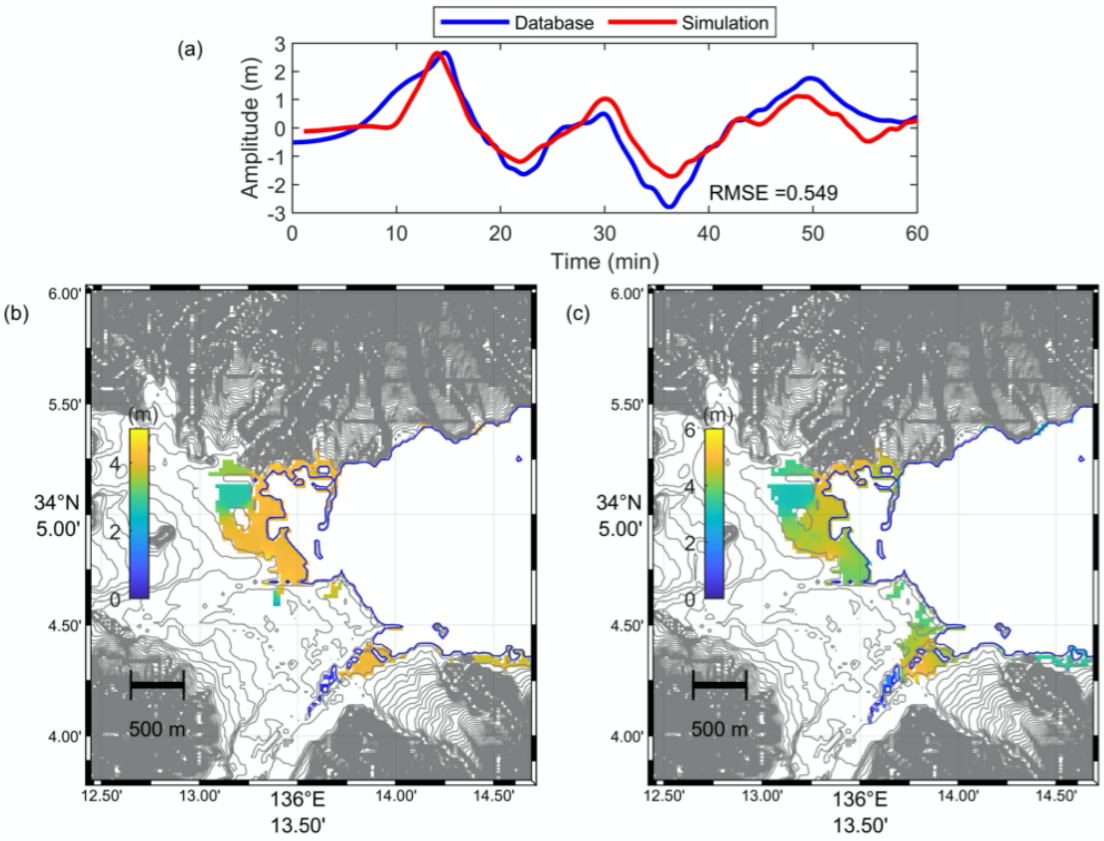


Figure 2.8: The stage 2 results of the Tokai–Tonankai earthquake case. (a) comparison between the precomputed tsunami waveform from the selected scenario and simulated tsunami waveform; (b) a tsunami inundation forecast from the selected scenario; (c) a tsunami inundation from forward modeling.

to the community. At present, tsunami waveform inversion is the best method to produce the most accurate tsunami source model. Unfortunately, with this limited time, it may not be enough to yield an accurate tsunami source, especially with limited tsunami observational systems in this zone. Therefore, as mentioned before, we still consider the use of a simple rectangular fault model to create a tsunami source model, as earthquake information will become available faster than will the tsunami waveform. Accordingly, we are conducting a further study to solve this problem, and the result will be presented in the near future.

### 2.3.3 Predicted future Nankai Megathrust earthquake

The predicted future Nankai Megathrust earthquake is assumed to be the worst case of a Nankai Trough earthquake, where the Tokai, Tonankai, and Nankai segments are ruptured together and generate huge earthquakes followed by tsunamis.

The slip distribution is divided into 1,188 subfaults with various fault sizes, and it can generate an earthquake of magnitude Mw 8.9 by assuming a rigidity of $5 \times 10^{10}$ Nm. Similar to the Tokai–Tonankai earthquake case, only stage 2 is conducted.

The lowest RMSE of 0.728 is obtained, and the best-fit scenario in the database is selected (Fig 2.9a). The maximum wave height of the simulated tsunami waveform is the slightly overestimated maximum wave height from the selected scenario in the database and has a peak time gap of the maximum wave. The inundation coverage and maximum inundation depth of the selected scenario are underestimated compared with those calculated from forward modeling, where the maximum inundation depth is 5.80 m (Figs. 2.9b and 2.9c). Both simulated tsunami waveforms of the predicted future Nankai Megathrust and Tokai–Tonankai earthquakes select the same scenario for the tsunami inundation forecast. This may explain that more variation of earthquake and fault model scenarios in developing a tsunami inundation and waveform database is required to improve the capability of the database.

In all cases, it takes less than 20 min for a tsunami wave to reach the Owase coastal area because of the short distance between the earthquake rupture area and the coast (less than 150 km). Conducting real-time forward modeling with a 2 h simulation time will take about 30 min by using regular computer (equipped with an Intel i-7 4.2 GHz CPU) run on multiple threads (parallel). Therefore, real-time forward modeling is not feasible for the Nankai Trough earthquake except when a high-performance computer, such as the K-supercomputer, is used. Furthermore, this database can be used as an alternative tool to forecast tsunami inundation generated by the Nankai Trough earthquake.

Additionally, from the results of tsunami inundation from forward modeling between the Tokai–Tonankai earthquake (Fig. 2.8c) and the Nankai Megathrust earthquake (Fig. 2.9c), it can be said that inundation coverage and maximum inundation depth are not significantly different by considering quite different earthquake magnitudes and rupture areas. It can be concluded that tsunamis generated by the Nankai segment are less of a threat to Mie and Aichi coastal area. Tsunamis from the Nankai segment may lose energy during propagation and not reach the coast of Mie and Aichi because of the relatively far distance and refraction process.

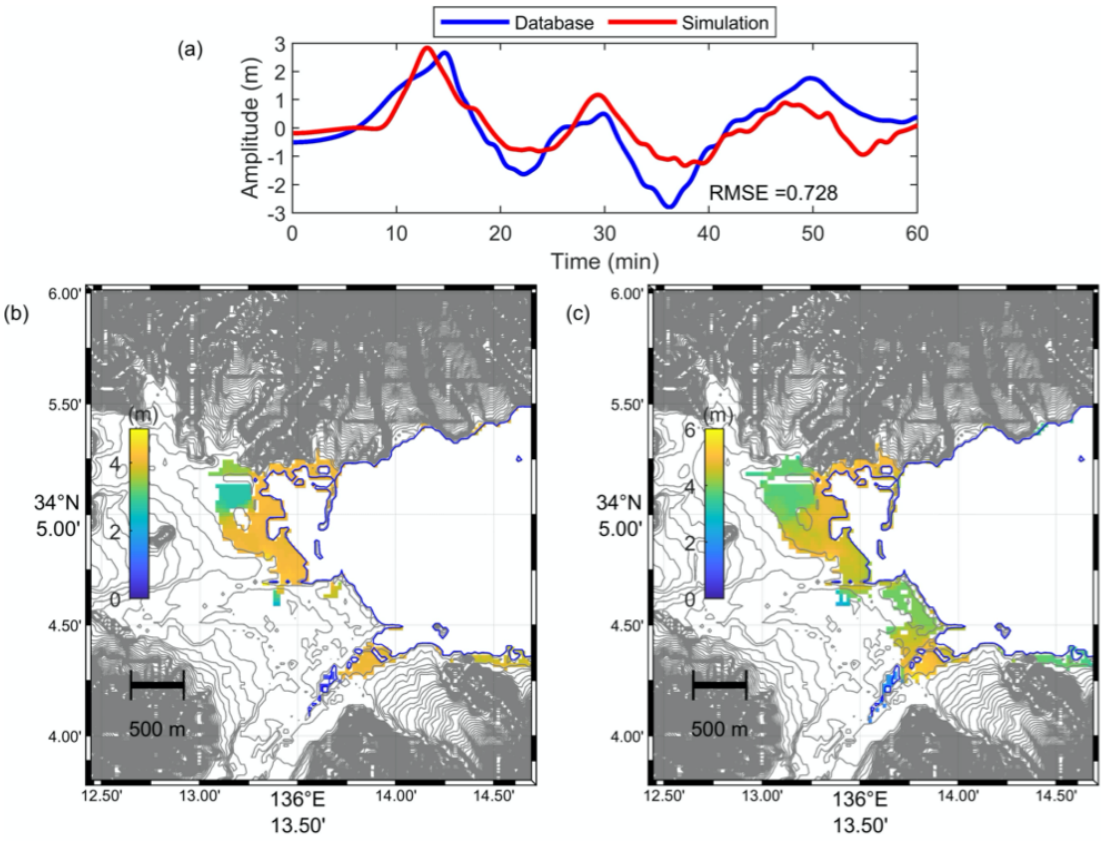


Figure 2.9: The stage 2 results of the Nankai Megathrust earthquake case. (a) comparison between the precomputed tsunami waveform from the selected scenario and the simulated tsunami waveform; (b) a tsunami inundation forecast from the selected scenario; (c) a tsunami inundation from forward modeling.

## 2.4 Summary

The first attempt of this study discussed the possibility of utilizing tsunami inundation and tsunami waveforms in a precomputed database for tsunami inundation forecasting in the Mie and Aichi prefectures of Japan, with the study case in Owase. A database that consists of tsunami inundation and waveforms from 17 hypothetical earthquake models with multiple fault configurations and parameters has been developed in this study.

By using one previous earthquake model and two predicted future earthquake models, we tested the performance of the database. The 1944 Tonankai earthquake was selected to represent previous earthquake cases, and the Tokai–Tonankai and Nankai Megathrust earthquakes represented predicted future earthquake cases. The stage 1 results of the 1944 Tonankai earthquake case explain that only utilizing earthquake coordinates and magnitudes is not enough to produce

a reliable tsunami inundation forecast, even though it can be done shortly after preliminary earthquake information becomes available. The comparisons between the tsunami inundation forecast and tsunami inundation calculated from forward modeling show that the database can fairly well resemble tsunami inundation from numerical forward modeling. This result shows that tsunami inundation forecasting based on the database is suitable for application in the coastal area of the Mie and Aichi prefectures.

However, to conduct real-time tsunami waveform simulation, fixed earthquake information or reliable tsunami source is needed. Based on the 2011 Tohoku earthquake, fixed earthquake information can be obtained at 20 min after the earthquake. This required time is too long because tsunami waves would reach the coast of Owase within less than 20 min. In the future, a quick and reliable method of tsunami source estimation is needed to cut the required time to obtain the tsunami source model.

# References

Abe, I. and Imamura, F. (2012). Verification of the Real-time Forecasting system for Tsunami Inundation using the GPS Buoy in the Case of the 2011 Tohoku Earthquake. *Journal of Japan Society of Civil Engineers, Ser. B2*, 68:I_376–I_380.

Baba, T. and Cummins, P. R. (2005). Contiguous rupture areas of two Nankai Trough earthquakes revealed by high-resolution tsunami waveform inversion. *Geophysical Research Letters*, 32(8):1–4.

Blaser, L., Krüger, F., Ohrnberger, M., and Scherbaum, F. (2010). Scaling relations of earthquake source parameter estimates with special focus on subduction environment. *Bulletin of the Seismological Society of America*, 100(6):2914–2926.

Craig, T. J., Copley, A., and Jackson, J. (2014). A reassessment of outer-rise seismicity and its implications for the mechanics of oceanic lithosphere. *Geophysical Journal International*, 197(1):63–89.

Goda, K. and Abilova, K. (2016). Tsunami hazard warning and risk prediction based on inaccurate earthquake source parameters. *Natural Hazards and Earth System Sciences*, 16(2):577–593.

Gusman, A. R., Murotani, S., Satake, K., Heidarzadeh, M., Gunawan, E., Watada, S., and Schurr, B. (2015). Fault slip distribution of the 2014 Iquique, Chile, earthquake estimated from ocean-wide tsunami waveforms and GPS data. *Geophysical Research Letters*, 42(4):1053–1060.

Gusman, A. R. and Tanioka, Y. (2013). W Phase Inversion and Tsunami Inundation Modeling for Tsunami Early Warning: Case Study for the 2011 Tohoku Event. *Pure and Applied Geophysics*, 171(7):1409–1422.

Gusman, A. R., Tanioka, Y., Macinnes, B. T., and Tsushima, H. (2014). A methodology for near-field tsunami inundation forecasting: Application to the 2011 Tohoku tsunami. *Journal of Geophysical Research: Solid Earth*, 119(11):8186–8206.

Gusman, A. R., Tanioka, Y., Matsumoto, H., and Iwasaki, S. I. (2009). Analysis of the Tsunami generated by the great 1977 Sumba earthquake that occurred in Indonesia. *Bulletin of the Seismological Society of America*, 99(4):2169–2179.

Gusman, A. R., Tanioka, Y., Sakai, S., and Tsushima, H. (2012). Source model of the great 2011 Tohoku earthquake estimated from tsunami waveforms and crustal deformation data. *Earth and Planetary Science Letters*, 341-344:234–242.

Hanks, T. C. and Bakun, W. H. (2002). A bilinear source-scaling model for M-log a observations of continental earthquakes. *Bulletin of the Seismological Society of America*, 92(5):1841–1846.

Hatori, T., Aida, I., Iwasaki, S., and Hibiya, T. (1981). Field Survey of the Tsunamis Inundating Owase City-The 1944 Tonankai, 1960 Chile, and 1854 Ansei Tsunamis. *Bulletin of the Earthquake Research Institute*, 56:245–263.

Hayes, G. P., Wald, D. J., and Johnson, R. L. (2012). Slab1.0: A three-dimensional model of global subduction zone geometries. *Journal of Geophysical Research: Solid Earth*, 117:B01302.

Imamura, F. (2009). Tsunami modeling: Calculating inundation and hazard maps. In *The Sea*, pages 25–42. World Scientific.

Imamura, F., Yalçiner, A. C., and Ozyurt, G. (2006). Tsunami modelling manual. *Tsunami Modelling Manual*.

Kazama, M. and Noda, T. (2012). Damage statistics (Summary of the 2011 off the Pacific Coast of Tohoku Earthquake damage). *Soils and Foundations*, 52(5):780–792.

Mofjeld, H. O., Titov, V. V., González, F. I., and Newman, J. C. (2001). Tsunami scattering provinces in the Pacific Ocean. *Geophysical Research Letters*.

Murotani, S., Miyake, H., and Koketsu, K. (2008). Scaling of characterized slip models for plate-boundary earthquakes. *Earth, Planets and Space*, 60(9):987–991.

Murotani, S., Satake, K., and Fujii, Y. (2013). Scaling relations of seismic moment, rupture area, average slip, and asperity size for M-9 subduction-zone earthquakes. *Geophysical Research Letters*, 40(19):5070–5074.

Ohta, Y., Kobayashi, T., Tsushima, H., Miura, S., Hino, R., Takasu, T., Fujimoto, H., Iinuma, T., Tachibana, K., Demachi, T., Sato, T., Ohzono, M., and Umino, N. (2012). Quasi real-time fault model estimation for near-field tsunami forecasting based on RTK-GPS analysis: Application to the 2011 Tohoku-Oki earthquake (Mw9.0). *Journal of Geophysical Research: Solid Earth*, 117:B02311.

Oishi, Y., Imamura, F., and Sugawara, D. (2015). Near-field tsunami inundation forecast using the parallel TUNAMI-N2 model: Application to the 2011 Tohoku-Oki earthquake combined with source inversions. *Geophysical Research Letters*, 42(4):1083–1091.

Okada, Y. (1985). Surface deformation due to shear and tensile faults in a half-space. *Bulletin of the Seismological Society of America*, 75(4):1135–1154.

Ozaki, T. (2011). Outline of the 2011 off the Pacific coast of Tohoku Earthquake (Mw 9.0). *Earth, Planets and Space*, 63:827–830.

Satake, K., Fujii, Y., Harada, T., and Namegaya, Y. (2013). Time and space distribution of coseismic slip of the 2011 Tohoku earthquake as inferred from Tsunami waveform data. *Bulletin of the Seismological Society of America*, 103(2B):1473–1492.

Tang, L. J., Titov, V. V., Wei, Y., Mofjeld, H. O., Spillane, M., Arcas, D., Bernard, E. N., Chamberlin, C., Gica, E., and Newman, J. (2008). Tsunami forecast analysis for the May 2006 Tonga tsunami. *Journal of Geophysical Research: Oceans*, 113:C12015.

Tanioka, Y. and Satake, K. (1996). Tsunami generation by horizontal displacement of ocean bottom. *Geophysical Research Letters*, 23(8):861–864.

Titov, V., Kânoğlu, U., and Synolakis, C. (2016). Development of MOST for real-time tsunami forecasting. *Journal of Waterway, Port, Coastal and Ocean Engineering*.

Tomita, T. and Takagawa, T. (2014). Development of real-time tsunami hazard mapping system using offshore tsunami measured data. *Journal of Japan Society of Civil Engineers. Ser. B3*, 70(2):I_55–I_60.

Van Veen, B. A., Vatvani, D., and Zijl, F. (2014). Tsunami flood modelling for Aceh & west Sumatra and its application for an early warning system. *Continental Shelf Research*, 79:46–53.

Wells, D. L. and Coppersmith, K. J. (1994). Empirical relationships among magnitude, rupture length, rupture width, rupture area and surface displacements. *Bulletin of the Seismological Society of America*, 84(4):974–1002.

Yokota, Y., Ishikawa, T., Sato, M., ichi Watanabe, S., Saito, H., Ujihara, N., Matsumoto, Y., ichi Toyama, S., Fujita, M., Yabuki, T., Mochizuki, M., and Asada, A. (2015). Heterogeneous interplate coupling along the Nankai Trough, Japan, detected by GPS-acoustic seafloor geodetic observation. *Progress in Earth and Planetary Science*, 2:10.

# Chapter 3

# Tsunami inundation forecasting by using machine learning

## 3.1 Problem description

Generally, the objective of tsunami forecasting is mainly to predict the tsunami waveform and tsunami inundation. Both are vital information during a tsunami event: tsunami waveform prediction is essential for early warning, while the inundation prediction is crucial for the evacuation process. This Chapter is an improvement of the warning system in Chapter 2, in which we focus on the tsunami inundation prediction. Most of the challenges in predicting tsunami inundation in real time is dealing with the computational load. Running a non-linear tsunami model is the most accurate method to predict tsunami inundation. However, with a very short effective period for announcing tsunami information, particularly in the Nankai Trough region, it is not suitable to run a forward model that requires a simulation time of tens of minutes or even hours on a regular computer. Oishi et al. (2015) used a supercomputer to simulate tsunami inundation in real time and was able to generate tsunami inundation for Sendai City with only 1.5 min of computational time. Similarly, Musa et al. (2018) equipped a supercomputer simulation with a delivery/mapping server to send the expected inundation map to the local government. Even so, the use of supercomputers, which are usually owned by the government, has limitations and difficulties, especially for countries or institutions that do not have such facilities. A real-time tsunami inundation forecasting system based on a database for far-field tsunamis has been developed by the National Oceanic and Administration (Tang et al., 2008, Titov

et al., 2005). However, it may not be suitable for near-field tsunami events because it requires direct forward simulation in the system. A more comprehensive tsunami inundation forecasting system for near-field tsunamis has been developed by Gusman et al. (2014). This system finds the best tsunami inundation scenario in the database by matching precomputed and real-time computed tsunami waveforms at virtual observation stations in the coastal region. Recently, there have been further improvements in the use of offshore bottom pressure data for rapid coastal tsunami estimation (Igarashi et al., 2016, Maeda et al., 2015, Tanioka, 2018, Tsushima et al., 2014, Yamamoto et al., 2016). Although such methods are useful for early tsunami warnings, additional procedures are still required to estimate tsunami inundation, as most of these methods are based on a linear long-wave model.

Here we improve the searching algorithm proposed by Gusman et al. (2014), which uses the tsunami waveform at virtual observation points as the input to find the best-fit scenario in the database. To speed up the matching algorithm, we use a convolutional neural network (CNN). Similar to the study conducted by Mulia et al. (2018), we use maximum tsunami amplitude in the low-resolution grid as the model input instead of tsunami waveforms at virtual observation points. Because the tsunami inundation database is usually numerically computed from many simple earthquake scenarios, we believe that simply selecting tsunami inundation from the best scenario in the database is not sufficient to represent the uniqueness and the complexity of an actual earthquake source. Therefore, we also use another machine learning framework, a multilayer perceptron (MLP), to forecast tsunami inundation directly based on the pattern of maximum tsunami amplitude in the low-resolution database.

## 3.2 Database development

### 3.2.1 Study site

In this experiment, we use the Nankai megathrust earthquake to test the performance of our proposed method. We choose two locations for study sites: Atashika and Owase bays (Fig. 3.1a). Atashika Bay directly faces the Pacific Ocean and is approximately 1 to 3 km wide, while Owase bay is a U-shaped bay approximately 7 km wide and 10 km long. Both areas are tsunami-prone areas that have experienced many destructive tsunamis in the past, such as the 1707 Hoei tsunami

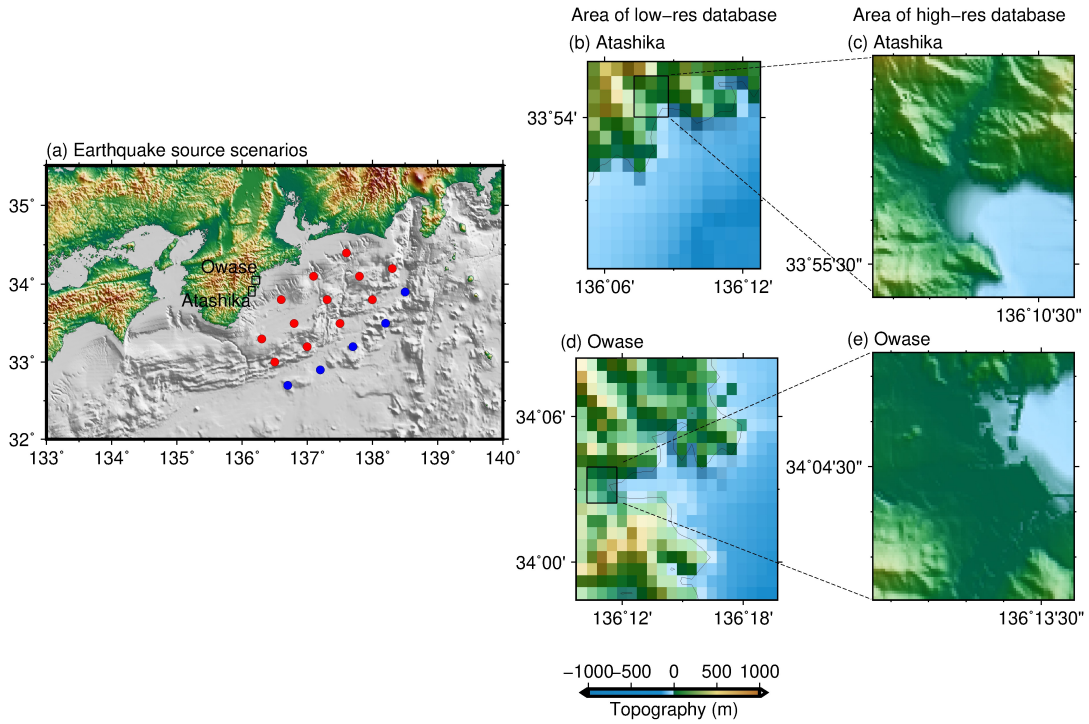


Figure 3.1: (a) Epicenter of fault scenarios used to develop the database. Red circles indicate the coordinate of the top center of the fault for thrust fault and tsunami earthquake scenarios. Blue circles indicate the coordinate of the top center of the fault for reverse fault scenarios. (b) Domain of low- resolution database at Atashika Bay. (c) Domain of high-resolution database at Atashika. (d) Domain of low-resolution database at Owase Bay. (e) Domain of high-resolution database at Owase

(Furumura et al., 2011), the 1944 Tonankai tsunami (Kikuchi et al., 2003), and the 1960 Chilean tsunami (Hatori et al., 1981). Because the location of both areas is close to the earthquake source in Nankai Trough, a tsunami generated in Nankai can reach those areas within a very short time (less than 20 min), as explained in Chapter 2. The unique U-shape of Owase Bay may also generate tsunami amplification as a result of soliton fission due to resonance in the bay (Yamanaka et al., 2016).

### 3.2.2 Fault model scenarios

In this chapter, the same fault model scenarios, as in Chapter 2, are used. Those scenarios are assumed as three types of simple rectangular faults: thrust (reverse fault with low dip angle), tsunami earthquake, and reverse. Earthquake magnitudes for the thrust fault ranging from 8.0 to 9.0 (0.2 interval), and 7.0 to

8.4 (0.2 interval) for the tsunami earthquake and reverse fault is used; in total, there are 328 fault scenarios. The strike angle ($\theta$) is set to 225° as an average orientation of the Nankai Trough subduction zone, while the rake angle ($\lambda$) is set to 90°. The dip angle ($\delta$) for the thrust fault scenarios is determined according to SLAB 1.0 (Hayes et al., 2012), while for the tsunami earthquake and reverse fault scenarios, it is set to 10° and 45°, respectively. The depths of the fault for the thrust and tsunami earthquake scenarios are also determined from SLAB 1.0. For the reverse fault scenarios, the fault depth ranges from 5 to 20 km (5-km interval) according to the outer-rise seismicity depth in Nankai studied by Craig et al. (2014). A magnitude scaling relation for the plate-boundary earthquake proposed by Murotani et al. (2013) (Eq. 2.1) is used to calculate the area of the fault. To compute the initial sea surface for tsunami simulation, we use a coseismic deformation in an elastic half-space model (Okada, 1985) to calculate seafloor deformation, and only the vertical component is used. The computed seafloor deformation is assumed to be the initial sea surface.

### 3.2.3 Precomputed tsunami database

A well-verified tsunami numerical model, JAGURS (Baba et al., 2016, 2015), is used to simulate 2-h tsunami propagation and inundation from the fault scenarios. The simulation is conducted in the spherical coordinate system. Based on Satake (1995), the equation of motion for non-linear shallow water theory is expressed as follows:

$$\frac{\partial u}{\partial t} + \frac{\partial u}{Rsin\theta}\frac{\partial u}{\partial \varphi} + \frac{\nu}{R}\frac{\partial u}{\partial \theta} = -\frac{g}{Rsin\theta}\frac{\partial h}{\partial \varphi} - C_f\frac{u\sqrt{u^2+\nu^2}}{d+h} \tag{3.1}$$

$$\frac{\partial \nu}{\partial t} + \frac{\partial u}{Rsin\theta}\frac{\partial \nu}{\partial \varphi} + \frac{\nu}{R}\frac{\partial u}{\partial \theta} = -\frac{g}{R}\frac{\partial h}{\partial \theta} - C_f\frac{\nu\sqrt{u^2+\nu^2}}{d+h} \tag{3.2}$$

and the continuity equation is,

$$\frac{\partial h}{\partial t} = -\frac{1}{Rsin\theta}\left[\frac{\partial\{u(d+h)\}}{\partial \varphi} + \frac{\partial\{\nu sin\theta(d+h)\}}{\partial \theta}\right] \tag{3.3}$$

where $h$ is the wave height above mean sea water level, $d$ is water depth, $t$ is time, $\varphi$ and $\theta$ are longitude and latitude coordinate, respectively, $u$ and $\nu$ are velocity flux along longitude and latitude axes, $R$ is radius of the Earth, $g$ is the gravitational acceleration, and $C_f$ is the non-dimensional frictional coefficient. Slightly different with the shallow water equation used in Chapter 2, the latitude coordinate $\theta$ in this equation is measured southward from the North Pole. A moving wet and dry boundary condition is used to compute tsunami run-up

and inundation. To solve Eq. (3.1), (3.2), (3.3), staggered grid leap-frog finite difference method is used. The computational domain consists of four nested grids with resolutions of 30, 10, 3.33, and 1.11 arcsec. We use a linear long-wave model for the low- and intermediate-resolution grids (30, 10, and 3.33 arcsec) and a non-linear long-wave model for the high-resolution grid (1.11 arcsec). The topography and bathymetry datasets are obtained from the Cabinet Office of Japan. We set the simulation time step of $\Delta t$=0.25 sec to satisfy the computational stability and a rise time of 60 sec.

To develop the tsunami database, maximum tsunami amplitude in the low-resolution grid (30 arcsec) and tsunami inundation in the high-resolution grid (1.11 arcsec) are stored to create low-resolution and high-resolution databases, respectively. Because the limit of inundation for each earthquake scenario is different in the high-resolution database, the grid points that satisfy inundation coverage for all scenarios are fixed. We consider only the wet grid for the low-resolution database and dry grid for the high-resolution database. The coverages of the low-resolution and high-resolution domains are defined in the area of interest (Fig. 3.1b - e).

## 3.3 Machine learning

In this study, we use two types of machine learning algorithms for two different tasks: CNN for classification and MLP for regression. Similar to the other data-driven models, both CNN and MLP require training process to acquire knowledge from the database, which consists of maximum tsunami amplitude at low-resolution grid and tsunami inundation at high-resolution grid. In the training process, the output variables of CNN are dicrete values representing the scenarios index, while continuous values for MLP. Here, the CNN is proposed as an alternative to the matching algorithm suggested by Gusman et al. (2014) and Mulia et al. (2018), while the MLP is proposed to directly reproduce tsunami inundation in the high-resolution grid. In the other words, to generate tsunami inundation prediction, CNN still relies on the database, in which its network will select the best-fit scenario from the database, while MLP is independent from the database. The flowchart of the application of CNN and MLP to forecast tsunami inundation is shown in Fig. 3.2. The flow of the system is similar to Stage 2 in Chapter 2. The difference is that the input for tsunami inundation forecast in the Stage 2 is the computed tsunami waveform, while in this chapter is the maximum

tsunami amplitude at low-resolution grid. The detailed explanation and network configuration of the CNN and MLP as well database for training and testing are explained in the following subsection. Both proposed frameworks are implemented using an open-source and popular machine learning library, Tensorflow (Abadi et al., 2016).

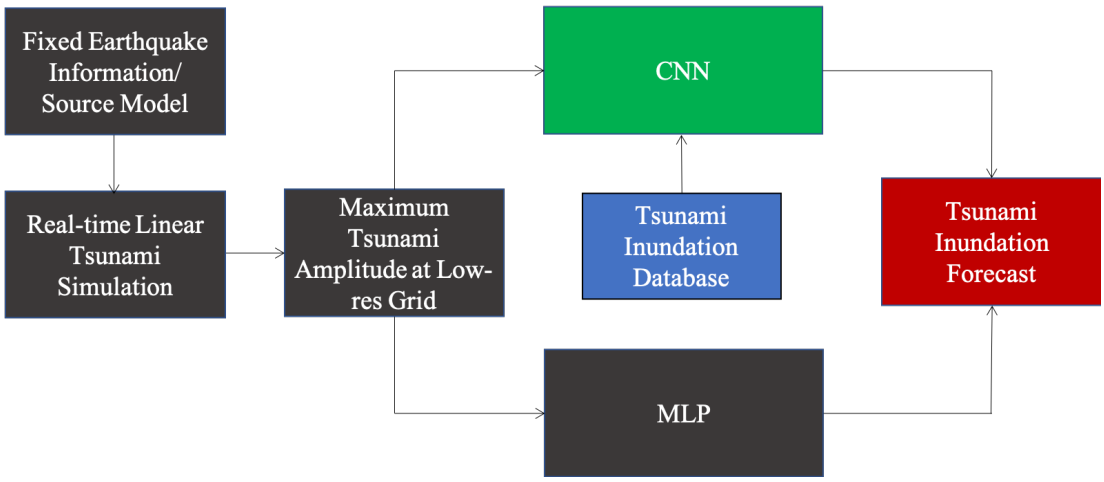


Figure 3.2: Flowchart of the application of CNN and MLP for tsunami inundation forecasting

### 3.3.1 CNN model

The CNN is a machine learning algorithm that is usually used for image or pattern recognition problems (Ciregan et al., 2012, Garcia and Delakis, 2004, Krizhevsky et al., 2012, Sermanet et al., 2013, Tompson et al., 2015), in which it is considered as the best among the other neural network (NN) methods (Krizhevsky et al., 2012). One of the advantages of a CNN over a regular NN is the capability to capture local patterns. Local patterns, which are obtained by down-sampling the input data into small fragments through the convolutional and pooling operator, improve the accuracy of global pattern recognition if they are examined from a large-scale view. A regular CNN typically consists of three layers: the convolutional layer, the pooling layer, and the fully connected layer.

The architecture of CNN used in this study is shown in 3.3. Within the convolutional layer, the input data are filtered and transferred onto the feature map by applying a set of the convolutional kernel. The output of a convolutional layer can be analytically formulated as

$$f = \sigma\left(Wx + b\right) \tag{3.4}$$

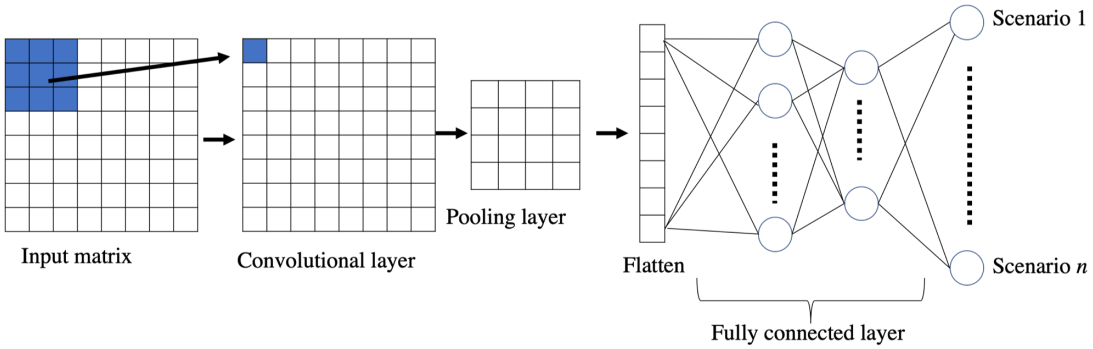


Figure 3.3: CNN architecture

where $W$ are the weights of the kernel with kernel size $m \times n$, $b$ is the bias of the kernel, $x$ is the input kernel, and $r$ is the transfer function. For the transfer function $r$, we select a rectified linear unit (ReLU) transfer function (Nair and Hinton, 2010), $f(x) = max(0, x)$, to introduce the nonlinearity of the network. The pooling layer compresses the size of the feature map and merges the semantically similar features into one feature (Lecun et al., 2015, LeCun et al., 1998). Typically, the pooling unit computes the maximum of a local unit kernel in one feature map. Then, all of the features are sent to the output layer through fully connected layer (conventional NN layer). The distribution over classes is mapped in the output layer by adding a classifier, that is, a softmax activation function.

We carefully investigate the layer configuration, and we finally use only one stage each of the convolutional layer, nonlinearity, and pooling layer, which are followed by two fully connected layers with 128 and 64 nodes. We set the kernel size as $3 \times 3$ and $2 \times 2$ for the convolutional and pooling layers, respectively. As typical deep-learning networks, a CNN may be subjected to overfitting caused by model complexity. It is usually typified by excellent training performance but unreliable testing performance. To avoid this problem, we apply a new kind of regularization term called dropout (Sutskever et al., 2014). The dropout algorithm randomly removes or ignores the hidden nodes and their incoming and outgoing connections with a given dropout probability $p$ ($p = 0.2$ in this study). This technique reduces the complex co-adaptation in the hidden nodes and improves the model performance (Sutskever et al., 2014). To fit the network parameters to the training dataset, which is obtained by minimizing the categorical cross-entropy loss function, we use a back-propagation algorithm with an Adam optimizer (Kingma and Ba, 2015).

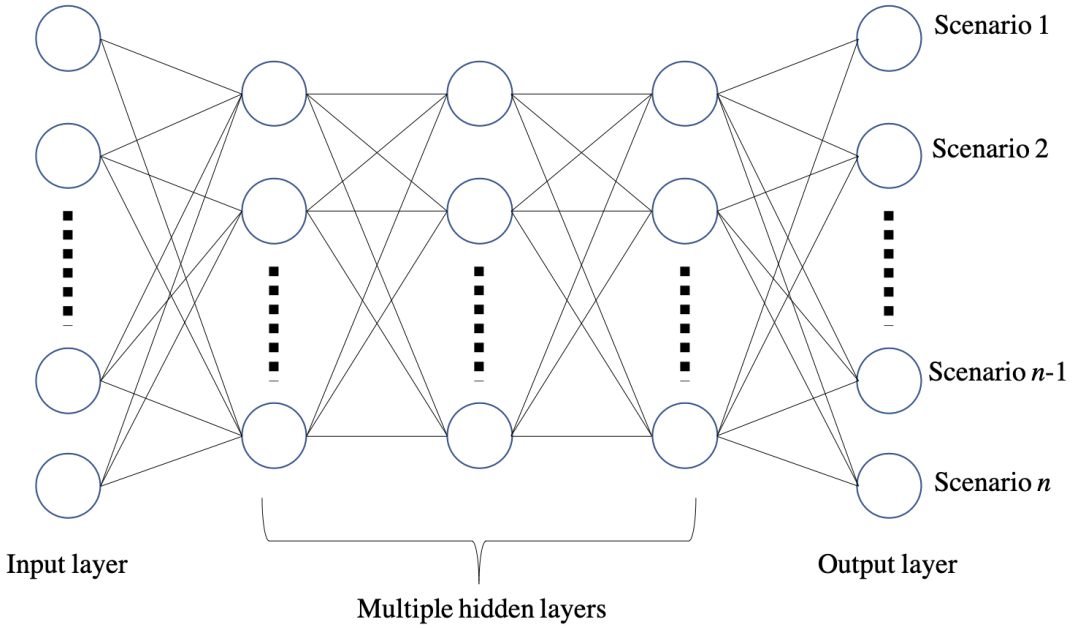


Figure 3.4: MLP architecture

### 3.3.2 MLP model

The MLP is a popular and most-often-used artificial neural network. It is well known for its outstanding performance because of its ability for universal approximation. The mathematical formulation of the MLP is inspired by the structure of the human brain to deal with nonlinear tasks (Haykin, 2008). Therefore, it is an effective method to solve regression problems (e.g.,Bienvenido-Huertas et al. (2019)), such as the problems in this study. The network structure of the MLP consists of three parts: an input layer, one or more hidden layers, and an output layer. MLP architecture is shown in 3.4. The output value of a hidden node $n$ can be expressed as

$$f = \sigma\left(W^l \sigma(W^{(l-1)} \dots (W^0 x + b^0) + b^{(l-1)}) + b^l\right) \tag{3.5}$$

where $l$ indicates the final layer. For the activation function $r$, we select the ReLU activation function (Nair and Hinton, 2010), similar to the CNN model. We apply a loss function based on mean squared error and minimize it by using the Adam optimizer (Kingma and Ba, 2015). Dropout and $L_2$ norm regularizations with regularization parameter $\gamma$ ($\gamma = 0.001$ in this study) are used to avoid overfitting. We investigate the appropriate number of hidden layers and nodes and find that a relatively deep and wide network architecture is necessary to capture the pattern of nonlinear characteristics of tsunami inundation. An MLP network that consists of five hidden layers with 128 nodes is sufficient to produce a reliable prediction.

### 3.3.3 Training dataset

Two types of databases are used in this study, of low resolution and high resolution, as explained in Sect. 3.2. The input data for training is the same for both the CNN and MLP models, that is, the low- resolution database, with a slightly different array configuration. For the low-resolution model, the array size of each scenario is $15 \times 15$ (Atashika) and $20 \times 20$ (Owase) for the CNN model, while for the MLP model, the array is reshaped into a one-dimensional array with sizes of 225 (Atashika) and 400 (Owase). The training target of the CNN model is an array of integers ranging from 1 to 328 to represent the scenario ranking, while the MLP model uses the high-resolution database as the training target. In the high-resolution model, the total number of grid points for each scenario are 6055 and 5826 for Atashika and Owase, respectively. We then stack the array from 328 scenarios in row vectors to create a low-resolution database with array sizes of $328 \times 15 \times 15$ (Atashika) and $328 \times 20 \times 20$ (Owase) for the CNN model and array sizes of $328 \times 225$ (Atashika) and $328 \times 400$ (Owase) for the MLP model. In a similar manner, the array sizes of the high-resolution database become $328 \times 6055$ (Atashika) and $328 \times 5826$ (Owase).

### 3.3.4 Testing dataset

We apply our proposed method to a hypothetical future scenario of the Nankai megathrust earthquake (M8.7) (Central Disaster Management Council, 2003) where the Tokai, Tonankai, and Nankai segments rupture simultaneously. The initial coseismic deformation of the hypothetical Nankai megathrust is shown in Fig. 3.5a. The hypothetical Nankai megathrust tsunami source is used by the Japanese government to formally estimate the tsunami risk and hazard caused by such a disastrous event. In a real event, once a reliable tsunami source is obtained, we then compute tsunami propagation using a linear tsunami model in the low-resolution grid to obtain the maximum tsunami amplitude. The maximum tsunami amplitude generated by the Nankai megathrust earthquake at the selected area (Fig. 3.5b, c) is then used as input for our proposed methods to generate tsunami inundation forecasts. In addition, the simulated tsunami inundation in the high-resolution grid from a nonlinear tsunami model is considered as a pseudo observation to validate our proposed method.

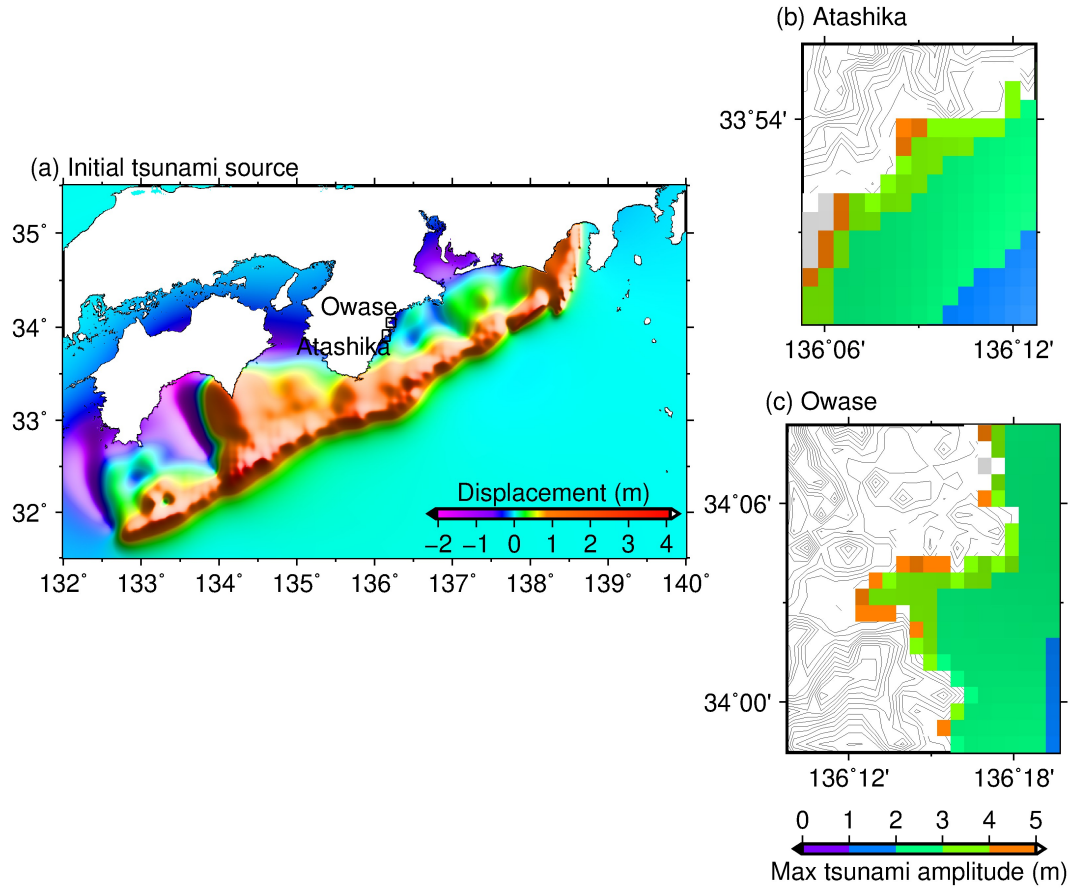


Figure 3.5: (a) Initial tsunami source of the hypothetical Nankai megathrust earthquake. (b) Maximum tsunami amplitude at Atashika as input to the networks. (c) Maximum tsunami amplitude at Owase as input to the networks

## 3.4 Tsunami inundation results

To quantify the prediction accuracy, the forecasted inundation is compared with the inundation from the forward modeling (depth and coverage). Because we use the pseudo observation, and because the tsunami inundation forecasts in our study may have inundation coverages different from that obtained by forward modeling, we select a relative error ($d$) to measure the model performance and avoid the errors caused by the logarithm of zero values

$$d = \frac{1}{N}\sum_{i=1}^{N}\left(2 \times \frac{(Y_i - \hat{Y}_i)}{|Y_i| + |\hat{Y}_i|}\right) \tag{3.6}$$

where $Y_i$ and $\hat{Y}_i$ indicate the tsunami inundation depth from the forward modeling and prediction at point $i$, respectively, and $d$ is a signed expression ranging from -2 to 2 that is positive for underestimation and negative for overestimation of the prediction over the observation. When $d$ is closer to zero, it indicates better

forecast accuracy. In addition, we also use a standard statistical measure, root mean square error (RMSE), which measures the average magnitude of the error.

### 3.4.1 CNN model results

Conventionally, comparing the result of direct linear forward modeling with the precomputed result in the database is the easiest method to find the best-fit scenario. This assumption was used by Gusman et al. (2014) to compare the tsunami waveforms from direct forward modeling with those in the database. However, when utilizing an extensive database (e.g., Baba et al. (2014)), such a method is not practical because it may require a relatively long computational time. Mulia et al. (2018) also used a similar method by comparing maximum tsunami amplitudes in the low-resolution grid with those precomputed in the database. To simplify the searching process, the input and the database should go through a principal component analysis (PCA) to reduce the dimensionality and select the scenario that gives the smallest Euclidian distance relative to the direct forward modeling as the forecast.

Once it is trained, the CNN is able to find the best-fit scenario in near real time (Kolsch et al., 2018, Wang et al., 2019). Furthermore, the convolutional and pooling layers, which give the CNN an outstanding pattern recognition, may reduce the misrecognition caused by the complexity of the data. The comparison between CNN-estimated tsunami inundation and the tsunami inundation from the forward modeling at Atashika and Owase are shown in Figs. 3.6b and 3.6b, respectively, while the statistical measures are shown in Table 3.1. In Atashika, the CNN-estimated tsunami inundation is very similar to the tsunami inundation from the forward modeling having similar coverage, with $d = -0.003$ and RMSE = 1.882 m (Fig. 3.6b). The maximum inundation depth is slightly larger, by 0.53 m, than the maximum inundation depth from the forward modeling. In contrast, the tsunami inundation forecast in Owase shows underestimation of the tsunami inundation from the forward modeling, with $d = 0.548$ and RMSE = 2.117 m (Fig. 3.7b). Moreover, the forecast has a limit of inundation that is significantly lower than that of the forward modeling in the southern part of Owase (area below latitude $34°04'30''$), with a total underestimation of 405 grid points. The forecasted maximum inundation depth in Owase also has a slightly larger error than that at Atashika with a discrepancy of 0.63 m.

In this study, we apply a $k$-fold cross-validation technique in training the network.

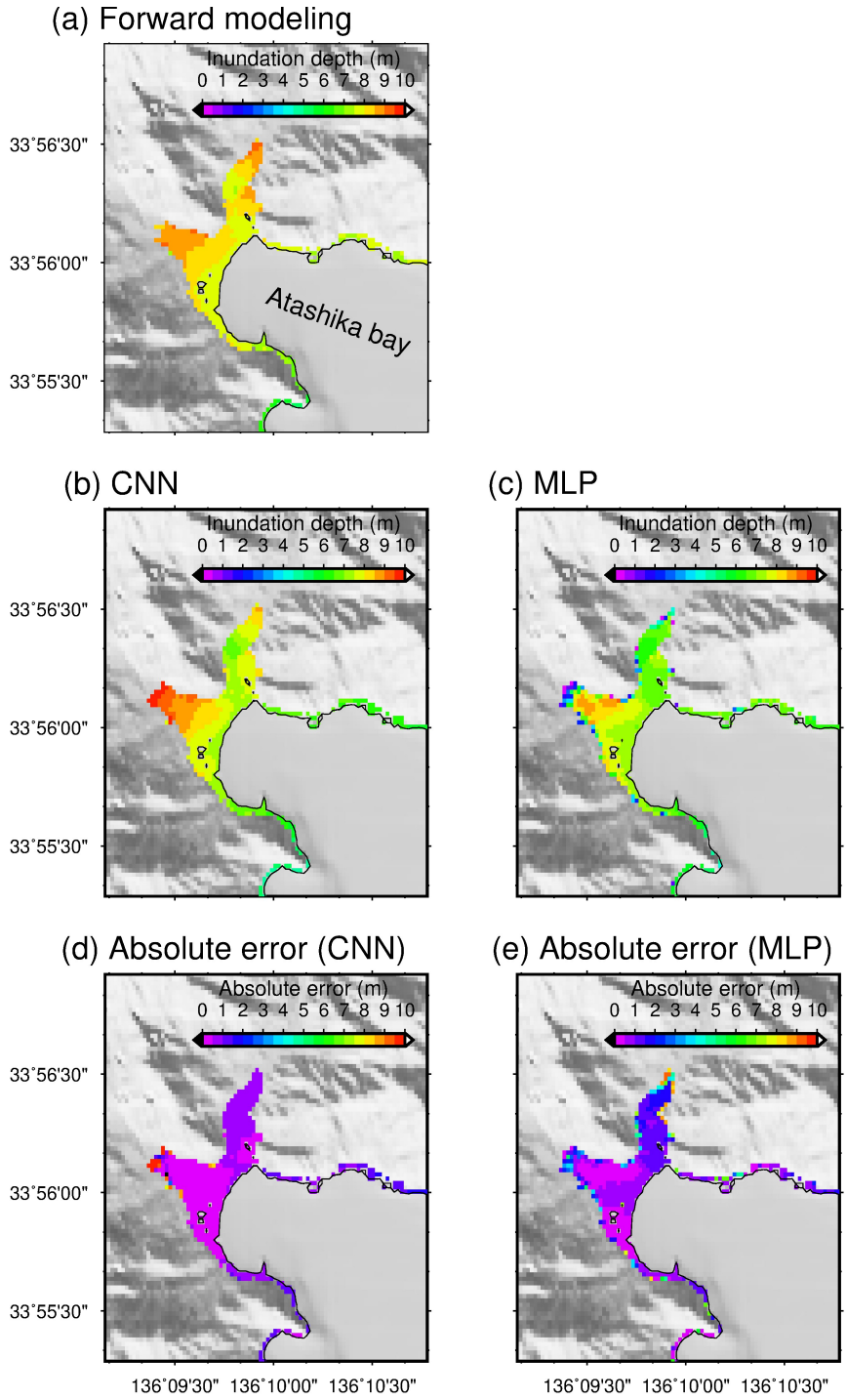


Figure 3.6: (a) Reference tsunami inundation at Atashika obtained from forward modeling. (b), (c) Forecasts obtained from the proposed methods. (d), (e) Absolute error between forecasts and forward modeling

The $k$-fold cross-validation is necessary to reduce the variance of the model and the bias, and thus allow us to estimate the generalization capability of the machine learning (Jiang and Wang, 2017). We randomly divide the dataset into tenfolds, in which each fold consists of nine subsets for training the model, and the remaining

subset for the testing. This folding procedure is repeated 10 times. The average value of the tenfolds is generally accepted to quantify the capability of the model against an independent dataset. Implementing tenfolds of $k$-fold, we find out that our model correctly recognizes the appropriate scenario for a training dataset with accuracy of 98.80% and 98.21% in Atashika and Owase, respectively.

### 3.4.2 MLP model result

Because every submarine earthquake has unique characteristics (i.e., coseismic deformation), the forecasted tsunami inundation from the best-fit scenario selected by the CNN may not closely represent the real tsunami inundation caused by the simple fault assumption used to develop the database. Unlike a CNN purposed for classification tasks, in which the algorithm will select the best-fit scenario from the database, the MLP has the ability to produce a unique output based on the knowledge acquired during the learning process. In other words, the MLP acts like tsunami inundation modeling based on the pattern of the training samples.

The comparison between MLP-estimated tsunami inundation and the forward modeling for Atashika and Owase are shown in Figs. 3.6c and 3.7c, respectively. The MLP-estimated tsunami inundation in Atashika underestimates the forward modeling with $d = 0.007$ and RMSE = 2.190 m, as shown in Table 3.1. The forecast poses inundation coverage similar to that of the forward modeling, even though it has a lower accuracy compared with the CNN, which is indicated by the larger RMSE value. The maximum inundation depth forecasted by the MLP is very similar to the forward modeling, with a discrepancy of 0.25 m. In Owase, the MLP provides a better result compared with the CNN, with $d = \breve{}0.061$ and RMSE = 1.142 m. The MLP-estimated maximum inundation depth is also almost identical to that of the forward modeling. An obvious difference between the tsunami inundation forecasts from the CNN and MLP in Owase is the limit of inundation. The forecast from the MLP successfully provided acceptable inundation coverage, with total overestimation of 104 grid points, whereas the CNN has an underestimation with a greater magnitude. Applying $k$-fold cross-validation with tenfolds produced an RMSE ranging from 0.35 m to 0.60 m and 0.32 m to 0.85 m for the testing dataset at Atashika and Owase, respectively. For the training dataset, the error ranges from 0.28m to 0.75m and 0.35m to 0.50m at Atashika and Owase, respectively.

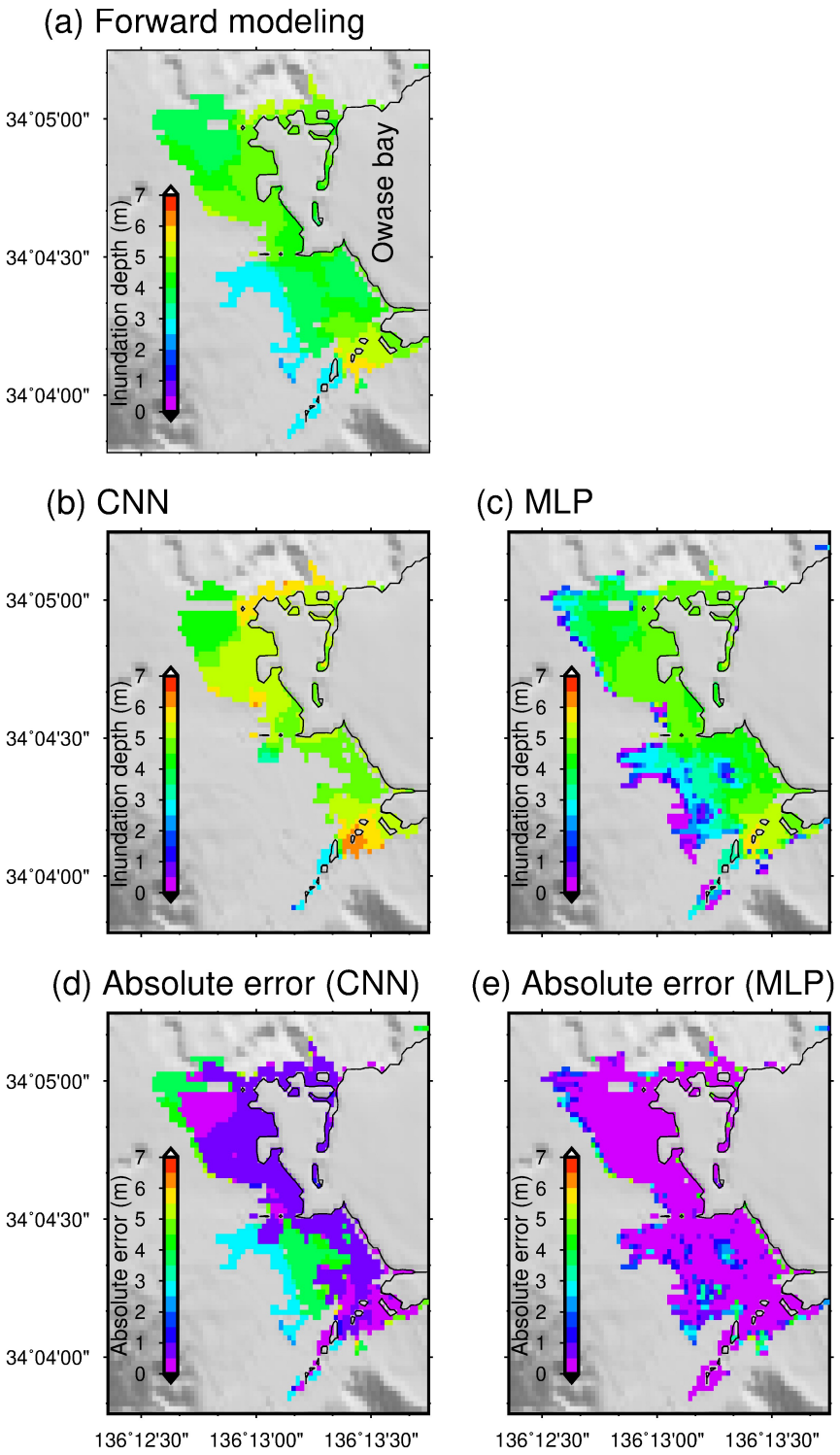


Figure 3.7: (a) Reference tsunami inundation at Owase obtained from forward modeling. (b), (c) Forecasts obtained from the proposed methods. (d), (e) Absolute error between forecasts and forward modeling

Table 3.1: Statistical measures of the results.

| **Method** | **Site** | $d$ | **RMSE** (m) | **Min** (m) | **Max** (m) | **Mean** (m) | **Number of inundated grid points** |
|---|---|---|---|---|---|---|---|
| Forward modeling | Atashika | - | - | 0 | 9.378 | 7.735 | 527 |
| | Owase | - | - | 0 | 5.754 | 3.761 | 1279 |
| CNN | Atashika | -0.003 | 1.882 | 0 | 9.904 | 7.588 | 545(18) |
| | Owase | 0.548 | 2.117 | 0 | 6.378 | 3.410 | 874(-405) |
| MLP | Atashika | 0.073 | 2.190 | 0 | 9.123 | 6.505 | 546(19) |
| | Owase | -0.061 | 1.142 | 0 | 5.768 | 3.656 | 1383(104) |

Values in parentheses in the last column indicate the differences in the number of inundated grid points modeling. Positive values indicate overestimation, and negative values indicate underestimation between forecasts and forward.

## 3.5 Discussion

Like the other tsunami inundation forecasting systems that use an algorithm that matches scenarios against a database (Gusman et al., 2014, Mulia et al., 2018, Setiyono et al., 2017), the performance of the forecast depends on the variability and the number of scenarios used to develop the database. The under-estimation of the CNN-forecasted tsunami inundation over the forward modeling at Owase indicates that the number of scenarios in our database is not sufficient, and thus the pattern of the maximum tsunami amplitude of the new input cannot fit a pattern in the low-resolution database. However, even with the limited scenarios, the MLP can provide a more acceptable result. One of the drawbacks of the MLP, as with the other black-box models, is that the forecasted inundation depth cannot represent the physical meaning of the physics of tsunami inundation.

For further analysis of the performance of the forecasts, the relative error at the grid points is also presented as a box and whiskers diagram (Fig. 3.8). At Atashika, the results from both methods show a similar distribution. For the CNN, the median of the relative error is slightly closer to zero than the MLP result. The forecast from the CNN also possesses better accuracy than that of the MLP, as indicated by the range and length of the box and whiskers, though the differences are not significant. In contrast, the distribution of the relative error

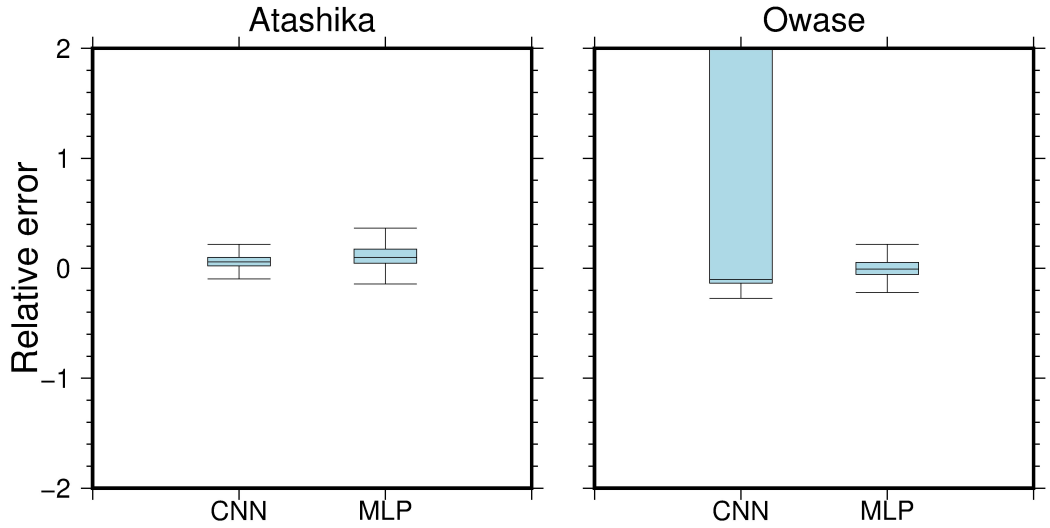


Figure 3.8: Box and whisker plots indicating the relative error between forward modeling and the forecasts at Atashika and Owase

of the forecast at Owase exhibits characteristics different from that at Atashika. Most of the relative errors of the forecast from the CNN are distributed within a range of 0 to 2, which indicates a strong underestimation caused by a significant difference in the limit of inundation between the forecast and forward modeling. In contrast, the MLP presents a more satisfactory result, in which the relative errors are mostly distributed near zero. Additionally, in Figs. 3.6e and 3.7e, it is observed that the overestimation and underestimation of the forecasted inundation depth are mostly located near the edge of the limit of inundation. To suppress this effect, which is probably caused by the model complexity, the MLP requires an additional regularizer ($L_2$ norm regularizer) in addition to the dropout regularizer. This may also explain why the MLP can capture the pattern of the inundation limit more easily than it can capture the inundation depth. A further study is being conducted to address this issue by using a stacked generalization ensemble method, and the results will be presented in the future.

The CNN and MLP models learn the pattern of the maximum tsunami amplitude during the training process. After the network has been trained, the prediction can be made quickly by performing a matrix multiplication procedure. We use a desktop computer equipped with an Intel i7 processor to conduct forward modeling, while a notebook computer with an i5 processor performed the machine learning simulation. Computationally, the nonlinear forward model requires about 40 min (on eight cores) for a 2-h simulation, while CNN and MLP require less than 1 s (0.069 and 0.084 s for CNN and MLP, respectively, on a single

processor) to produce a tsunami inundation forecast. In a real event, although the time required for the prediction process can be ignored, the proposed methods depend heavily on a reliable tsunami source model. Considering that a tsunami caused by a hypothetical future Nankai megathrust earthquake can quickly reach the region used in this study, a robust and fast method to obtain a tsunami source model is needed. Seismic waves, which propagate faster than tsunamis, are promising for use in estimating the tsunami source about 5 to 10 min after the earthquake, as presented by Gusman and Tanioka (2013) and Kanamori (2015). Furthermore, computing the maximum tsunami amplitude using a linear model in the low-resolution grid takes less than 2 min on a regular computer (on eight cores). In total, to generate a tsunami inundation forecast, it only takes approximately 7–12 min. By using our proposed methods, we can provide more lead time, which is very important to give sufficient warning to coastal residents who need to evacuate the inundation area.

The advantages of our proposed methods over the NearTIF method (Gusman et al., 2014) are that our proposed methods can provide better and faster tsunami inundation prediction because the MLP can predict tsunami inundation using the learned scenarios and they have no waveform time-shifting procedure, as in NearTIF which may take some time. The ability of our proposed methods is similar to that of the method proposed by Mulia et al. (2018), which is able to provide a unique tsunami inundation forecast. However, in the method of Mulia et al. (2018), applying the interpolation method produces a tsunami inundation prediction that is exactly half of the Euclidian distance between the two closest samples, whereas the MLP produces inundation prediction based on the patterns learned during the training process. A problem arises when the number of scenarios is limited, so that the tsunami inundation from the two closest samples may be significantly different. Thus, the interpolation method may produce inundation prediction with significant overestimation or underestimation. Therefore, we would expect that the MLP provides a better tsunami inundation result compared with the method of Mulia et al. (2018).

For future development, adding more fault scenarios is essential to improve the prediction capability of the models. This can be accomplished by incorporating unique features from well-verified earthquakes or tsunami source models of previous events in the region, such as the 1707 Hoei (Furumura et al., 2011), the 1944 Tonankai (Baba et al., 2006), and the 1946 Nankai (Murotani et al., 2015) events. To consider the uncertainty of source properties of future tsunamigenic earthquakes, stochastic earthquake sources (Goda et al., 2018) are sug-

gested for inclusion. Incorporating the influence of tides in shallow waters within the tsunami simulation could provide substantial results for tsunami hazard preparedness (Lee et al., 2015), and thus this effect should be considered in a future study. Additionally, although it requires high computational cost, incorporating a dispersive effect in the nonlinear tsunami model successfully reproduces soliton fission along the Sendai coast during the 2011 Tohoku tsunami (Baba et al., 2015). With U-shaped topography, Owase is also subjected to soliton fission effects (Yamanaka et al., 2016); therefore, applying dispersive effects may provide a more comprehensive database.

It is straightforward to apply the proposed methods in this study to other locations. However, because the model parameters (weight and bias) are particularly purposed for Atashika and Owase, it is necessary to re-train the model to fit each new specific location. Of course, the low-resolution and high-resolution domains need to be carefully adjusted to give a reliable result. In the near future, it is expected that these data-driven models will become a standard method for solving various problems, especially early warning tasks.

## 3.6 Summary

To improve the matching algorithm in Chapter 2 and previous studies (Gusman et al., 2014, Mulia et al., 2018), two machine learning models (CNN and MLP) have been developed in this experiment. The concept of the CNN is similar to the method proposed by Mulia et al. (2018), which selects the best-fit scenario in the database based on similarity pattern between computed and precomputed maximum tsunami amplitude in the low-resolution grid. The difference is that the pattern recognition in the previous study is conducted by using principal component analysis, a conventional dimensionality reduction algorithm, while the dimensionality reduction is performed within the convolutional and pooling layers of a CNN in this experiment. Because the database is developed from limited simple fault scenarios, there is a possibility that the CNN is unable to find the appropriate best-fit scenario, as shown for Owase. However, the MLP, which is purposed for the regression task, is able to yield a more acceptable forecast than CNN when there is no scenario in the database that has a pattern similar to that produced by direct forward modeling. With a quick calculation time, both methods are strong candidates for a future tsunami inundation forecasting system.

The proposed methods rely on accurate and reliable tsunami source models to generate inundation forecasts. Due to the short distance between the Nankai Trough and the nearby Japanese coast, a fast and reliable tsunami source model is needed. A tsunami source model based on W-phase inversion Gusman and Tanioka (2013), which only requires about 10 min, is a promising method for integration with the proposed methods. In the future, further development should focus on improving the reliability of the database by incorporating more scenarios. The network architecture may also need to be improved to accommodate more input variables, such as tsunami height at observation stations, to produce a better forecast.

# References

Abadi, M., Barham, P., Chen, J., Chen, Z., Davis, A., Dean, J., Devin, M., Ghemawat, S., Irving, G., Isard, M., Kudlur, M., Levenberg, J., Monga, R., Moore, S., Murray, D. G., Steiner, B., Tucker, P., Vasudevan, V., Warden, P., Wicke, M., Yu, Y., Zheng, X., Brain, G., Osdi, I., Barham, P., Chen, J., Chen, Z., Davis, A., Dean, J., Devin, M., Ghemawat, S., Irving, G., Isard, M., Kudlur, M., Levenberg, J., Monga, R., Moore, S., Murray, D. G., Steiner, B., Tucker, P., Vasudevan, V., Warden, P., Wicke, M., Yu, Y., and Zheng, X. (2016). TensorFlow: A System for Large-Scale Machine Learning. In *12th USENIX conference on Operating Systems Design and Implementation*, pages 265–283.

Baba, T., Ando, K., Matsuoka, D., Hyodo, M., Hori, T., Takahashi, N., Obayashi, R., Imato, Y., Kitamura, D., Uehara, H., Kato, T., and Saka, R. (2016). Large-scale, high-speed tsunami prediction for the Great Nankai Trough Earthquake on the K computer. *International Journal of High Performance Computing Applications*, 30(1):71–84.

Baba, T., Cummins, P. R., Hori, T., and Kaneda, Y. (2006). High precision slip distribution of the 1944 Tonankai earthquake inferred from tsunami waveforms: Possible slip on a splay fault. *Tectonophysics*, 426:119–134.

Baba, T., Takahashi, N., and Kaneda, Y. (2014). Near-field tsunami amplification factors in the Kii Peninsula, Japan for Dense Oceanfloor Network for Earthquakes and Tsunamis (DONET). *Marine Geophysical Research*, 35(3):319–325.

Baba, T., Takahashi, N., Kaneda, Y., Ando, K., Matsuoka, D., and Kato, T. (2015). Parallel Implementation of Dispersive Tsunami Wave Modeling with a

Nesting Algorithm for the 2011 Tohoku Tsunami. *Pure and Applied Geophysics*, 172(12):3455–3472.

Bienvenido-Huertas, D., Rubio-Bellido, C., Pérez-Ordóñez, J. L., and Moyano, J. (2019). Optimizing the evaluation of thermal transmittance with the thermometric method using multilayer perceptrons. *Energy and Buildings*, 198:395–411.

Central Disaster Management Council (2003). Risk assessment results of Tokai-Tonankai-Nankai earthquake disaster. Technical report.

Ciregan, D., Meier, U., and Schmidhuber, J. (2012). Multi-column deep neural networks for image classification. In *Proceedings of the IEEE Computer Society Conference on Computer Vision and Pattern Recognition*, pages 333–338.

Craig, T. J., Copley, A., and Jackson, J. (2014). A reassessment of outer-rise seismicity and its implications for the mechanics of oceanic lithosphere. *Geophysical Journal International*, 197(1):63–89.

Furumura, T., Imai, K., and Maeda, T. (2011). A revised tsunami source model for the 1707 Hoei earthquake and simulation of tsunami inundation of Ryujin Lake, Kyushu, Japan. *Journal of Geophysical Research: Solid Earth*, 116(B02308).

Garcia, C. and Delakis, M. (2004). Convolutional face finder: A neural architecture for fast and robust face detection. *IEEE Transactions on Pattern Analysis and Machine Intelligence*, 56:1408–1423.

Goda, K., Yasuda, T., Mai, P. M., Maruyama, T., and Mori, N. (2018). Tsunami simulations of mega-thrust earthquakes in the Nankai–Tonankai Trough (Japan) based on stochastic rupture scenarios. *Geological Society, London, Special Publications*, 456.

Gusman, A. R. and Tanioka, Y. (2013). W Phase Inversion and Tsunami Inundation Modeling for Tsunami Early Warning: Case Study for the 2011 Tohoku Event. *Pure and Applied Geophysics*, 171(7):1409–1422.

Gusman, A. R., Tanioka, Y., Macinnes, B. T., and Tsushima, H. (2014). A methodology for near-field tsunami inundation forecasting: Application to the 2011 Tohoku tsunami. *Journal of Geophysical Research: Solid Earth*, 119(11):8186–8206.

Hatori, T., Aida, I., Iwasaki, S., and Hibiya, T. (1981). Field Survey of the Tsunamis Inundating Owase City-The 1944 Tonankai, 1960 Chile, and 1854 Ansei Tsunamis. *Bulletin of the Earthquake Research Institute*, 56:245–263.

Hayes, G. P., Wald, D. J., and Johnson, R. L. (2012). Slab1.0: A three-dimensional model of global subduction zone geometries. *Journal of Geophysical Research: Solid Earth*, 117:B01302.

Haykin, S. (2008). *Neural Networks and Learning Machines*.

Igarashi, Y., Hori, T., Murata, S., Sato, K., Baba, T., and Okada, M. (2016). Maximum tsunami height prediction using pressure gauge data by a Gaussian process at Owase in the Kii Peninsula, Japan. *Marine Geophysical Research*, 37:361–370.

Jiang, G. and Wang, W. (2017). Error estimation based on variance analysis of k-fold cross-validation. *Pattern Recognition*, 69:94–106.

Kanamori, H. (2015). Earthquake Hazard Mitigation and Real-Time Warnings of Tsunamis and Earthquakes. *Pure and Applied Geophysics*, 172(9):2335–2341.

Kikuchi, M., Nakamura, M., and Yoshikawa, K. (2003). Source rupture processes of the 1944 Tonankai earthquake and the 1945 Mikawa earthquake derived from low-gain seismograms. *Earth, Planets and Space*, 55:159–172.

Kingma, D. P. and Ba, J. L. (2015). Adam: A method for stochastic gradient descent. *ICLR: International Conference on Learning Representations*.

Kolsch, A., Afzal, M. Z., Ebbecke, M., and Liwicki, M. (2018). Real-Time Document Image Classification Using Deep CNN and Extreme Learning Machines. In *Proceedings of the International Conference on Document Analysis and Recognition, ICDAR*.

Krizhevsky, A., Sutskever, I., and Hinton, G. E. (2012). ImageNet Classification with Deep Convolutional Neural Networks. In *ImageNet Classification with Deep Convolutional Neural Networks*, pages 1090–1098.

Lecun, Y., Bengio, Y., and Hinton, G. (2015). Deep learning. *Nature*, 521(7553):436–444.

LeCun, Y., Bottou, L., Bengio, Y., and Haffner, P. (1998). Gradient-based learning applied to document recognition. *Proceedings of the IEEE*, pages 2278–2324.

Lee, H. S., Shimoyama, T., and Popinet, S. (2015). Impacts of tides on tsunami propagation due to potential Nankai Trough earthquakes in the Seto Inland Sea, Japan. *Journal of Geophysical Research: Oceans*, 120(10):6865–6883.

Maeda, T., Obara, K., Shinohara, M., Kanazawa, T., and Uehira, K. (2015). Successive estimation of a tsunami wavefield without earthquake source data: A data assimilation approach toward real-time tsunami forecasting. *Geophysical Research Letters*, 42:7923–7932.

Mulia, I. E., Gusman, A. R., and Satake, K. (2018). Alternative to non-linear model for simulating tsunami inundation in real-time. *Geophysical Journal International*, 214:2002–2013.

Murotani, S., Satake, K., and Fujii, Y. (2013). Scaling relations of seismic moment, rupture area, average slip, and asperity size for M-9 subduction-zone earthquakes. *Geophysical Research Letters*, 40(19):5070–5074.

Murotani, S., Shimazaki, K., and Koketsu, K. (2015). Rupture process of the 1946 Nankai earthquake estimated using seismic waveforms and geodetic data. *Journal of Geophysical Research: Solid Earth*, 120(8):5677–5692.

Musa, A., Watanabe, O., Matsuoka, H., Hokari, H., Inoue, T., Murashima, Y., Ohta, Y., Hino, R., Koshimura, S., and Kobayashi, H. (2018). Real-time tsunami inundation forecast system for tsunami disaster prevention and mitigation. *Journal of Supercomputing*, 74:3093–3113.

Nair, V. and Hinton, G. (2010). Rectified Linear Units Improve Restricted Boltzmann Machines. In *Proceedings of the 27th International Conference on Machine Learning*.

Oishi, Y., Imamura, F., and Sugawara, D. (2015). Near-field tsunami inundation forecast using the parallel TUNAMI-N2 model: Application to the 2011 Tohoku-Oki earthquake combined with source inversions. *Geophysical Research Letters*, 42(4):1083–1091.

Okada, Y. (1985). Surface deformation due to shear and tensile faults in a half-space. *Bulletin of the Seismological Society of America*, 75(4):1135–1154.

Satake, K. (1995). Linear and nonlinear computations of the 1992 Nicaragua earthquake tsunami. *Pure and Applied Geophysics*, 144((3-4)):455–470.

Sermanet, P., Kavukcuoglu, K., Chintala, S., and Lecun, Y. (2013). Pedestrian detection with unsupervised multi-stage feature learning. In *Proceedings of the*

*IEEE Computer Society Conference on Computer Vision and Pattern Recognition.*

Setiyono, U., Gusman, A. R., Satake, K., and Fujii, Y. (2017). Pre-computed tsunami inundation database and forecast simulation in Pelabuhan Ratu, Indonesia. *Pure and Applied Geophysics*, 178(8):3219–3235.

Sutskever, I., Hinton, G., Krizhevsky, A., and Salakhutdinov, R. R. (2014). Dropout : A Simple Way to Prevent Neural Networks from Overfitting. *Journal of Machine Learning Research*, 15(1):1929–1958.

Tang, L. J., Titov, V. V., Wei, Y., Mofjeld, H. O., Spillane, M., Arcas, D., Bernard, E. N., Chamberlin, C., Gica, E., and Newman, J. (2008). Tsunami forecast analysis for the May 2006 Tonga tsunami. *Journal of Geophysical Research: Oceans*, 113:C12015.

Tanioka, Y. (2018). Tsunami Simulation Method Assimilating Ocean Bottom Pressure Data Near a Tsunami Source Region. *Pure and Applied Geophysics*, 175:721–729.

Titov, V. V., González, F. I., Bernard, E. N., Eble, M. C., Mofjeld, H. O., Newman, J. C., and Venturato, A. J. (2005). Real-time tsunami forecasting: Challenges and solutions. In *Developing Tsunami-Resilient Communities: The National Tsunami Hazard Mitigation Program*, pages 41–58.

Tompson, J., Goroshin, R., Jain, A., LeCun, Y., and Bregler, C. (2015). Efficient object localization using Convolutional Networks. In *Proceedings of the IEEE Computer Society Conference on Computer Vision and Pattern Recognition.*

Tsushima, H., Hino, R., Ohta, Y., Iinuma, T., and Miura, S. (2014). TFISH/RAPiD: Rapid improvement of near-field tsunami forecasting based on offshore tsunami data by incorporating onshore GNSS data. *Geophysical Research Letters*, 41:3390–3397.

Wang, X., Zhang, W., Wu, X., Xiao, L., Qian, Y., and Fang, Z. (2019). Real-time vehicle type classification with deep convolutional neural networks. *Journal of Real-Time Image Processing*, 16(1):5–14.

Yamamoto, N., Aoi, S., Hirata, K., Suzuki, W., Kunugi, T., and Nakamura, H. (2016). Multi-index method using offshore ocean-bottom pressure data for real-time tsunami forecast 4. Seismology. *Earth, Planets and Space*, 68.

Yamanaka, Y., Sato, S., Tajima, Y., and Shimozono, T. (2016). A study on soliton fission of Nankai trough tsunami. *Journal of Japan Society of Civil Engineers, Ser. B2.*, 72(2):I_403–I_408.

# Chapter 4

# Data-driven models for tsunami waveforms forecasting

## 4.1 Problem description

In general, the primary purpose of the tsunami early warning system (TEWS) is to predict tsunami waveforms and inundation as quick as possible after a submarine earthquake occurs. A typical method to forecast tsunami waveform is by using the tsunami waveform inversion (TWI). This method is regarded as one of the most suitable methods for tsunami waveform forecasting with robust prediction performance and has been widely used in many studies (e.g. Tsushima et al., 2009, Yasuda and Mase, 2013). Recently, many comprehensive TEWSs usually require a tsunami inundation database, which computed from various fault scenarios, to avoid a high-computational load of the non-linear tsunami simulation in order to forecast tsunami inundation in real-time (e.g. Gusman et al., 2014, Mulia et al., 2018, Setiyono et al., 2017). In this chapter, we focus on tsunami waveform prediction.

The advancement of data-driven techniques, such as neural networks (NNs), has resulted in new approaches as an alternative to the deterministic model. Namekar et al. (2009) used an NN and utilized the precomputed tsunami waveforms for training the NN in advance. Even though it is convenient to be used in real-time, however, we believe that conducting real-time training of the NN against observed data would produce a better forecast. Romano et al. (2009) also used an NN to forecast tsunami height and arrival time in spatial distribution. How-

ever, their proposed method may not be suitable for near-field tsunami events because they rely on the fixed earthquake parameters, which are subjected to uncertainty, as the input of the model. Mase et al. (2011) applied an NN with a single hidden layer to forecast the tsunami height at the observation points. However, for warning and evacuation purposes, in addition to the tsunami height, the information of tsunami arrival time is also essential. Mulia et al. (2016) successfully applied another type of data-driven model, a regularized extreme learning machine (ELM), to predict tsunami waveforms generated by the 2011 Tohoku earthquake. In a real event, their proposed method only requires the information of the location of the earthquake, then utilizes the Green's database as the model input. The result showed that ELM outperforms the TWI method and could capture the nonlinearity of the tsunami. It is widely known that forecasting tsunami waveform generated by an earthquake in real-time is dealing with uncertainty. The uncertainty usually is caused by incomplete information of the source parameters. By applying an ELM as conducted by Mulia et al. (2016), the uncertainty arises due to random parameters (i.e., input weights and biases) inside its network. In other words, each run will produce a different forecast. In a real event, this condition may cause confusion as to which of the forecasts is reliable.

In this study, we improve the method proposed by Mulia et al. (2016). We use a probabilistic regularized extreme learning machine (PRELM), which originally developed to deal with data with noises, to forecast tsunami waveform. We then fine-tune the network parameters to improve the forecast consistency and reduce the uncertainty caused by the randomness of the input weights and biases. Furthermore, we compare the performance of the forecasts with that forecasted by a conventional TWI and another popular data-driven model, the support vector machine (SVM) (Cortes and Vapnik, 1995). We apply our proposed methods to the 2004 Kii earthquake and the 2011 Tohoku earthquake.

## 4.2 Tsunami observational system and bathymetry data

For the 2004 Kii earthquake case, we use the existing tsunami observational system that consists of the ocean bottom pressure (OBP) gauges and global positioning system (GPS) buoys. The OBP gauges were developed and operated by several Japanese agencies. Japan Agency for Marine Earth Science and Technology

(JAMSTEC) installed and operated most of OBP gauges in Nankai Trough called Dense Oceanfloor Network System for Earthquakes and Tsunamis (DONET). The first phase of the DONET program installed 20 stations located off Kii Peninsula and further classified as DONET 1. The second phase of DONET is referred to as DONET 2 consists of 29 stations located on the west side of DONET 1 to cover a wider monitoring region. The Japan Meteorological Agency (JMA) and the National Research Institute for Earth Science and Disaster Prevention (NIED) operated the other OBP gauges other than the DONET system that consisted of 14 stations. The Port and Harbours Bureau, Ministry of Land, Infrastructure, Transport and Tourism (MLIT), Japan operated the GPS buoys through the Port and Airport Research Institute (PARI) (Nagai et al., 2008). The GPS buoys are equipped with real-time kinematic (RTK) technology and able to measure sea-level changes in second. For the 2011 Tohoku earthquake case, we only use six GPS buoys (G801, G802, G803, G804, G806, G807), which also operated by MLIT. The distribution of those existing tsunami observation stations is shown in Fig. 4.1a and c. The bathymetry and topography we use for numerical simulation are based on the General Bathymetric Chart of the Ocean (GEBCO) dataset. The GEBCO 2019 with 15 arcsec resolution is selected. The computational domain ranges from 130° E to 141°E and 30°N to 36°N for the 2014 Kii earthquake case, and from 140° E to 146°E and 36°N to 42°N. The bathymetry map is shown in Fig. 4.1a.

## 4.3 Methodology

### 4.3.1 Tsunami numerical model and Green's function

Similar to TWI, this study utilizes the responses of unit sources distributed inside the influenced area as Green's function. The Green's function database is computed using a numerical model under a linear long-wave (LLW) assumption. The momentum and continuity equations in spherical coordinate system are:

$$\frac{\partial \eta}{\partial t} + \frac{1}{rcos\varphi}\frac{\partial M}{\partial \lambda} + \frac{1}{rcos\varphi}\frac{\partial (Ncos\varphi)}{\partial \varphi} = 0 \tag{4.1}$$

$$\frac{\partial M}{\partial t} + \frac{gd}{rcos\varphi}\frac{\partial \eta}{\partial \lambda} = 0 \tag{4.2}$$

$$\frac{\partial N}{\partial t} + \frac{gd}{r}\frac{\partial \eta}{\partial \varphi} = 0 \tag{4.3}$$

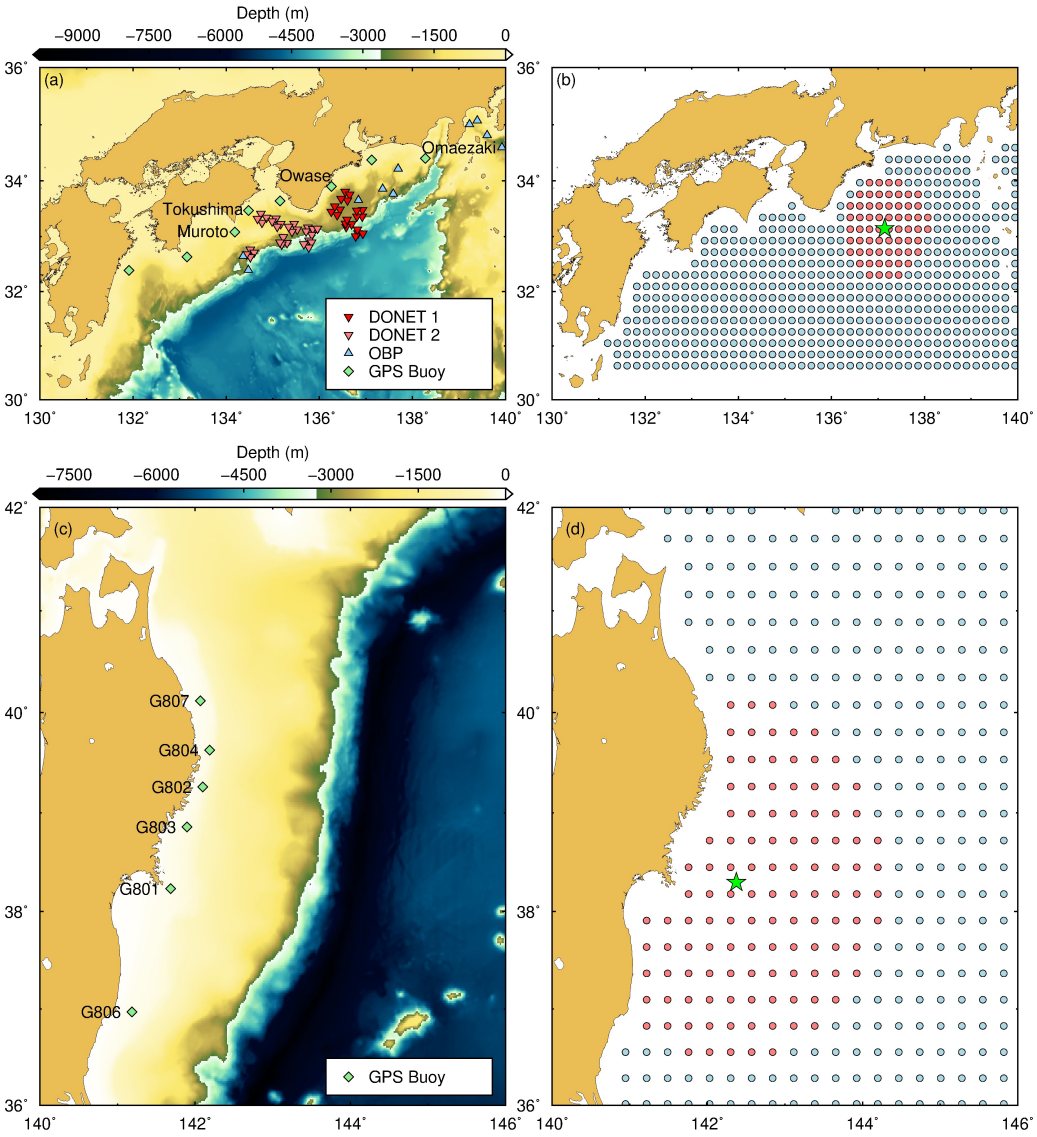


Figure 4.1: (a) Bathymetry profile and existing tsunami observational system in the Nankai region. (b) Unit source locations (blue circles symbol) and selected unit sources in this study (red circles symbol). (c) Bathymetry profile and existing tsunami observational system in the Tohoku region. (d) Unit source locations (blue circles symbol) and selected unit sources in this study (red circles symbol). Star symbol indicates the epicenter of the earthquake

where, $\eta$ is the tsunami height measured from still sea surface, $M$ and $N$ are the components of velocity along $x$ and $y$ directions, $\varphi$ and $\lambda$ are latitude and longitude, $d$ is the water depth, and $g$ is the gravitational constant. We solve these tsunami equations by using a finite difference method with a staggered grid.

To depress artificial reflections from model boundaries that cannot be effectively

absorbed by using traditional boundary conditions, we apply a perfectly matched layer (PML) boundary condition (Maeda et al., 2016). In the numerical simulation, we set the time step ($\Delta t$) is 0.5 s to satisfy the Courant-Friedrichs-Lewy condition with 2 h simulation time.

### 4.3.2 Tsunami waveform inversion

TWI is one of the most robust methods to estimate the initial fault slip of a submarine earthquake that generates tsunami with high accuracy. The reason is that water propagation can be evaluated precisely by using linear or nonlinear long-wave model compared to the seismic propagation, which is dealing with unknown properties within the Earth. In our study, we use TWI to estimate the initial tsunami source instead of a fault model. In this manner, tsunami waveforms in the coastal regions can be predicted directly.

The principle of TWI, synthetic observed tsunami profiles are a linear superposition of wave profiles as Green's function of distributed unit sources with 1 m initial amplitude that are computed using the linear long-wave model. The superposition equation is as follows,

$$\eta(j,t) = \sum_i (G_i(j,t)x_i \quad (0 \leq t \leq T) \tag{4.4}$$

where $\eta(j,t)$ is the observed waveform at the $j$th station, $G_i(j,t)$ is Green's function recorded at the $j$th station from the $i$th unit source, and $x_i$ is the unknown parameter indicating the displacement of the $i$th unit source. We densely distributed unit sources inside the study area with 20 km interval. For each unit source, we apply a Gaussian shape as initial water surface ($z$) with initial amplitude ($A$) of 1 m,

$$z_i(\lambda,\varphi) = A_i exp\left[-\frac{(\lambda-\lambda_i)^2+(\varphi-\varphi_i)^2}{2\sigma^2}\right] \tag{4.5}$$

where $A_i$ is the amplitude with $\lambda_i$ and $\varphi_i$ as the center of the unit source and $\sigma =$ 30 km is the blob spread in $\lambda$ and $\varphi$ directions. To accommodate coseismic seafloor deformation, we modify the Green's function by subtracting initial water surface heights from the synthetic observed tsunami profiles at observation stations. The modification formula as described by Tsushima et al. (2012) is

$$G_i''(j,t) = G_i(j,t) - D_i(j)\int_\infty^t \chi(\delta)d\delta \tag{4.6}$$

where $G_i''(j,t)$ is the modified Green's function, $D_i$ is the initial seafloor deformation, and the term $\int_{\infty}^{t} \chi(\delta) d\delta$ indicates seafloor deformation in temporal evolution, which is set to be 1 for instantaneous tsunami generation.

To estimate the value of xi, we solve Eq. (4.4) by using the singular value decomposition (SVD) method. In vector form, Eq. (4.4) can be written as

$$\boldsymbol{\eta} = \boldsymbol{G}\boldsymbol{x} \tag{4.7}$$

The SVD of $G \in \mathbb{R}^{m \times n}$ is described as $\boldsymbol{G} = \boldsymbol{U}\boldsymbol{\Sigma}\boldsymbol{V}^T$, where $\boldsymbol{U} \in \mathbb{R}^{m \times m}$, $\boldsymbol{\Sigma} \in \mathbb{R}^{m \times n}$, and $\boldsymbol{V} \in \mathbb{R}^{n \times n}$. To avoid overfitting, we minimize both total square loss and regularization term. Now, we can obtain the final objective function, that is,

$$\min_{x} = \left[ \frac{1}{2} \|\boldsymbol{G}\boldsymbol{x} - \boldsymbol{\eta}\|^2 + \frac{\gamma}{2} \|x\|^2 \right] \tag{4.8}$$

where $\gamma > 0$ is the regularization parameter ($\gamma = 1$, in this study) and $I$ is an identity matrix. Finally, the normal equation of Eq. (4.8) is

$$\boldsymbol{x} = \boldsymbol{V}(\boldsymbol{\Sigma}^T\boldsymbol{\Sigma} + \gamma \boldsymbol{I})^{-1}\boldsymbol{\Sigma}^T\boldsymbol{U}^T \tag{4.9}$$

To determine the number of unit sources used in the inversion, we follow the method proposed by Mulia et al. (2016). The unit sources are limited by a circle area with a certain radius defined by the inversion time range. The selected unit sources are $w(t)$, where $(t = r/v) \leq T$, $r$ is the radius of a circle with epicenter as the center, and $v$ is a constant to adjust the size of the circle. We set $v$= 10.5 and 5 km/min after several trial and error tests for the 2004 Kii and 2011 Tohoku earthquake cases, respectively. The selected unit sources are shown in Fig. 4.1c and 1d.

### 4.3.3 Probabilistic extreme learning machine

Similar to the traditional NN, an ELM consists of three layers: input layer, hidden layer, and output layer. In ELM, the input weights that connect input layer and hidden layer are randomly generated. While for the output weights that bridge between hidden layer and output layer are determined by computing the Moore-Penrose generalized inverse matrix. The ELM with $\hat{N}$ hidden nodes can be formulated as

$$\sum_{i=1}^{\hat{N}} = \beta_i g(\boldsymbol{w}_i \boldsymbol{a}_j + b_i) = \boldsymbol{\eta}_j, \quad j = 1, \ldots, N \tag{4.10}$$

where $\beta_i$ is the output weights, $g(\boldsymbol{w}_i \boldsymbol{a}_j + b_i)$ indicates the output of $i$th hidden node with activation function $g$, $\boldsymbol{a}_j = [a_{(j,1}, \ldots, a_{j,n}]^T \in R^n$ is Green's function as used in TWI, which is the waveform at observational stations originating from the $j$th unit source with the number of unit sources $n$, $\boldsymbol{w}_i = [w_{(i,1}, \ldots, w_{i,n}]^T \in R^n$ is the input weights at the $i$th hidden node, $b_i$ is the bias or threshold at the $i$th hidden node. In our study, the training dataset for ELM is $\left\{\boldsymbol{a}_j, \boldsymbol{\eta}_j\right\}_{j=1}^{N}$. For activation function, we use exponential linear units (ELUs) instead of the well-known nonlinear sigmoid function. The ELUs is purposed to avoid the vanishing gradient problem which is caused by a sigmoid function in deep architecture network (Clevert et al., 2016). Even though we use shallow networks in this study, the ELUs is also capable to accelerate the learning process. Considering the dimension of our input function (vector dimension of $\boldsymbol{a}$) is small, and the fact that ELM models require more hidden nodes compared the other neural networks, we set the number of hidden nodes $\hat{N}$ is equal to 80% of the vector dimension of the input function.

The objective function of PRELM minimizes the discrepancy between mean and variance for both modeling error and noise, while the standard ELM only minimizes modeling error (Lu et al., 2018). In other words, the distribution of modeling errors is taken into account. Similar to TWI, to avoid overfitting and provide better model performance, a regulation term can be added (Huang et al., 2012). Finally, the objective function of PRELM can be formulated as

$$\min_{\beta} \left[ \frac{1}{2}\|\beta\|^2 + \frac{1}{2}\frac{\gamma}{N}\sum_{i=1}^{N}(e_i - \zeta)^2 + C\frac{1}{2}\zeta^2 \right] \tag{4.11}$$

where $e_i$ is the modeling error, $\zeta$ is the global error factor which connects among errors, and $\gamma$ and $C$ are the regularization parameters ($\gamma = 2^4$ and $C = 2^3$ in this study). When the number of hidden nodes are smaller than the number of training samples, the output weights $\boldsymbol{\beta}$ of the PRELM can be computed by solving Eq. (4.11),

$$\boldsymbol{\beta} = \boldsymbol{H}^T(\boldsymbol{H}\boldsymbol{H}^2 + \frac{\boldsymbol{I}}{(\gamma/N)} + \frac{\boldsymbol{O}}{C})^{-1}\boldsymbol{\eta} \tag{4.12}$$

where $\boldsymbol{O}$ is a matrix of ones whose elements are 1.

### 4.3.4 Fine-tuning

As mentioned in the beginning, predicting tsunami waveform generated by an earthquake in real-time is dealing with uncertainty due to limited information

of the earthquake source parameters. The ELM is also one of the uncertainty sources since the input weights and biases are defined randomly. Similar to a standard neural network, the most common way to reduce the uncertainty caused by randomness in ELM architecture is by updating or adjusting the network weights and biases according to the output error.

Once the network parameters (input weight, bias, and output weight) are initialized using PRELM, we then optimize them by using the adaptive moment estimation (Adam) optimizer (Kingma and Ba, 2015). The initial network parameters for optimization are computed by using the PRELM algorithm during the training stage. Since the network parameters are relatively well-defined because they have been trained in advance, Adam optimization should be done quickly. Besides, Adam is well-known as a rapid optimizer and suitable for a wide range of optimization problems in the machine learning field (Wilson et al., 2017). Hereafter, we call the fine-tuned PRELM the PRELM-FT.

### 4.3.5 Support vector machine

SVM is one of the emerging learning models in the past two decades due to its outstanding capability in solving classification problems. Cortes and Vapnik (1995) concluded that SVM could be viewed as a type of SLFNs after conducting a rigorous study about the relationship between SVM and deep architecture feedforward model. In this study, we decide to use $\nu$-support vector regression ($\nu$-SVR) (Schölkopf et al., 2000), a variant of SVM for regression problems. For a given similar training dataset as in ELM $\left\{\boldsymbol{a}_j, \boldsymbol{\eta}_j\right\}_{j=1}^{N}$, where $\boldsymbol{a}_j = [a_{(j,1}, \ldots, a_{j,n}] \in R^n$, $\nu$-SVR can be analytically modelled as

$$\hat{\boldsymbol{w}}\boldsymbol{a} + b = f(\boldsymbol{a}) \tag{4.13}$$

where $\hat{\boldsymbol{w}}$ is the vector variable and $b$ is the bias. We can see that the formulation of $\nu$-SVR is similar to the ELM (Eq. 4.10), and the vector variable matrix of $\hat{\boldsymbol{w}}$ resembles the input weights $\boldsymbol{w}$. The objective function of $\nu$-SVR with regularization term is

$$\begin{aligned} \min_{\hat{w},b,\xi,\xi^*,\epsilon} & \left[\frac{1}{2}\hat{\boldsymbol{w}}^T\hat{\boldsymbol{w}} + \gamma\left(\nu\epsilon + \frac{1}{n}\sum_{i=1}^{n}(\xi + \xi^*)\right)\right] \\ s.t.\ & (\hat{\boldsymbol{w}}^T\phi(\boldsymbol{a}_i) + b) - \eta_i \leq \epsilon + \xi\backslash 1\backslash_i, \\ & \eta_i - (\hat{\boldsymbol{w}}^T\phi(\boldsymbol{a}_i) + b) \leq \epsilon + \xi_i^* \\ & \xi_i, \xi_i^* \geq i = 1, \ldots, n,\ \epsilon \geq 0 \end{aligned} \tag{4.14}$$

where $\nu$ is the SVM constant ($\nu$=0.1, in this study), $\epsilon$ is the error at each $a_i$ or indicates the tube size of the SVM with everything above $\epsilon$ is defined as slack variables (e.g. $\xi_i$,$\xi_i^*$), $\gamma$ is the regularization parameter, and $\phi$ denotes nonlinear mapping into a higher-dimensional feature space. According to Karush-Kuhn-Tucker (KKT) theorem, solving the following dual problem is equivalent to train the SVM, that is,

$$\begin{aligned} &\min_{\alpha,\alpha^*} \left[\frac{1}{2}(\boldsymbol{\alpha}-\boldsymbol{\alpha}^*)^T Q(\boldsymbol{\alpha}-\boldsymbol{\alpha}^*) + \boldsymbol{\eta}^T(\boldsymbol{\alpha}-\boldsymbol{\alpha}^*)\right] \\ &s.t.\ \boldsymbol{O}^T(\boldsymbol{\alpha}-\boldsymbol{\alpha}^*) \le 0,\ \boldsymbol{O}^T(\boldsymbol{\alpha}-\boldsymbol{\alpha}^*) = \hat{\gamma} n \nu, \\ &0 \le \alpha_i, \alpha_i^* \le \hat{\lambda},\ i = 1, \ldots, n \end{aligned} \tag{4.15}$$

where $Q_{ij} = K(a_i, a_j) \equiv \phi(a_i)^T \phi(a_j)$, $\hat{\gamma} = \gamma/n$, $\boldsymbol{O}$ is a matrix of ones whose elements are 1, and $\alpha_i$ and $\alpha_i^*$ are Lagrange multipliers. The solution to Eq. (4.15) is

$$\sum_{i=1}^{n} (-\alpha_i + \alpha_i^*)^T K(\boldsymbol{a}_i, \boldsymbol{a}) + b \tag{4.16}$$

We use a Gaussian radial basis function (RBF), a general-purpose kernel function, and applicable for most problems. The RBF is usually used when the knowledge about the data is unknown before the learning process. The RBF kernel is expressed as follows,

$$K(a_i, a_j) = e^{-\gamma \|a_i - a_j\|^2} \tag{4.17}$$

where $\gamma = 1/n$ is the parameter of the RBF function ($\gamma = 0.1$, in this study).

## 4.4 Experimental results and discussion

To evaluate the performance of the models, we compare the observed and forecasted waveforms by calculating the Pearson correlation coefficient ($r$) and root mean square errors (RMSE). We also compute the accuracy score (Tsushima et al., 2009) of the tsunami forecasting using the following equation.

$$\text{accuracy score} = \left[1 - \frac{\sum_{j=1}^{N} (\eta_j - \hat{\eta}_j)^2}{\sum_{j=1}^{N} \eta_j^2}\right] \tag{4.18}$$

where $\eta_j^2$ is the forecasted waveform. Generally, a higher accuracy score indicates a better accuracy of the forecasts. Furthermore, we compare tsunami arrival time and maximum wave height at selected GPS buoy locations as testing points (Fig. 4.1d) since these are very important indicators for early warning. Aside

from that, we include scatter plots for further analysis and interpretation of the proposed models.

To test the performance of our proposed models, we conduct two experimental cases, the 2004 Kii and the 2011 Tohoku earthquakes. The fault model of the 2004 Kii earthquake is obtained from Yamanaka (2004), which is computed from teleseismic body waves. Because no OBPs were installed at the time of the 2004 Kii tsunami, we use synthetic data for the 2004 Kii earthquake case by conducting a numerical simulation. By assuming seafloor deformation is equal to the initial water surface profile, we use Okada's model (Okada, 1985) to calculate the tsunami source model. The simulated waveforms recorded at observational stations are assumed as a pseudo-observation that will be used to quantify our model performance. The observational system in the Nankai region consists of GPS buoy and OBP, which are not free from noises or outliers. To provide realistic data, we add white Gaussian noise to every observation station. Since the noise level of OBP is generally lower than the GPS buoy, we set a signal-to-noise ratio of 30:1 for OBP calculated from the ratio between maximum wave amplitude and standard noise deviation as similarly used by Mulia et al. (2017) and slightly larger ratio of 30:5 for GPS buoy. For the 2011 Tohoku earthquake case, we use a real tsunami data. The data has been preprocessed to remove the non-tsunami components such as seismic waves and tides.

It is evident that in any inversion process, data with longer inversion time range will improve the forecast accuracy. We define the inversion time period of 10 min for the 2004 Kii earthquake case, and 35 min for the 2011 Tohoku earthquake case according to Gusman et al. (2014). By using that period of data, we forecast 50 min tsunami waveform at testing points (Fig. 4.1a and c). We select four GPS buoy stations (Muroto, Tokushima, Owase, and Omaezaki) and six stations (G801, G802, G803, G804, G806, G807) as the testing points for the 2004 Kii and 2011 Tohoku earthquake cases, respectively.

It is worth noting that PRELM, PRELM-FT, and SVM models should be carefully optimized by adjusting the parameters to obtain the best performance of the models. For the PRELM and PRELM-FT, besides requiring more hidden nodes, the accuracy of the forecasting is affected by regularization parameters. In the SVM model, the model accuracy is affected by the SVM constant $\nu$ and RBF parameter $\gamma$. In this study, those parameters are optimized by conducting a grid-search method. Because those are user-controlled parameters, in a real event, however, those parameters need to be adjusted through trial and error

procedure, since there is no certain rule to determine the best value.

### 4.4.1 The comparisons of PRELM and PRELM-FT

In terms of the model formulation, the PRELM is similar to the model proposed by Mulia et al. (2016), with only slightly different in the computation of the distribution of modeling error. Both models rely on the randomization of the input weights and biases, as Huang et al. (2006) presented that the approximation capability of ELM can be achieved when the inputs are projected randomly. However, in this manner, the prediction from each run would be different. In the context of a warning system, in addition to the accuracy of the predictions, prediction consistency is also important. To give more consistent predictions, therefore, the network parameters of the PRELM need to be fine-tuned. Once the PRELM is trained, we then optimize the network parameters by using Adam optimizer. Since the network has been trained in advance, the optimization procedure only requires 10-30 iterations to achieve reliable results. To evaluate the benefits of fine-tuning the PRELM, we conduct 50 consecutive runs to quantify the uncertainty of the predictions. Both of PRELM and PRELM-FT are implemented using an open-source machine learning library, Tensorflow (Abadi et al., 2016).

Comparisons between PRELM, PRELM-FT, and observation are shown in Fig. 4.2 and 4.3 for the 2004 Kii and 2011 Tohoku earthquake, respectively. In the figure panel, the light blue and red shaded areas represent the prediction variability areas bounded by $10^{th}/90^{th}$ percentiles for the 2004 Kii and 2011 Tohoku earthquakes, respectively, while the solid lines represent their means. For both earthquake cases, it can be observed that the predictions from 50 consecutive runs of the PRELM are highly variable. For the 2004 Kii earthquake case, the PRELM exhibits significant variability of the predictions relative to the maximum observed tsunami height. A similar condition also applies to the 2011 Tohoku earthquake case. However, PRELM shows relatively low prediction variability at the time between 0-35 min, which most likely occurred because the predictions are within the inversion time range. Furthermore, PRELM-FT, which is a fine-tuned PRELM, successfully reduces the variability of the predictions. The areas bounded by $10^{th}/90^{th}$ percentiles are hardly seen for the predictions by the PRELM-FT indicating consistent predictions. Therefore, the level of the uncertainty of the PRELM prediction caused by random parameters of the network can be significantly reduced by fine-tuning the network parameters. Hereafter, we assume the mean of the results of 50 PRELM consecutive runs as the PRELM

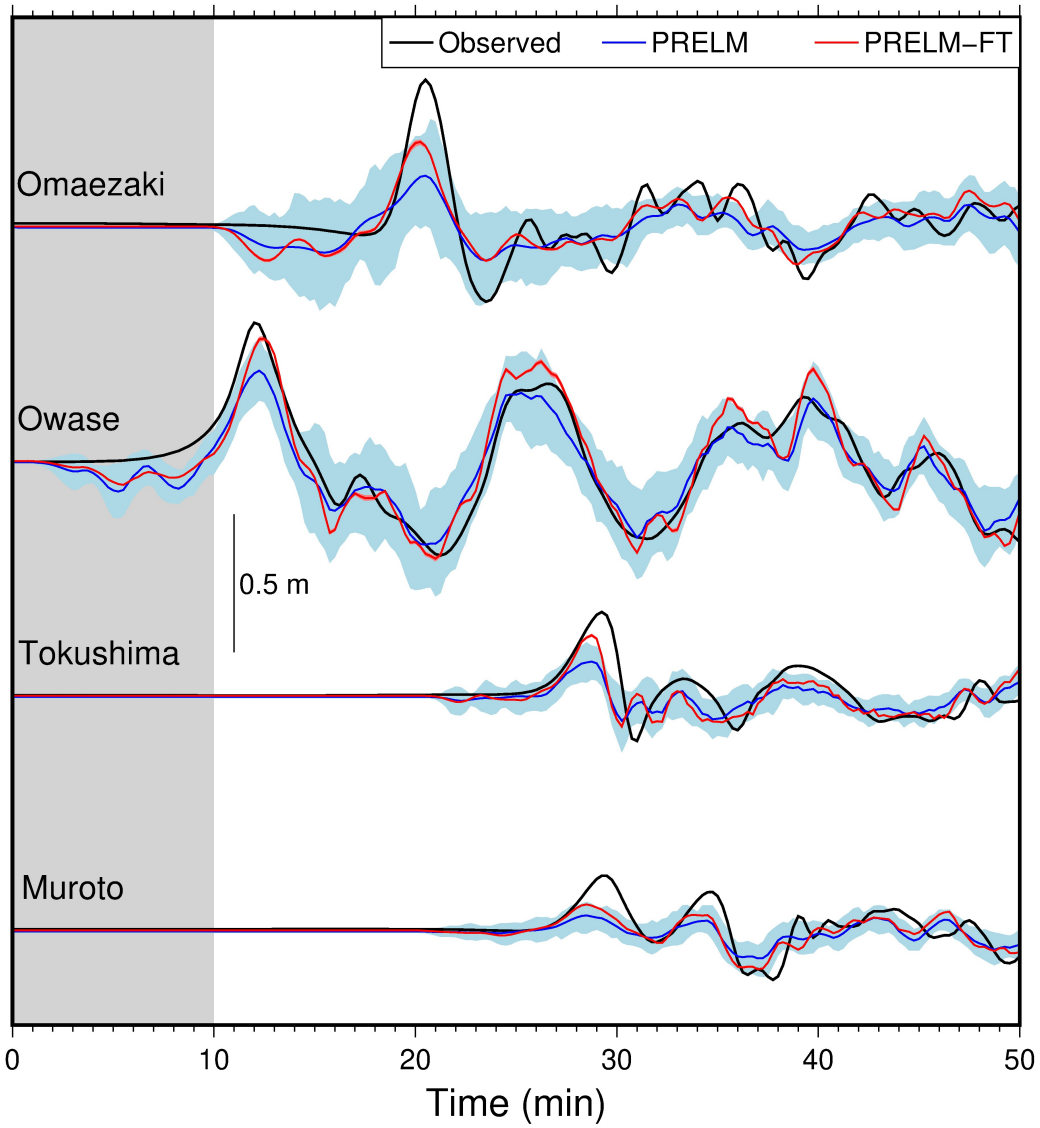


Figure 4.2: Comparison of forecasted waveforms between PRELM, PRELM-FT, and the observations at the testing stations for the 2004 Kii earthquake. The grey shaded area indicates the training period. The shaded areas around the graph indicate the area bounded by $10^{th}/90^{th}$ percentiles for PRELM and PRELM-FT forecasts, while the solid lines indicate the mean from 50 consecutive runs.

forecast, while only from a single run for the other models, since the variability is neglectable.

### 4.4.2 All models comparisons

Overall, all of the models produce reliable and similar tendencies in capturing the pattern of the observed tsunami waveforms. The comparisons of the forecasted

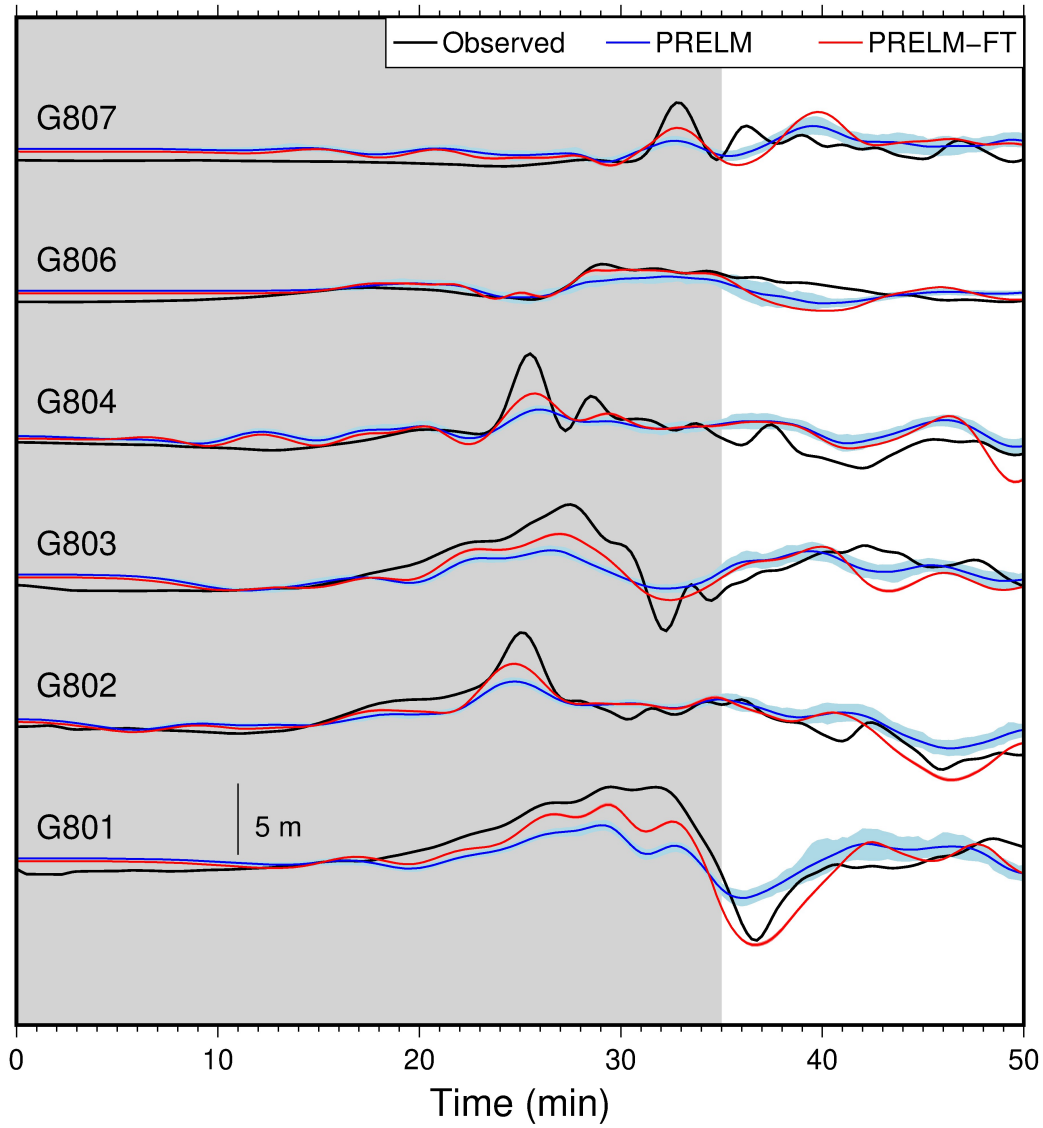


Figure 4.3: Comparison of forecasted waveforms between PRELM, PRELM-FT, and the observations at the testing stations for the 2011 Tohoku earthquake. The grey shaded area indicates the training period. The shaded areas around the graph indicate the area bounded by $10^{th}/90^{th}$ percentiles for PRELM and PRELM-FT forecasts, while the solid lines indicate the mean from 50 consecutive runs.

waveform from all proposed models and observations are shown in Fig. 4.4 and 4.5 for the 2004 Kii and 2011 Tohoku earthquake cases, respectively. To provide a clear judgment of the performance of the models, we assess three essential indicators: the accuracy of tsunami waveform, maximum tsunami amplitude, and arrival time. Furthermore, to quickly determine which data-driven model performs the best, we then give a rank to each data-driven models. The rank is calculated based on the accuracy score. For each tsunami case, the lowest rank

at each testing station is one point, and the highest rank is equal to the number of the testing station. The ranking results of the models are shown in Fig. 4.6 and 4.7.

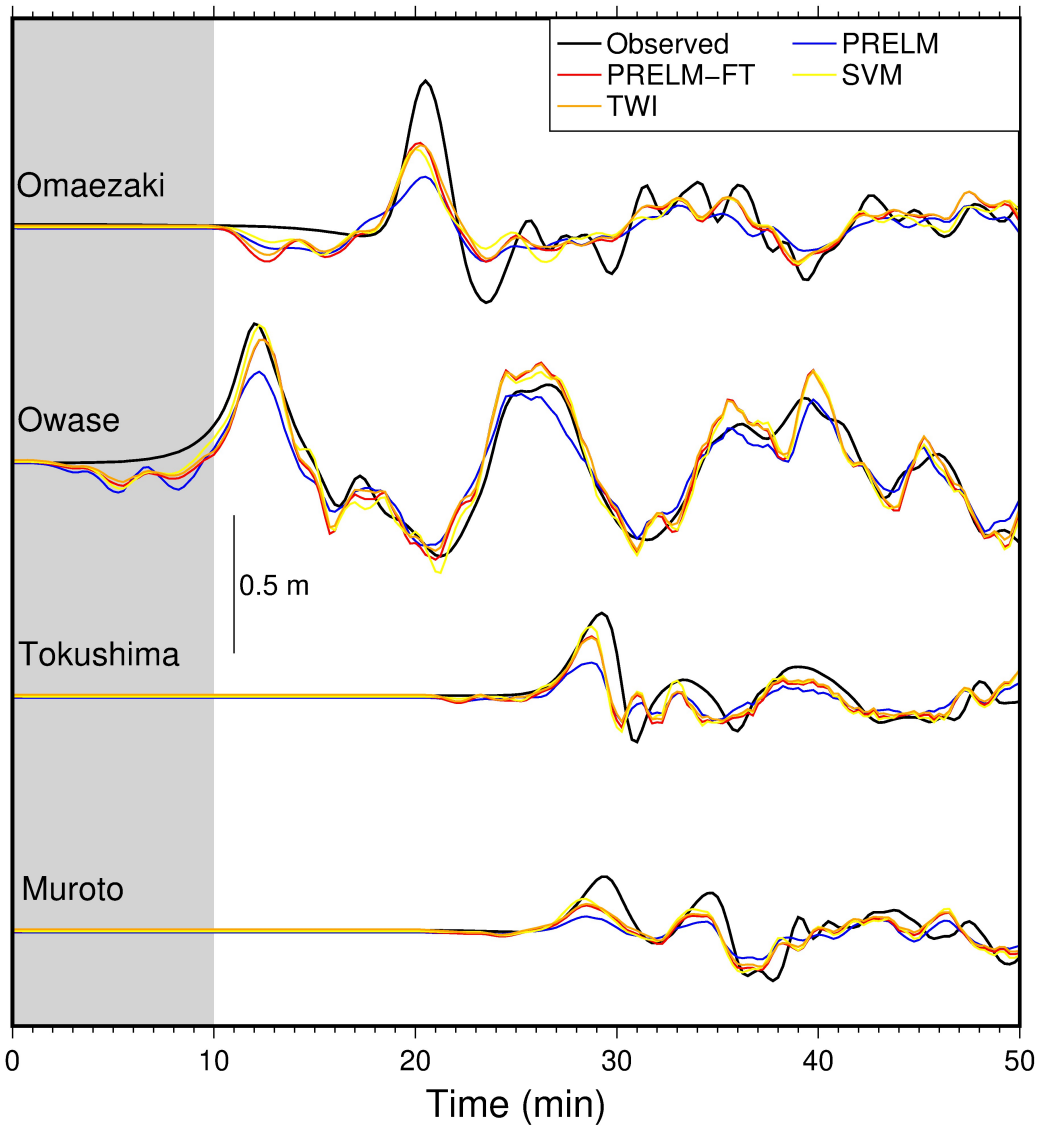


Figure 4.4: Comparison of forecasted waveforms between PRELM, PRELM-FT, SVM, TWI, and the observations at the testing stations for the 2004 Kii earthquake. Shaded area indicates the training period.

It is clear from Fig. 4.4 that the forecasts from the proposed data-driven models for the 2004 Kii earthquake possess a similar tendency. TWI and followed by the PRELM-FT successfully provide the best waveform prediction accuracy, as indicated with the highest rank shown in Fig. 4.6a. It is also evident that SVM tends to forecast maximum tsunami amplitudes closer to the observations at most of the testing stations (also indicated by the highest rank shown in

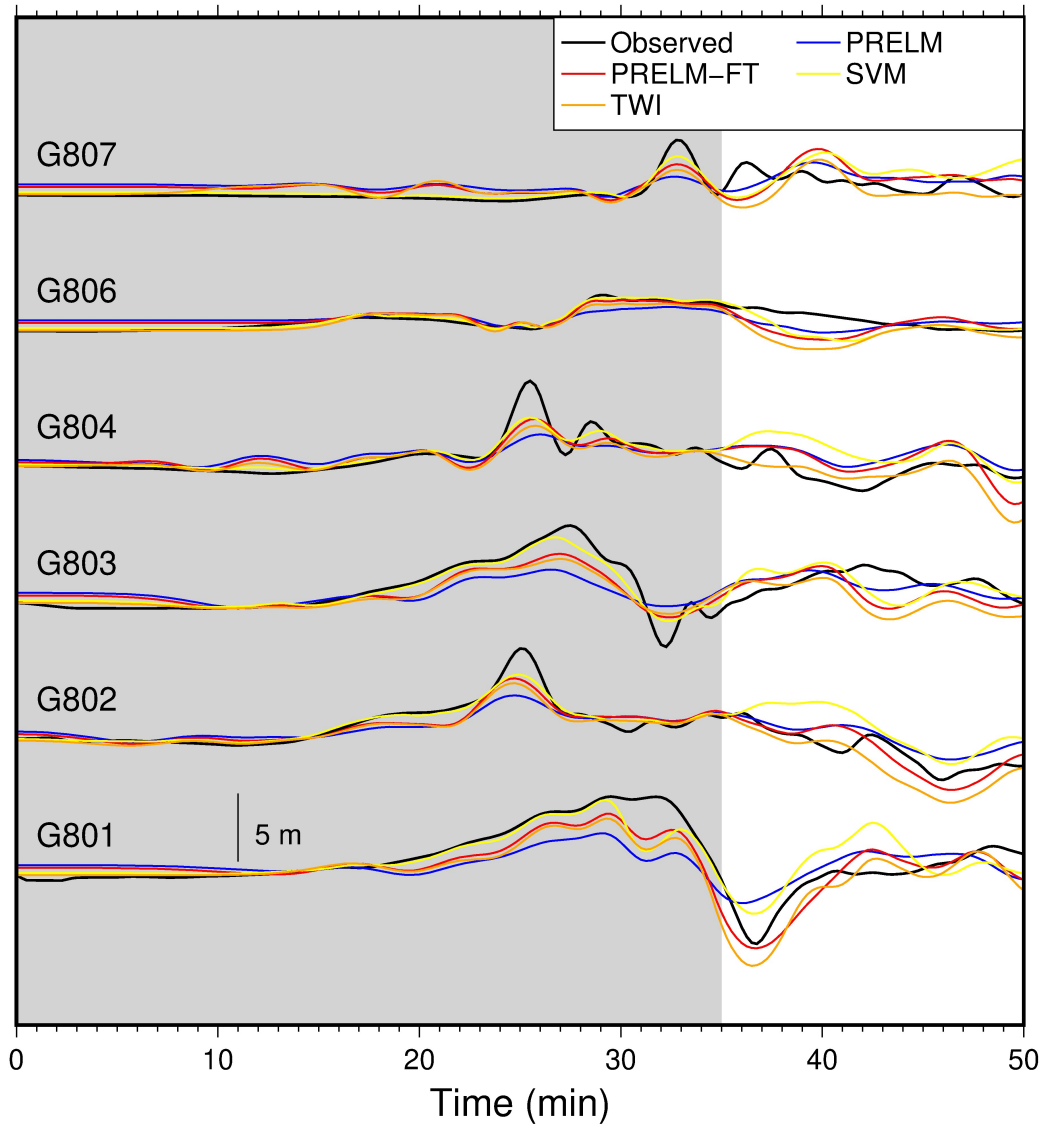


Figure 4.5: Comparison of forecasted waveforms between PRELM, PRELM-FT, SVM, TWI, and the observations at the testing stations for the 2011 Tohoku earthquake. Shaded area indicates the training period.

Fig 4.6b), except at Omaezaki that slightly outperformed by PRELM-FT. The PRELM outperforms the other models in terms of the accuracy of the tsunami arrival time, as indicated in Fig. 4.6c, though it is clearly shown in Fig. 4.4 that the difference is not significant. According to the total ranks of the data-driven models, the PRELM-FT performs the best, while PRELM shows the lowest rank (Fig. 4.6d). For the 2011 Tohoku earthquake case, PRELM-FT and followed by SVM produces the highest waveform and tsunami arrival time accuracy compared to the other proposed models (Fig. 4.7a and c). Similar to the 2004 Kii earthquake case, the SVM can capture the maximum tsunami height better than the other models (Fig. 4.7b). From both earthquake cases, PRELM-FT obtains the highest

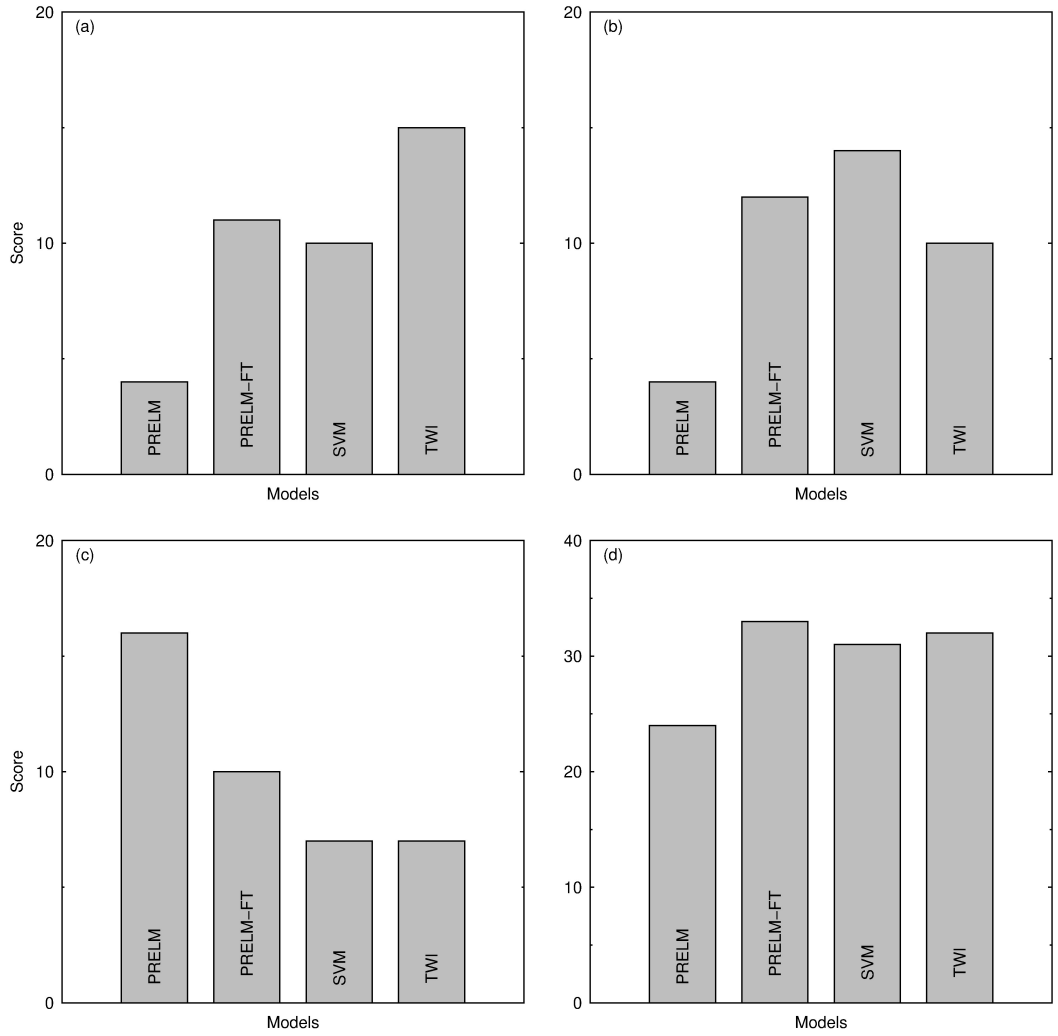


Figure 4.6: The performance rank of the models for the 2004 Kii earthquake. (a) The rank for tsunami waveform accuracy. (b). The rank for maximum tsunami amplitude accuracy. (c) The rank for tsunami arrival time accuracy. (d) The total rank.

ranking, indicating that PRELM-FT is superior to the other models. However, in terms of maximum tsunami height accuracy, SVM is better.

Additionally, to further investigate the performance of the proposed methods, we include the scatter and Gaussian fit plot for each method as presented in Fig. 4.8 and 4.9 for the 2004 Kii and 2011 Tohoku earthquake cases, respectively. In the 2004 Kii earthquake case, PRELM-FT, SVM, and TWI produce forecasts which have a relatively similar distribution and agreement with the observation (Fig. 4.8). They also show similar performance indicated by similar statistical measures (RMSE and $r$), while PRELM has the lowest performance. For the case of the 2011 Tohoku earthquake, the PRELM-FT forecast shows the most similar

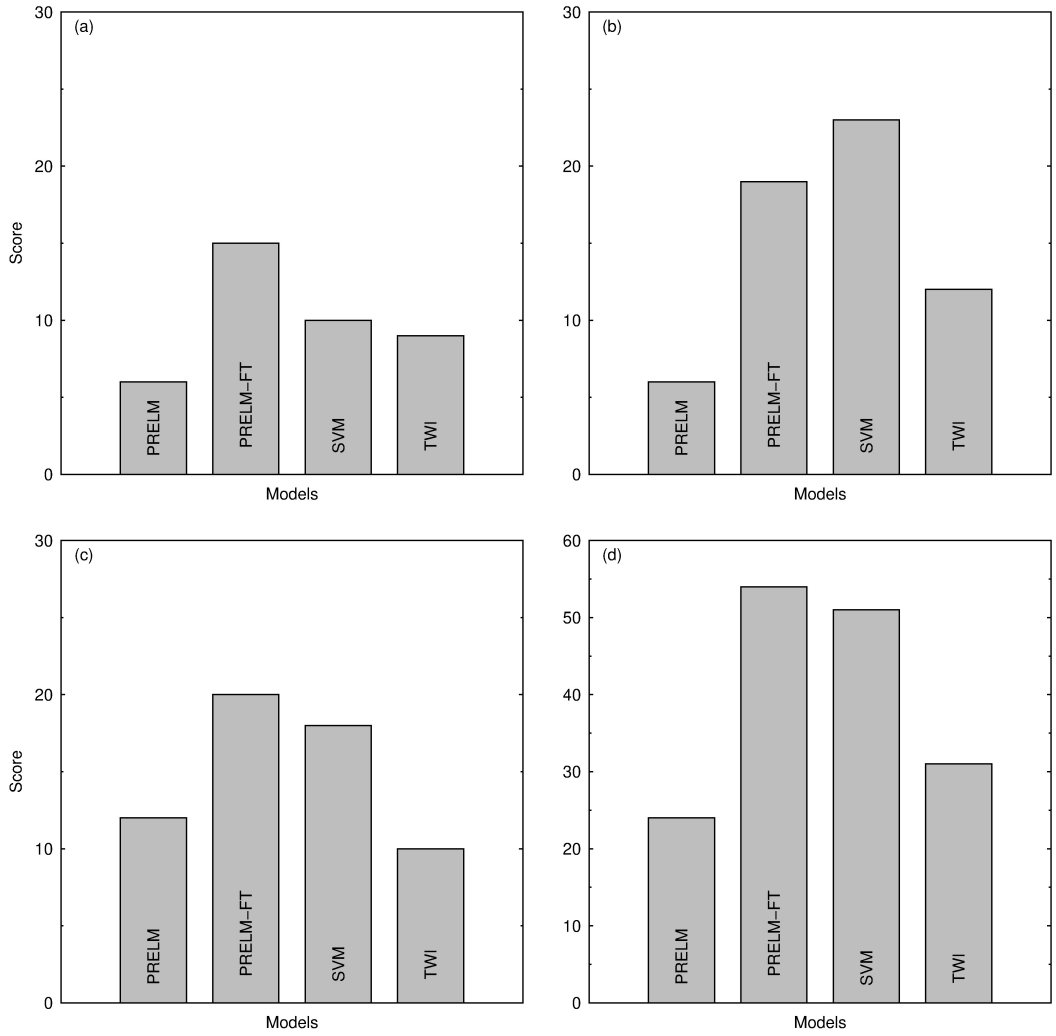


Figure 4.7: The performance rank of the models for the 2011 Tohoku earthquake. (a) The rank for tsunami waveform accuracy. (b). The rank for maximum tsunami amplitude accuracy. (c) The rank for tsunami arrival time accuracy. (d) The total rank.

distribution with the observation compared to the other models as shown in the Gaussian fit plot (Fig. 4.9). It also yields the best performance indicated by the statistical measures.

Most of the comparisons of evaluation indicators reveal that PRELM-FT can achieve more accurate predictions. However, imposing Adam optimizer into PRELM-FT makes the training time longer due to the iteration process. PRELM-FT requires 0.8 s of training time, which is longer than PRELM (0.07 s), SVM (0.3 s), and TWI (0.3 s). Applying ELUs as the transfer function, the PRELM presents remarkable training time, faster than that in the previous study (0.35 s) (Mulia et al., 2016). Also, PRELM-FT as the other NN-based networks are

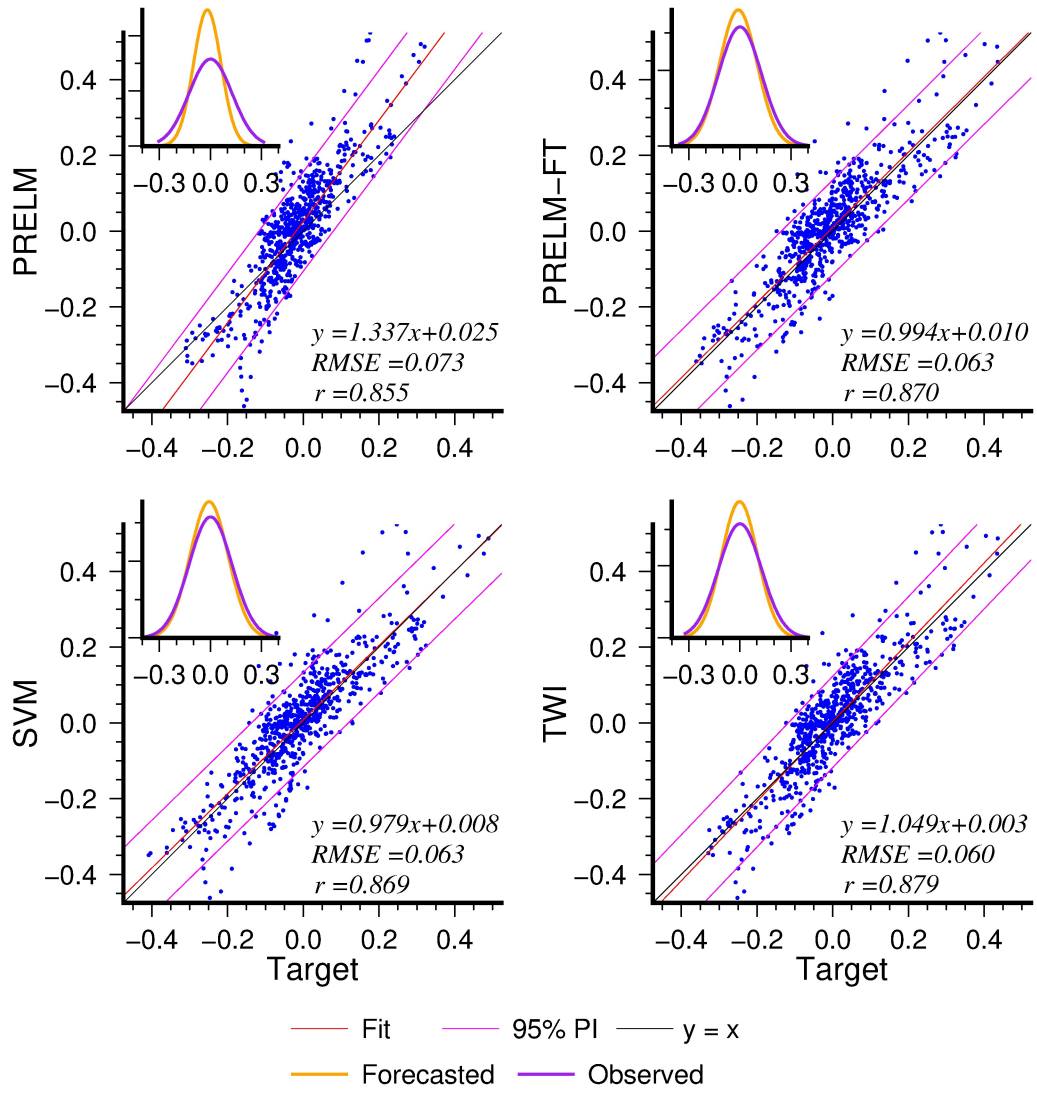


Figure 4.8: Scatter plots and Gaussian fits resulted by the proposed methods versus the observations for the 2004 Kii earthquake.

prone to overfitting and higher probability to converge in local minima. Unlike NN, SVM is more resistant to overfitting and able to find the global optimum solution during the training process. Therefore, with faster training time and a slightly different performance with the PRELM-FT, SVM is also a promising method for real-time tsunami waveform forecasting.

All of the models perform very well with RMSE $< 1$ and $r > 0.8$ for the 2004 Kii earthquake. Apart from the coseismic deformation of the 2004 Kii earthquake is relatively less complicated compared to the 2011 Tohoku earthquake, the deployment of dense OBP (DONET) system may improve the accuracy of prediction. Following the 2011 Tohoku event, an advance and dense OBP network called

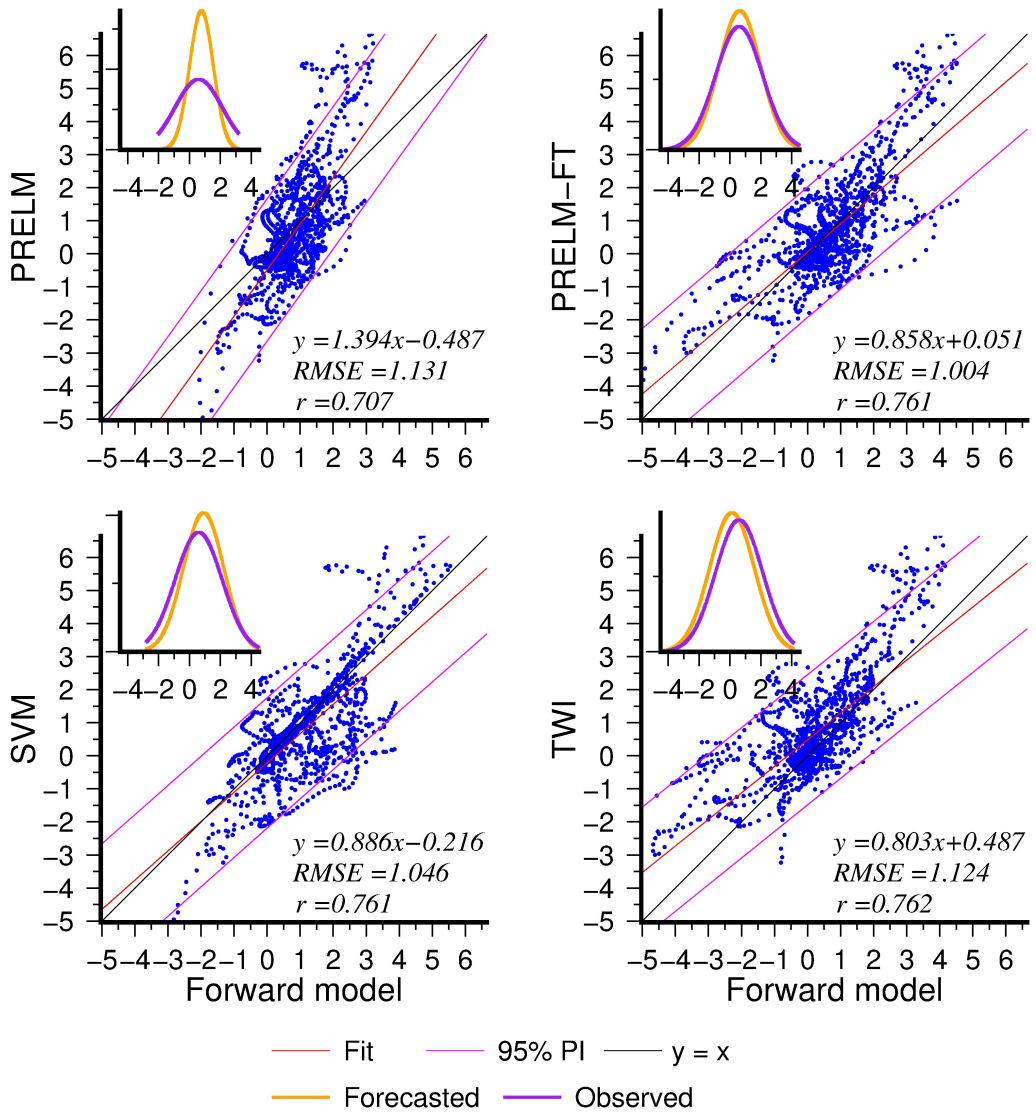


Figure 4.9: Scatter plots and Gaussian fits resulted by the proposed methods versus the observations for the 2011 Tohoku earthquake.

S-net is also installed around Japan Trench which covers a wide area of the eastern coast of Japan with 30-50 km grid spacing (Maeda et al., 2015, Saito, 2013). Therefore, the prediction performance for the 2011 Tohoku earthquake case may improve when the S-net is included.

The advantages of our proposed methods over the published model (Mulia et al., 2016) is that it provides consistent prediction. PRELM and the other variants of conventional ELM would produce a different result for each run. Therefore, conventional ELM may not be suitable for early warning systems, in which the prediction consistency is an essential factor. In this study, the unit sources included in the inversion are determined by limiting the unit sources with a certain

radius with the earthquake coordinate as the center. However, this method may not represent the actual coseismic deformation as the epicenter of the earthquake is not always at the center of the deformation area. Therefore, incorporating a fast optimization procedure to select the unit sources is suggested for future development. Both of the 2004 Kii and 2011 Tohoku earthquake exhibit dispersive effects, as presented in the previous study (Saito et al., 2014, 2010). Even though it requires a high computational load, applying a dispersive model in developing the Green's function database may provide more accurate predictions.

## 4.5 Summary

This study presents an application of data-driven models including, PRELM, PRELM-FT, and SVM for robust forecasting of tsunami waveform in real-time. The basic idea of the PRELM is similar to the method proposed by Mulia et al. (2016), which also uses an ELM variant. The difference is that the input parameters of the previous study are randomly assigned, while the input parameters in this study are then iteratively-optimized by using Adam optimizer. Consequently, in the previous study, each model run would produce a different prediction which may not be suitable for early warning tasks. In addition to producing a quick and accurate prediction, the TEWS also requires a consistent prediction to avoid confusion during a real event. With fully-trained network parameters, the PRELM-FT can yield a better forecast with a significant improvement than PRELM. PRELM-FT is also superior to TWI and another popular data-driven model, SVM, indicated by the highest rank in two earthquake cases. However, due to the iteration procedure during the optimization, the PRELM-FT requires more computational time. In terms of waveform forecasting accuracy, PRELM shows the best performance; however, in terms of maximum tsunami height accuracy, SVM outperforms the other methods. Therefore, with faster training time than PRELM-FT, SVM is also a promising method for future tsunami waveform forecasting tool.

Overall, PRELM-FT and SVM are strong candidates for the future TEWS tool by considering its good approximation. In the future, we should focus on improving the performance of the method by using a more sophisticated procedure in selecting and developing the Green's function.

# References

Abadi, M., Barham, P., Chen, J., Chen, Z., Davis, A., Dean, J., Devin, M., Ghemawat, S., Irving, G., Isard, M., Kudlur, M., Levenberg, J., Monga, R., Moore, S., Murray, D. G., Steiner, B., Tucker, P., Vasudevan, V., Warden, P., Wicke, M., Yu, Y., Zheng, X., Brain, G., Osdi, I., Barham, P., Chen, J., Chen, Z., Davis, A., Dean, J., Devin, M., Ghemawat, S., Irving, G., Isard, M., Kudlur, M., Levenberg, J., Monga, R., Moore, S., Murray, D. G., Steiner, B., Tucker, P., Vasudevan, V., Warden, P., Wicke, M., Yu, Y., and Zheng, X. (2016). TensorFlow: A System for Large-Scale Machine Learning. In *12th USENIX conference on Operating Systems Design and Implementation*, pages 265–283.

Clevert, D.-A., Unterthiner, T., and Sepp, H. (2016). Fast and accurate deep network learning by exponential linear units (ELUs). In *International Conference on Learning Representations*.

Cortes, C. and Vapnik, V. (1995). Support-vector networks. *Machine Learning*, 20(3):273–297.

Gusman, A. R., Tanioka, Y., Macinnes, B. T., and Tsushima, H. (2014). A methodology for near-field tsunami inundation forecasting: Application to the 2011 Tohoku tsunami. *Journal of Geophysical Research: Solid Earth*, 119(11):8186–8206.

Huang, G. B., Zhou, H., Ding, X., and Zhang, R. (2012). Extreme learning machine for regression and multiclass classification. *IEEE Transactions on Systems, Man, and Cybernetics, Part B: Cybernetics*, 42(2):513–529.

Huang, G.-B., Zhu, Q.-y., Siew, C.-k., and Ã (2006). Extreme learning machine: Theory and applications. *Neurocomputing*, 70:489–501.

Kingma, D. P. and Ba, J. L. (2015). Adam: A method for stochastic gradient descent. *ICLR: International Conference on Learning Representations*.

Lu, X., Ming, L., Liu, W., and Li, H. X. (2018). Probabilistic regularized extreme learning machine for robust modeling of noise data. *IEEE Transactions on Cybernetics*, 48(8):2368–2377.

Maeda, T., Obara, K., Shinohara, M., Kanazawa, T., and Uehira, K. (2015). Successive estimation of a tsunami wavefield without earthquake source data: A data assimilation approach toward real-time tsunami forecasting. *Geophysical Research Letters*, 42:7923–7932.

Maeda, T., Tsushima, H., and Furumura, T. (2016). An effective absorbing boundary condition for linear long-wave and linear dispersive-wave tsunami simulations. *Earth, Planets and Space*, 68(63).

Mase, H., Yasuda, T., and Mori, N. (2011). Real-Time Prediction of Tsunami Magnitudes in Osaka Bay, Japan, Using an Artificial Neural Network. *Journal of Waterway, Port, Coastal, and Ocean Engineering*, 137(5):263–268.

Mulia, I. E., Asano, T., and Nagayama, A. (2016). Real-time forecasting of near-field tsunami waveforms at coastal areas using a regularized extreme learning machine. *Coastal Engineering*, 109:1–8.

Mulia, I. E., Gusman, A. R., and Satake, K. (2017). Optimal Design for Placements of Tsunami Observing Systems to Accurately Characterize the Inducing Earthquake. *Geophysical Research Letters*, 44(24):12106–12115.

Mulia, I. E., Gusman, A. R., and Satake, K. (2018). Alternative to non-linear model for simulating tsunami inundation in real-time. *Geophysical Journal International*, 214:2002–2013.

Nagai, T., Shimizu, K., Sasaki, M., and Murakami, M. (2008). Improvement of the Japanese NOWPHAS network by introducing advanced GPS buoys. In *Proceedings of the 18th International Offshore and Polar Engineering Conference*, pages 558–564.

Namekar, S., Yamazaki, Y., and Cheung, K. F. (2009). Neural network for tsunami and runup forecast. *Geophysical Research Letters*, 36:L08604.

Okada, Y. (1985). Surface deformation due to shear and tensile faults in a half-space. *Bulletin of the Seismological Society of America*, 75(4):1135–1154.

Romano, M., Liong, S. Y., Vu, M. T., Zemskyy, P., Doan, C. D., Dao, M. H., and Tkalich, P. (2009). Artificial neural network for tsunami forecasting. *Journal of Asian Earth Sciences*.

Saito, T. (2013). Dynamic Tsunami generation due to sea-bottom deformation: Analytical representation based on linear potential theory. *Earth, Planets and Space*.

Saito, T., Inazu, D., Miyoshi, T., and Hino, R. (2014). Dispersion and nonlinear effects in the 2011 Tohoku-Oki earthquake tsunami. *J. Geophys. Res. Oceans*, 119:5160–5180.

Saito, T., Satake, K., and Furumura, T. (2010). Tsunami waveform inversion including dispersive waves: The 2004 earthquake off Kii Peninsula, Japan. *Journal of Geophysical Research: Solid Earth*, 115(B6).

Schölkopf, B., Smola, A. J., Williamson, R. C., and Bartlett, P. L. (2000). New support vector algorithms. *Neural Computation*, 12(5):1207–1245.

Setiyono, U., Gusman, A. R., Satake, K., and Fujii, Y. (2017). Pre-computed tsunami inundation database and forecast simulation in Pelabuhan Ratu, Indonesia. *Pure and Applied Geophysics*, 178(8):3219–3235.

Tsushima, H., Hino, R., Fujimoto, H., Tanioka, Y., and Imamura, F. (2009). Near-field tsunami forecasting from cabled ocean bottom pressure data. *Journal of Geophysical Research: Solid Earth*, 114:B06309.

Tsushima, H., Hino, R., Tanioka, Y., Imamura, F., and Fujimoto, H. (2012). Tsunami waveform inversion incorporating permanent seafloor deformation and its application to tsunami forecasting. *Journal of Geophysical Research: Solid Earth*, 117(B3).

Wilson, A. C., Roelofs, R., Stern, M., Srebro, N., and Recht, B. (2017). The marginal value of adaptive gradient methods in machine learning. In *Advances in Neural Information Processing Systems*.

Yamanaka, Y. (2004). EIC Seismology Note No. 153.

Yasuda, T. and Mase, H. (2013). Real-Time Tsunami Prediction by Inversion Method Using Offshore Observed GPS Buoy Data: Nankaido. *Journal of Waterway, Port, Coastal, and Ocean Engineering*, 139(3).

# Chapter 5

# Deep predictive coding network for wavefields forecasting

## 5.1 Problem description

Tsunami forecasting systems have advanced significantly in recent years, especially since the 2004 Indian Ocean and 2011 Tohoku tsunamis. In most forecasting systems, information on the earthquake source parameters, that is, earthquake coordinates, depth and fault size, are necessary to run the tsunami propagation model (Satake, 2015). Calculating the earthquake source parameters from seismic observations in real-time is a difficult task because of the complexity of the structure beneath the Earth. Even though the parameters can also be calculated using the waveform inversion method (Satake, 1989), it still requires many trials and errors to find the best-fit fault configuration. With the vast deployment of offshore observation stations in recent years, many studies prefer tsunami forecasting systems that estimate sea surface deformation instead of the earthquake source mechanisms (Titov et al., 2005, Tsushima et al., 2011). Several studies have proposed comprehensive forecasting systems that use a tsunami database to forecast tsunami inundation caused by a near-field earthquake (Gusman et al., 2014, Mulia et al., 2018, Setiyono et al., 2017). However, these studies are not free from uncertainty in estimating the tsunami source.

Real-time data transmission through a high density of observational instruments interconnected with a cabled network has been conducted in Japan for more than a decade to provide tsunami predictions. In the Nankai region, the Dense

Oceanfloor Network System for Earthquakes and Tsunamis, which is a cabled network for tsunami and seismic measurement, has been extended to cover a wider region (Baba et al., 2014, Kaneda et al., 2015). A new cabled network, S-Net (Yamamoto et al., 2016), is currently being installed in the Japan Trench, and some operations were started in 2016.

With the availability of dense observation stations, Maeda et al. (2015) first proposed a data assimilation (DA) method which was able to forecast tsunami wavefields without the need to know information on the earthquake source parameters by utilizing the observed tsunami amplitude. The technique was introduced to avoid uncertainties in estimating the tsunami source. The method was successfully implemented for the 2011 Tohoku earthquake. However, besides requiring a dense observation network, it also has a high computational cost because of the direct linear long-wave (LLW) numerical simulation. To reduce the computational cost, Wang et al. (2017) used a Green's function database to speed up the assimilation process. However, unlike the original tsunami DA, the method was not developed to predict the tsunami wavefield, but only to synthesize waveforms at points of interest. An improved DA was presented by Yang et al. (2019) with an even higher computational cost because of the introduction of the ensemble Kalman filter into the model.

Here we conduct a numerical experiment by integrating a deep predictive coding network (Lotter et al., 2017) with the DA. The method was initially used in the computer vision field to predict future video frames. In this study, the predictive coding network is used to predict the next time steps of the tsunami wavefield utilizing a short sequence of the previously assimilated wavefield. In this manner, tsunami propagation after the last assimilated wavefield is estimated by the predictive coding network. Like the other typical data-driven methods, the computational time of the predictive coding network is short. The method reduces the computational time for DA; this enables the tsunami wavefield and arrival time at the coastal region to be predicted within a short time. We first developed a tsunami propagation database from predefined scenarios to train the predictive coding network. To evaluate the performance of our proposed method, we conducted experiments with two cases: simple bathymetry, and the 2011 Tohoku earthquake.

## 5.2 Methodology

In this study, DA is combined with the deep predictive coding network to quickly estimate tsunami wavefield. The proposed method can also be viewed as a hybrid method between DA and deep predictive coding network. At first, the deep predictive coding needs to be trained by using a database. The database consists of DA-assimilated wavefield from a set of predefined scenarios. In the application, when a tsunami generated by submarine earthquake occurs, from the observed tsunami at a dense observational stations, the DA can directly assimilated the wavefield. However, since the computational cost of the DA is very high, the DA is unable to quickly forecast the future wavefield with an ordinary computational machine. At this point, the deep predictive coding network will take over the prediction process. The deep predictive coding network requires the DA-assimilated tsunami wavefields, but only in a short sequence, as the the input. By using a short sequence of the DA-assimilated wavefield, the deep predictive coding network will forecast the future sequence wavefield based on the acquired knowledge during the training process. In other words, the prediction by the deep predictive coding network is independent from the DA. Since the prediction process of the predictive coding network is a matrix multiplication task, a longer wavefield estimation can be obtained with a minimum computational cost. The flowchart of the application of the proposed method is shown in Fig. 5.1. The detailed explanation of the DA and deep predictive coding network as well as the training database are shown in the following sub-sections.

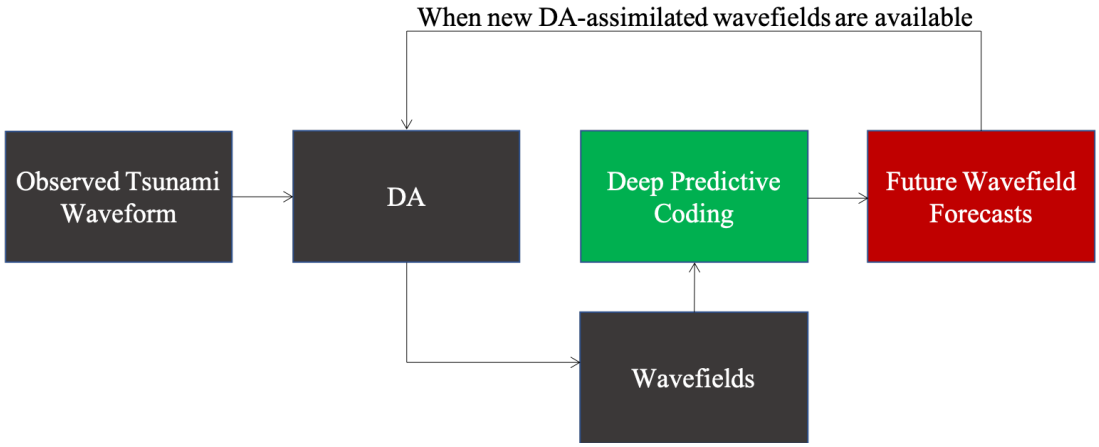


Figure 5.1: The flowchart of the application of hybrid DA and deep predictive coding network for tsunami wavefield forecasting

### 5.2.1 Data assimilation

The sequential DA method has been widely used in weather forecasting (Kalnay, 2002). The tsunami DA method proposed by Maeda et al. (2015) for simulating tsunami wavefields in real-time is based on the optimal interpolation method, which has a lower computational cost than the more advanced method using the ensemble Kalman filter, under the assumption that the system is linear. Even though the optimal interpolation method is simple, however, the DA approach showed good agreement with real tsunami data (Gusman et al., 2016, Heidarzadeh et al., 2019, Wang et al., 2019, 2017) and the synthetic case (Mulia et al., 2017). In the numerical simulation, the tsunami wavefield at the nth time step is represented as $\boldsymbol{x}_n(\eta(n\Delta t, x, y), M(n\Delta t, x, y), N(n\Delta t, x, y))$, where $\eta$ is the tsunami height, $M$ and $N$ are the velocities in the $x$ and $y$ directions and $\Delta$t is the time step. The DA method can be expressed as

$$\boldsymbol{x}_n^f \equiv \boldsymbol{F}\boldsymbol{x}_{n-1}^a \tag{5.1}$$

$$\boldsymbol{x}_n^a = \boldsymbol{x}_n^f + \boldsymbol{W}(\boldsymbol{y}_n - \boldsymbol{H}\boldsymbol{x}_n^b) \tag{5.2}$$

At each time step, the forecasted tsunami wavefield $\boldsymbol{x}_n^f$ at the $n$th time step is computed by numerically solving linear long wave theory in Cartesian coordinates using the assimilated wavefield at the previous time step $\boldsymbol{x}_{n-1}^a$. The vector $\boldsymbol{F}$ is the propagation matrix, which corresponds to the 2-D LLW tsunami propagation model. The residual between the observed tsunami amplitude and the forward simulation at the observation station $\boldsymbol{y}_n$ is calculated as $(\boldsymbol{y}_n - \boldsymbol{H}\boldsymbol{x}_n^f)$. $\boldsymbol{H}$ is a vector that has a value of 1 at the observation stations and zero at the other elements, and is used to extract the forecasted tsunami height at the observation stations. The residual is then multiplied by the smoothing matrix $\boldsymbol{W}$ to bring the assimilated wavefield closer to the observed tsunami wavefield. The smoothing matrix is an essential factor in DA as it controls the quality of the assimilated wavefield. We compute the smoothing matrix by solving the following equation:

$$\boldsymbol{W} = \boldsymbol{P}\boldsymbol{H}^T + (\boldsymbol{H}\boldsymbol{P}\boldsymbol{H}^T - \boldsymbol{R})^{-1} \tag{5.3}$$

where $P^f = \langle \varepsilon^f \varepsilon^{fT} \rangle$ and $\boldsymbol{R} = \langle \varepsilon^O \varepsilon^{OT} \rangle$ are the error covariance matrices of the forward simulation and the observations, respectively. $\varepsilon^f$ and $\varepsilon^O$ are the Gaussian errors of the forward simulation and observations, respectively, while $\varepsilon^{fT}$ and $\varepsilon^{OT}$ are the corresponding transpose matrices.

By iteratively solving Eqs. (5.1) and 5.2, the tsunami wavefield is assimilated, and we can obtain forecasted tsunami waveforms at any location inside the model domain during and after the assimilation process.

### 5.2.2 Deep predictive coding networks

Traditionally, static images are used to train computer vision models. However, in the real world, the visual world involves spatiotemporal movement. As a complex system, the human brain is continuously making spatiotemporal predictions based on the incoming sensory stimuli, and this is mirrored in the concept of predictive coding (Friston and Kiebel, 2009, Rao and Ballard, 1999). Predictive coding networks were initially developed by Lotter et al. (2017) based on this concept, but reformulated in recent deep learning techniques, and trained using a gradient descent method with an implicitly embedded loss function. A network consists of several repeating stacked layers that make local predictions of the input to the modules. The difference between the actual input and this prediction then proceeds to the higher layer. The architecture of the proposed method is shown in Fig. 5.2. Each level of the network is composed of four main components: an input convolutional unit ($A_l$), a recurrent representation unit ($R_l$), a prediction unit ($\hat{A}_l$) and an error representation unit ($E_l$). The recurrent representation unit $R_l$ estimates the prediction $\hat{A}_l$ of the input $A_l$. The error unit $E_l$ computes the difference between $A_l$ and $\hat{A}_l$, and then passes it to the next layer of the network as input $A_{l+1}$. The representation unit $R_l$ receives a copy of the error matrix $E_l$ along with the input from the representation unit of the higher layer $R_{l+1}$, which is then used to estimate future predictions.

$$A_l^t = \begin{cases} x_t & l = 0 \\ maxpool\left(ELU(conv(E_{l-1}^t))\right) & l > 1 \end{cases} \tag{5.4}$$

$$\hat{A}_l^t = ELU\left(conv(R_l^t)\right) \tag{5.5}$$

$$E_l^t = \left[ELU(A_l^t - \hat{A}_l^t); ELU(\hat{A}_l^t - A_l^t)\right] \tag{5.6}$$

$$R_l^t = convLSTM(E_l^{t-1}, R_l^{t-1}, upsample(R_{l+1}^t)) \tag{5.7}$$

Predictive coding networks initially focused on image sequences in video data. In this study, we use the assimilated tsunami wavefields from the DA process. Considering a sequence from the assimilated tsunami wavefield $x_t$ as the input to the model, the target for the lowest layer of the network is set to the input sequence itself, that is $A_0^t = x_t \forall t$. Except for layer 0, the targets for the higher layers $A_l^t$ are determined by a convolution of error units from the lower layer $E_{l-1}^t$, which is followed by an exponential linear unit (ELU) activation function (Clevert et al., 2016) and max-pooling, as described in Eq. (5.4). After several experiments, we found that the ELU activation function is more suitable for our study than the rectified linear unit function that was used in the original model. We used the convolutional long short-term memory (convLSTM) units (Hochreiter

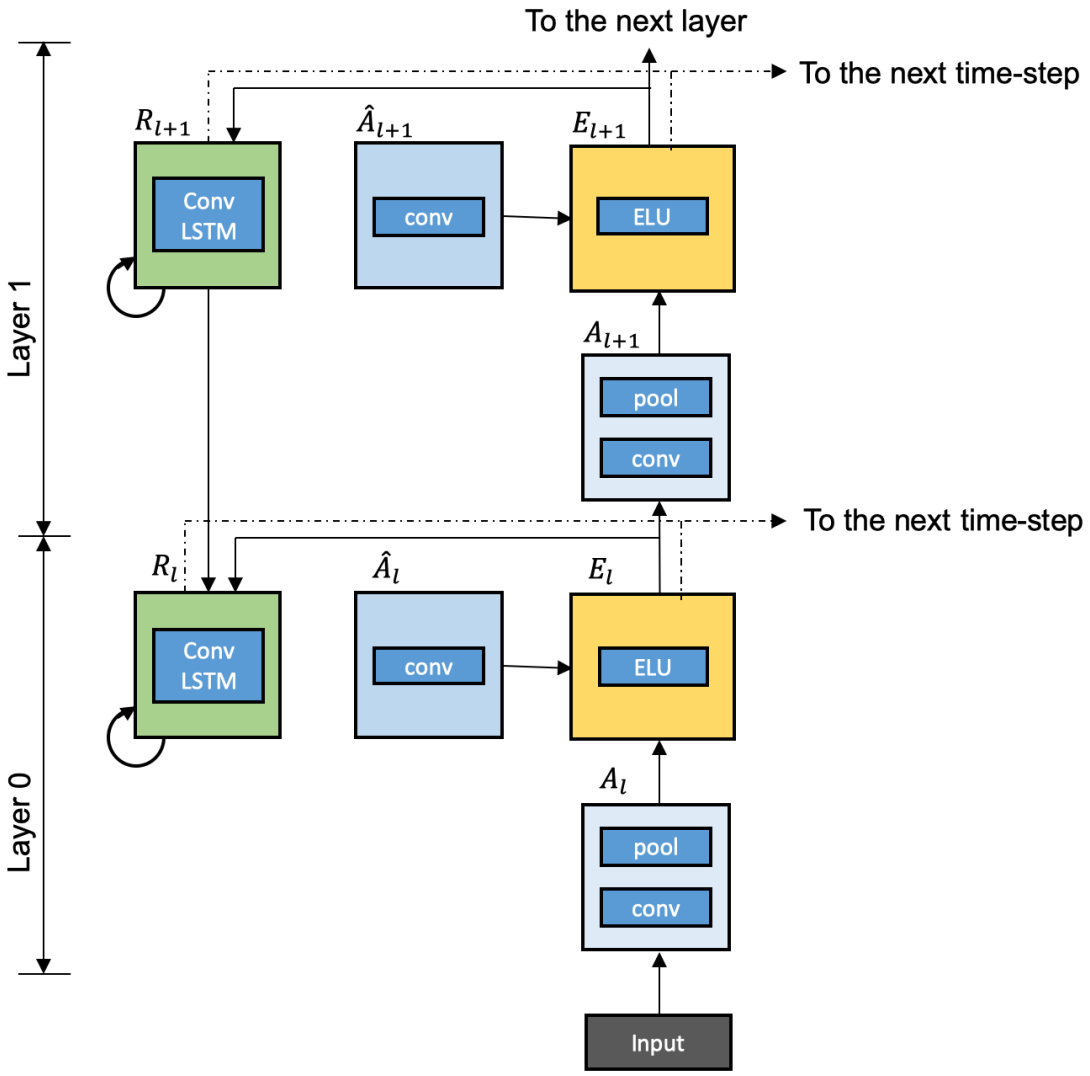


Figure 5.2: Architecture of the deep predictive coding network

and Schmidhuber, 1997, Shi et al., 2015) as the backbone for the representation units. Then $R_l^t$ is determined by the representation from the previous time step $R_l^{t-1}$, $E_l^{t-1}$, as well as $R_{l+1}^t$ (Eq. (5.7)). $R_{l+1}^t$ should go through an upsampling procedure because of the max-pooling in $A_l^t$ units. The predictions $\hat{A}_l^t$ are estimated through a convolution of $R_l^t$ and followed by an ELU activation function (Eq. (5.5)). Finally, the error units $E_l^t$ are computed from the difference between $A_l^t$ and $\hat{A}_l^t$ and then divided into ELU-activated positive and negative values (Eq. (5.6)). The model is trained by minimizing the sum of the error units.

First, we develop a database from multiple predefined scenarios to train the model. The scenario and experiment settings are explained in the next section. For each scenario, we simulate the tsunami propagation using the LLW tsunami model. The synthesized tsunami heights at every time step ($\Delta t = 1$ s) are used to estimate the tsunami wavefield through the assimilation process using Eq. (5.1).

Once the assimilation process has started, we use the assimilated wavefield from those scenarios with 1 min intervals to train the model. Since the proposed algorithm learns the pattern of the tsunami propagation during the training process, we would expect the model to behave similarly to the tsunami propagation model. The predictive coding network in this study was composed of four layers of networks with $3 \times 3$ filter sizes, and channel sizes of 1, 48, 96 and 192 for each layer. The model was trained using a gradient descent based optimization technique, RMSprop (Hinton et al., 2012), with a learning rate $\alpha$ of 0.001, decreasing by a factor of 10 halfway through the training process.

## 5.3 Numerical implementation and results

To quantify the prediction accuracy of the proposed method, the forecasted wavefields are compared to the assimilated wavefield computed by DA. However, quantitative assessment of the generative models is a complex problem (Theis et al., 2016), and we adopted a structural similarity index measurement (SSIM) (Wang et al., 2004) to measure the model performance quantitatively. SSIM is currently widely used in the image vision field to provide a clear judgment of the similarity between two images:

$$SSIM(x, y) = \frac{(2\mu_x\mu_y + C_1)(2\sigma_{xy} + C_2)}{(\mu_x^2 + \mu_y^2 + C_1)(\sigma_x^2 + \sigma_y^2 + C_2)} \tag{5.8}$$

where $\mu_x$ and $\mu_y$ are the averages of the images $x$ and $y$, respectively and $\sigma_x^2$ and $\sigma_y^2$ are the variances of $x$ and $y$, respectively. $C_1 = (k_1 L)^2$ and $C_2 = (k_2 L)^2$ are two variables that are designed to avoid a zero denominator, while $L$ is the dynamic range of the pixel values and $k_1 = 0.01$ and $k_2 = 0.03$ are constants. SSIM is a signed expression ranging between –1 and 1, with a larger value indicating a greater similarity. We also used a conventional statistical measure, the root mean square error (RMSE), which measures the average magnitude of the prediction error.

### 5.3.1 Simple bathymetry

To assess the performance of our proposed method, we conducted a numerical experiment with a simple bathymetry profile as the simplest case. The numerical domain is shown in Fig. 5.3. We set a mild bathymetry slope of 0.33% with a

shallowest depth of 1000 m and a deepest of 2000 m. The size of the numerical domain was 300 km in the x and y directions with a grid width of $\delta x = \delta y = 1000$ m. We set an array of 25 virtual stations as a dense observation station is typically required by the conventional DA method to provide a good assimilation result. The distance between observation points in the $x-$ and $y$-directions was 15 km. We used a two-dimensional cosine basis function (Hossen et al., 2015) for the initial water surface:

$$\eta_i = \frac{\eta_0}{4}\left[1 + cos\left(\frac{\pi(x - x_0)}{L}\right)\right]\left[1 + cos\left(\frac{\pi(y - y_0)}{L}\right)\right],\ -L \leq x_i, y_i \leq L, \tag{5.9}$$

where $L$ is the characteristics source size, and we chose $L$= 70 km. The maximum initial height $\eta_0 = 1$ at $x = x_o$ and $y = y_o$, which is the center of the source. This basis function provide a more compact solution than the conventional Gaussian basis function used in Chapter 4 and previous studies (e.g. Mulia et al., 2016, Saito et al., 2010).

Three scenarios of the initial tsunami sources were used; two for the training, and one for testing purposes. The location of the initial tsunami sources for training and testing is shown in Fig. 5.3. For training, we first simulated the tsunami propagation using the LLW tsunami model. Assuming the recorded waveform at observation stations as the observed data, once the tsunami signal had been recorded at the stations, the assimilation process had started, and we concatenated the assimilated wavefield with 1 min intervals from those two scenarios as the training input. We found that a training the model with a training epoch of 350 was enough to provide a good representation of the database. The training epoch represents the number of cycle of the feedforward and backpropagation computation in a traditional NN, which requires about 1 h computational time. Similarly, for the prediction, once the assimilation process had begun, four assimilated tsunami wavefields with an interval of 1 min originating from the testing scenario were used as the input to the model. We configured the model using four assimilated wavefields, enabling the model to predict the next four steps in the wavefield.

A comparison between the predictions, DA, and forward modeling is shown in Fig. 3. We set the initial water surface at $t = 0$ as the tsunami source. When the tsunami reached the observation stations, in this case, at $t = 11$ min, the data assimilation started. Here we used four assimilated wavefields starting from $t = 11$ min to 14 min (Fig. 5.4a) to predict the next four frames of the wavefield, i.e., $t = 15$ to 18 min (Fig. 5.4b). From the comparison, the estimated wavefields are visually very similar to the DA (Fig. 5.4c). The model can mimic the charac-

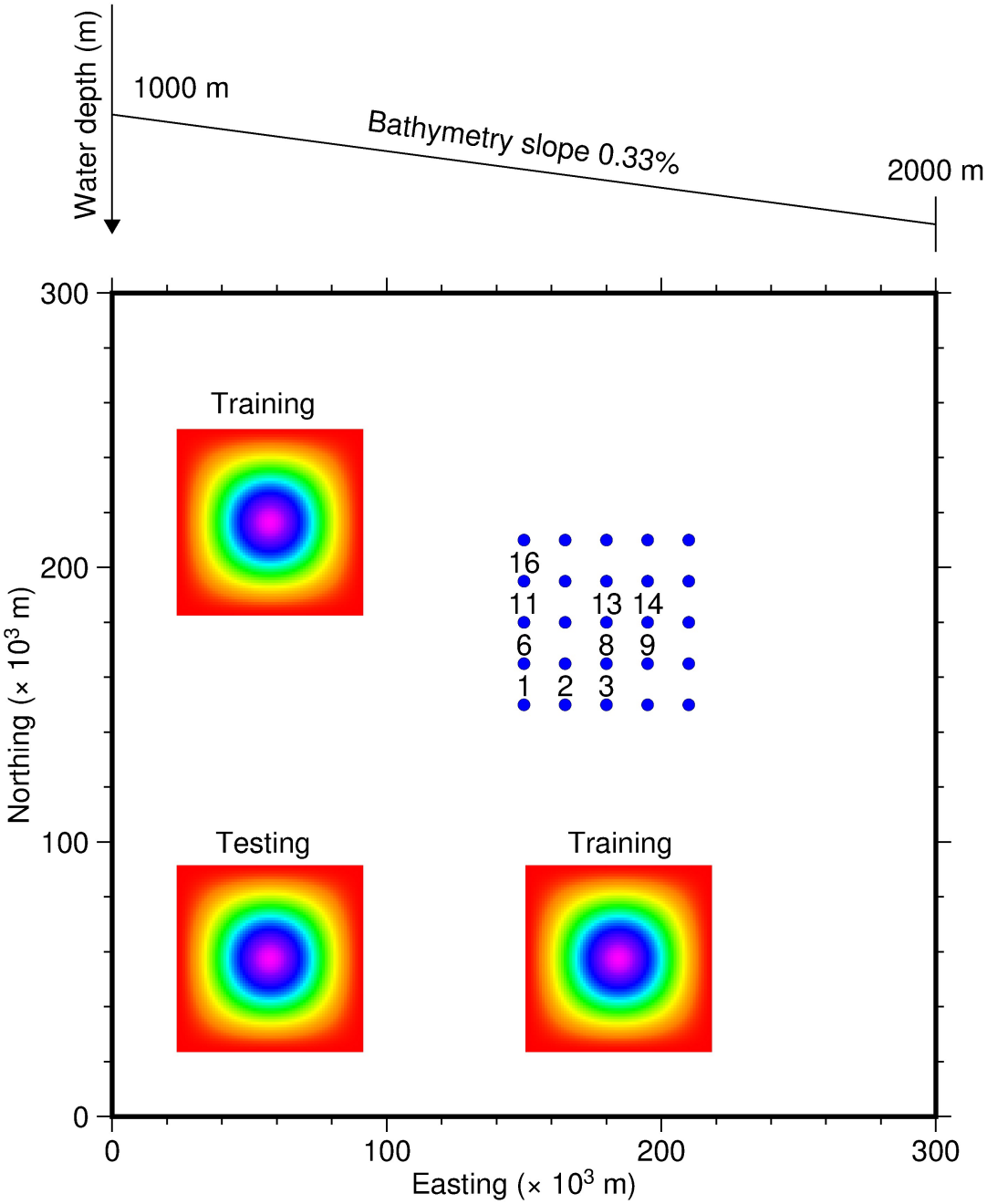


Figure 5.3: Domain of the simple bathymetry case. The colored area indicates the location of the cosine basis function of the initial water surface for training and testing purposes. The blue dots indicate the array of the observation stations.

teristics of the DA indicated with SSIM and RMSE values ranging from 0.891 to 0.960 and 0.02 to 0.06 m, respectively. We included quantile-quantile (Q-Q) plots to further analyze the differences between the forecasts and DA (Fig. 5.5). The Q-Q plots suggest that the forecasts had a similar distribution to the DA. We also randomly selected ten observation stations and compared the recorded waveforms produced by the proposed method and DA (Fig. 5.5). The selected stations are

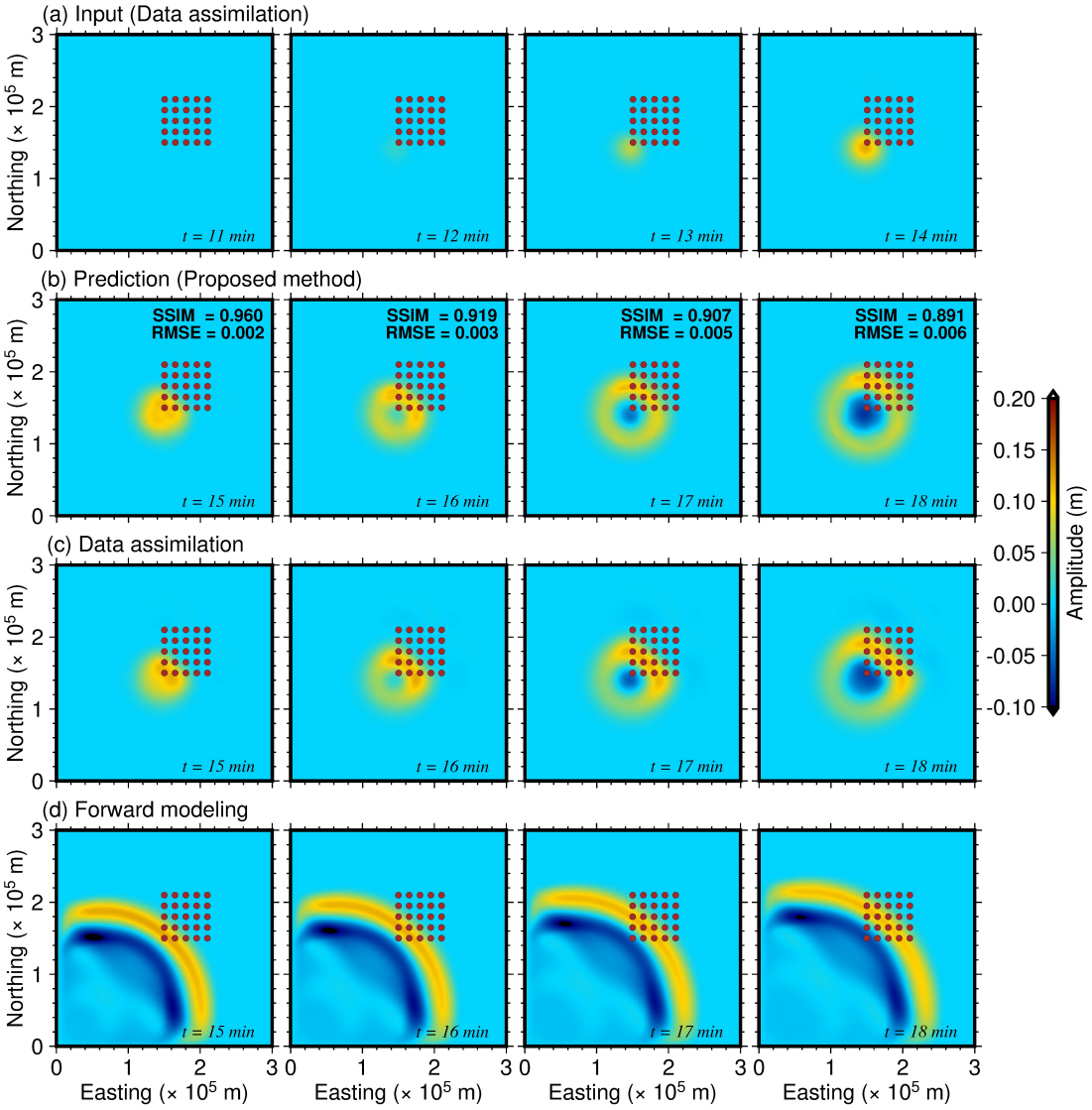


Figure 5.4: Comparisons of the wavefields for the model input and the estimated wavefields from the proposed method, DA and forward modeling for the simple bathymetry case. (a) Input to the model; (b) Forecasted tsunami wavefields; (c) Assimilated tsunami wavefields; (d) Results of forward modeling

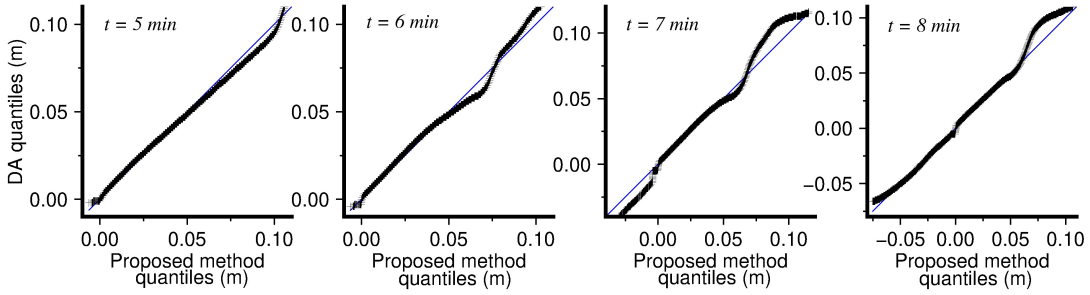


Figure 5.5: Q-Q plots between the proposed method and DA for the simple bathymetry case

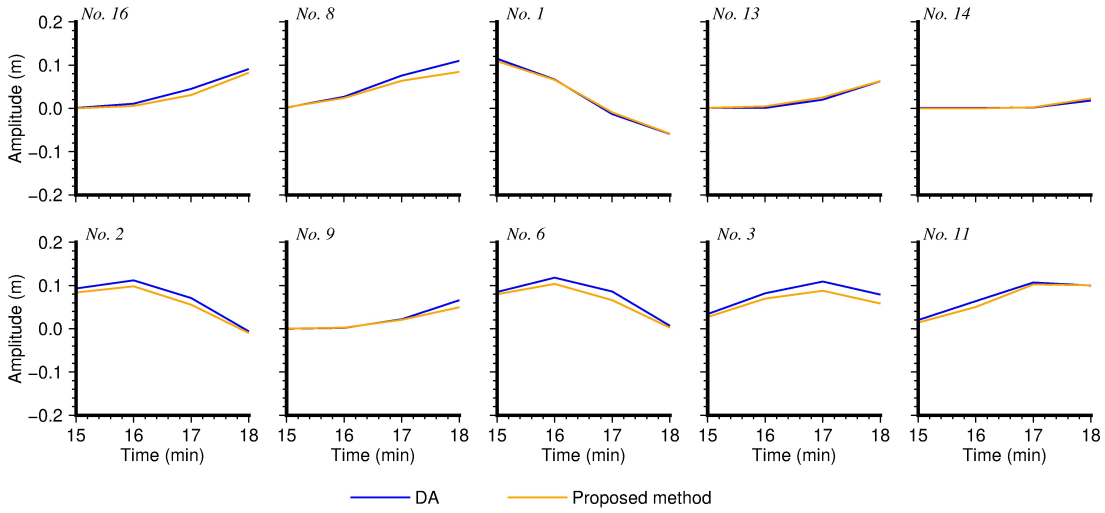


Figure 5.6: Comparisons of waveforms between the proposed method and DA at randomly-selected stations for the simple bathymetry case

plotted in Fig. 5.3. Overall, the forecasted waveforms were almost identical to the waveforms estimated by the DA with a mean correlation coefficient of 0.995. The figure shows that the DA (Fig. 5.4c) provided a good wavefield approximation in the vicinity of the observation points, though a broader coverage of the stations may be necessary to improve the quality of the assimilated wavefield, as exhibited in the forward modeling results (Fig. 5.4d). However, here we only focused on the performance of the proposed model over the DA.

### 5.3.2 The 2011 Tohoku tsunami

Next, we applied the proposed method to the tsunami induced by the 2011 Tohoku earthquake. We used bathymetry data with a relatively coarse resolution of 4050 m (Fig. 5.7a). The bathymetry dataset, which was obtained from the Cabinet Office of Japan, is based on a nautical chart and digital data compiled by the Japan Coast Guard and the Japan Hydrographic Association.

For model training, we arranged multiple scenarios for simple rectangular fault models. We set 15 reference points as the top-center of the faults. The placement of the reference points is shown in Fig. 5.7b. We set an earthquake magnitude ranging from 8.0 to 9.0 (0.2 intervals); in total, there were 90 scenarios. The earthquake depth, strike and dip angle were determined based on SLAB 2.0 (Hayes et al., 2018), while the rake angle was set to 90° for all scenarios, representing the thrust fault mechanism. To calculate the area of the fault, the magnitude scale relation for the plate-boundary proposed by Murotani et al. (2013) (Eq. 2.1) was

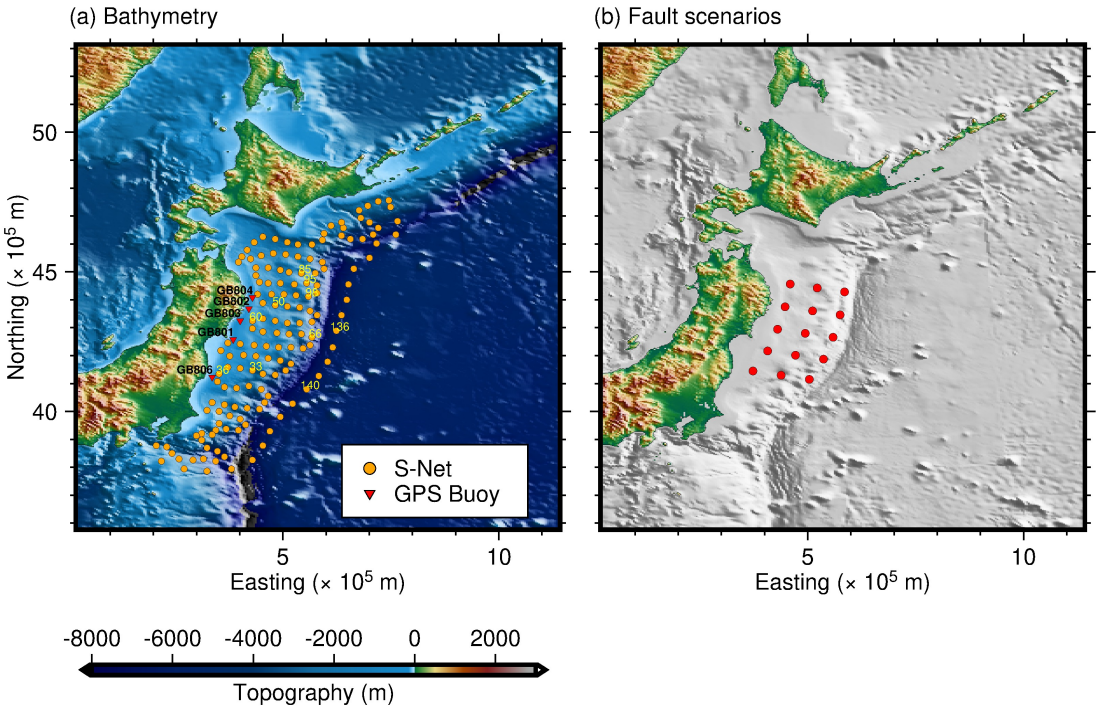


Figure 5.7: (a) Bathymetry data and the locations of S-Net and GPS buoys stations; (b) Top-center of the fault scenarios to develop the database

used. We used a coseismic deformation in an elastic half-space model (Okada, 1985), to compute the initial sea surface for the DA. Similar to the simple case, the training epoch was set to 350. For model testing, we used a source model of the 2011 Tohoku earthquake (Gusman et al., 2012). The slip distribution was calculated by conducting a joint inversion using a tsunami, GPS and seafloor deformation data.

A comparison between the predictions, DA and forward modeling is shown in Fig. 7. In this case, the DA process started at $t = 1$ min. We used four frames of the assimilated wavefield from $t = 1$ to 4 min (Fig. 5.8a) as the input to the model to predict the next four frames of the wavefield ($t = 5$ to 8 min). The results show that the predictions (Fig. 5.8b) are very similar to the DA (Fig. 5.8c) with SSIM and RMSE values ranging from 0.949 to 0.955 and 0.173 to 0.196, respectively. We further explored the capability of the proposed method by recursively feeding back the prediction into the model to provide longer wavefield predictions up to t = 36 min. We show four snapshots of the resulting forecasts at $t = 14$, 21, 28 and 35 min (Fig. 5.9). In Fig. 5.11, we also compared the assimilated and forecasted waveforms from ten randomly-selected S-Net stations and with real waveform data from the 2011 Tohoku tsunami recorded at five GPS buoys (GB801, GB802, GB803, GB804, GB806). The location of the GPS buoys and selected observation stations are shown in Fig. 5.7a. At ten S-Net stations, the forecasted waveforms

show reasonably good agreement with the DA, with a mean correlation coefficient of 0.748. However, both the assimilated and forecasted waveforms underestimated the observations at the GPS buoys. Nonetheless, both exhibit similar trends to the observations.

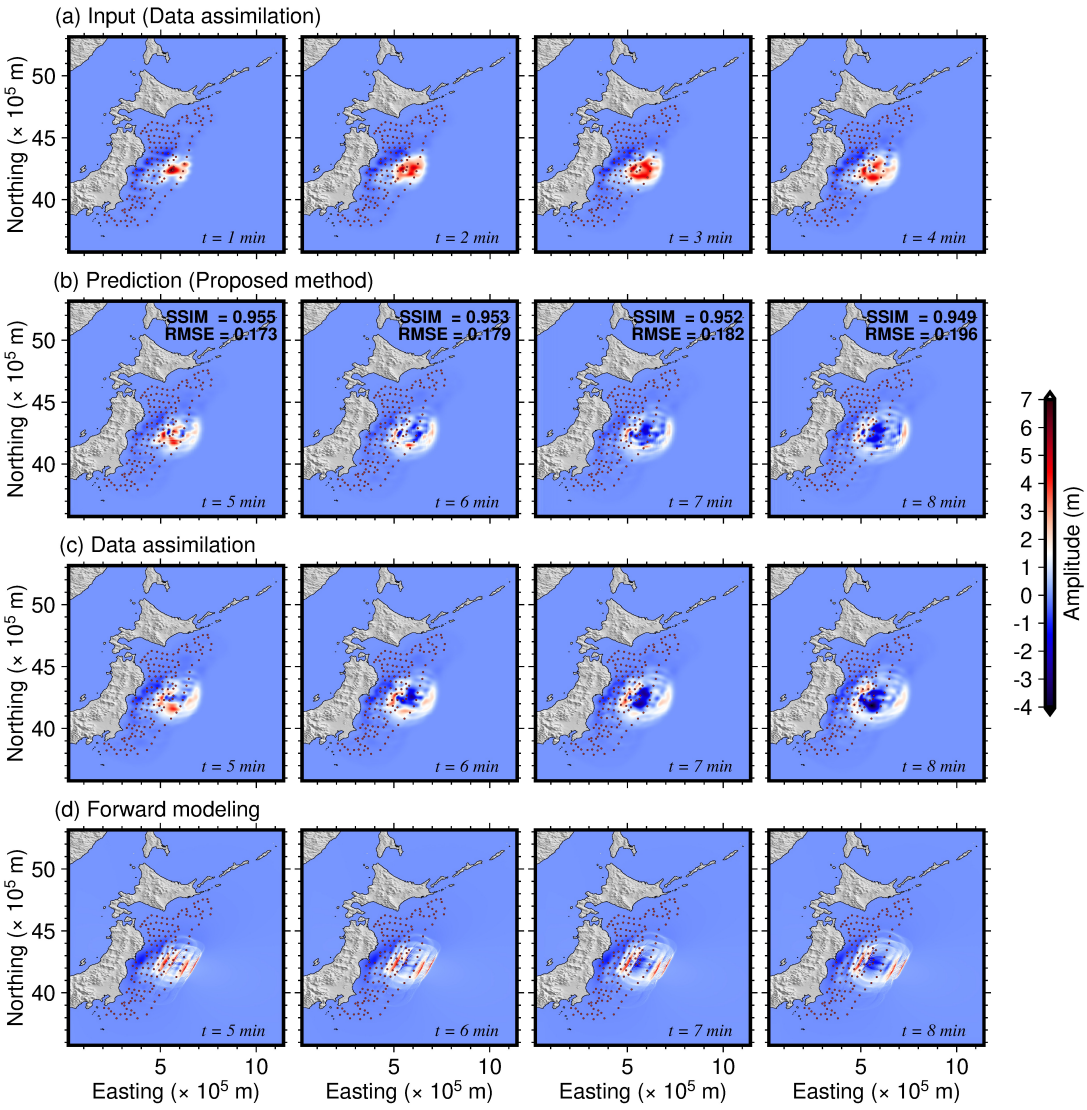


Figure 5.8: Comparisons of the wavefields for the model input and the estimated wavefields from the proposed method, DA and forward modeling for the 2011 Tohoku tsunami. (a) Input to the model; (b) Forecasted tsunami wavefields; (c) Assimilated tsunami wavefields; (d) Results of forward modeling

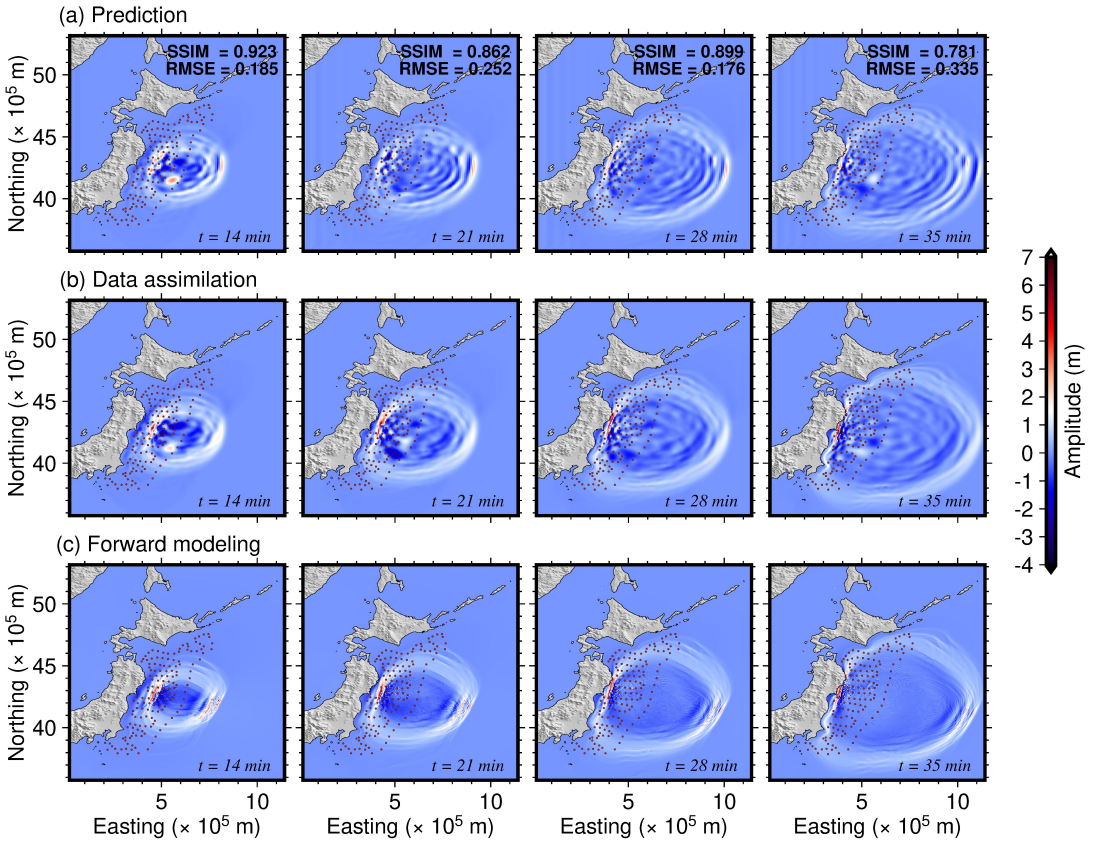


Figure 5.9: Comparisons of the estimated wavefields from the proposed method, DA and forward modeling for the 2011 Tohoku tsunami at t = 14, 21, 28 and 35 min. (a) Forecasted tsunami wavefields; (b) Assimilated tsunami wavefields; (c) Results of forward modeling

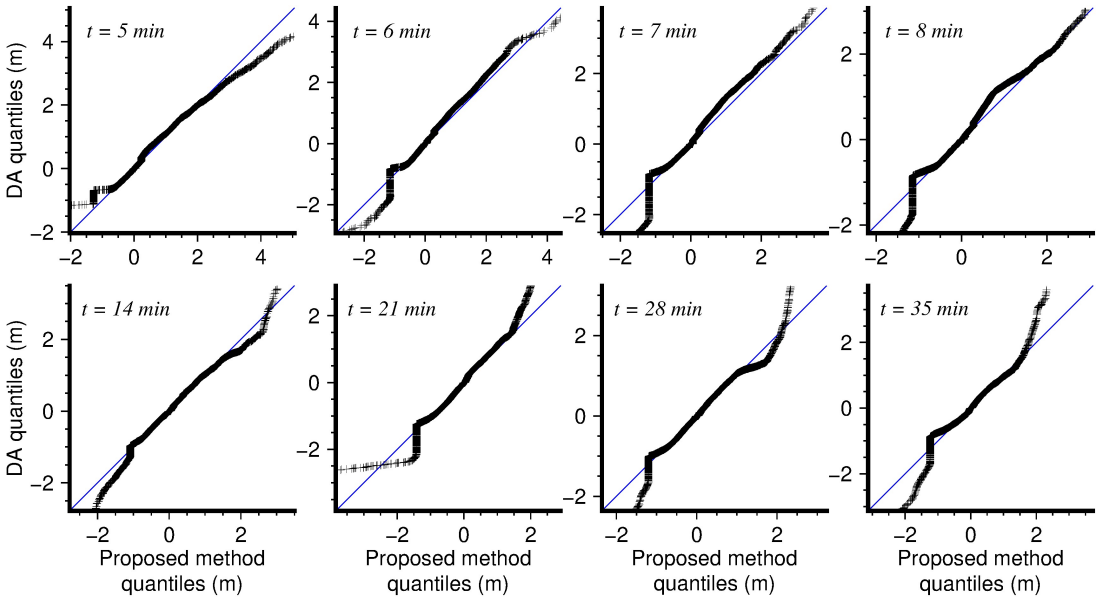


Figure 5.10: Q-Q plots between the proposed method and DA for the 2011 Tohoku tsunami

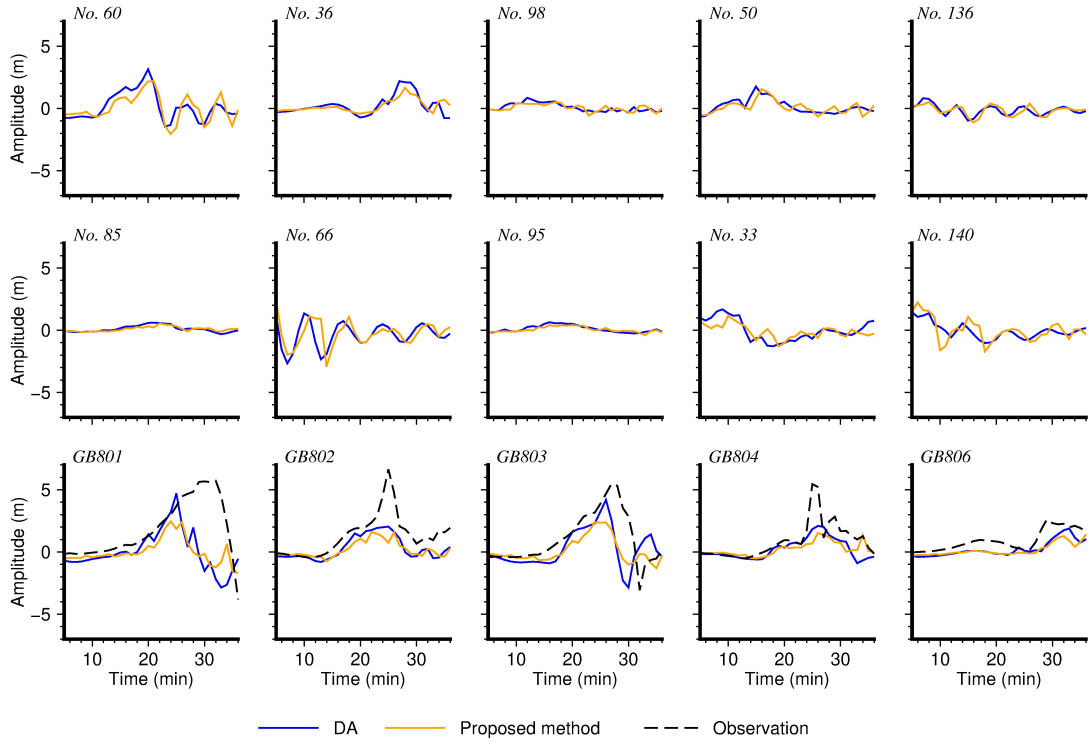


Figure 5.11: Comparisons of the waveforms between the proposed method, DA and observations at GPS buoys and randomly-selected stations for the 2011 Tohoku tsunami

## 5.4 Discussion

Computational speed is one of the most critical factors for real-time tsunami forecasting. In the previous studies (Gusman et al., 2016, Maeda et al., 2015, Yang et al., 2019), tsunami DA has successfully provided accurate results at a relatively high computational cost. The predictive coding network learns the pattern of tsunami propagation during the training period. Once the model has been trained, the spatiotemporal tsunami wavefield prediction can be made quickly by only performing a matrix multiplication procedure. We used a personal computer equipped with an Intel i7 processor, an 8-gigabyte graphics processing unit (GPU), and 16 gigabytes of memory for model training and testing. Computationally, generating four frames of future wavefield predictions utilizing four frames of the assimilated wavefield as the input requires a computational time of 0.2 sec. The computational time to obtain the input (four frames of DA-generated wavefields) is 1.38 min. In total, it only requires 1.38 min and 1.6 sec to provide wavefield predictions from $t = 1$ to 36 min in the case of the 2011 Tohoku earthquake, while the DA requires about 7 min. The comparison of computational time between DA and the proposed method for the 2011 Tohoku tsunami

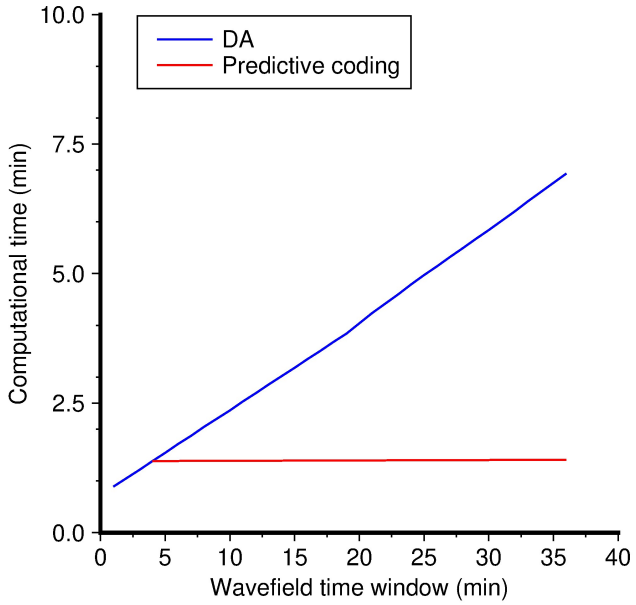


Figure 5.12: Comparisons of the computational time between the proposed method and DA for the 2011 Tohoku tsunami

is plotted in Fig. 5.12. Furthermore, by using a finer grid, the DA may require a more significantly high computational cost. Therefore, with this quick computation time, we can provide immediate warnings, which is very important for the evacuation process.

In the original DA, the tsunami model is based on LLW theory. Even though incorporating nonlinearity or a dispersive effect may improve the quality of the DA, this would be better avoided, as it may further increase the computational cost. Since the learning process of the proposed method is based on the database, incorporating those scenarios is more practical, because the tsunami simulation is conducted in advance.

For the case of the 2011 Tohoku tsunami, both the proposed method and DA-generated waveforms at the GPS buoys underestimate the observations (Fig. 10). With the limited memory capacity of our standard GPU, we decided to use a relatively coarse bathymetry resolution. As a result, a high accuracy forecasting result may not be achieved in this study, because, as explained in previous studies (Gusman et al., 2009, Satake, 1995), the forecast accuracy is strongly dependent on the topography resolution. A more sophisticated GPU should be used in future studies to accommodate a finer bathymetry resolution. In addition, since the error propagates over time steps, the optimum length of future predictions should be carefully investigated in future work. It is clear from Figs. 5.4b, 5.8b,

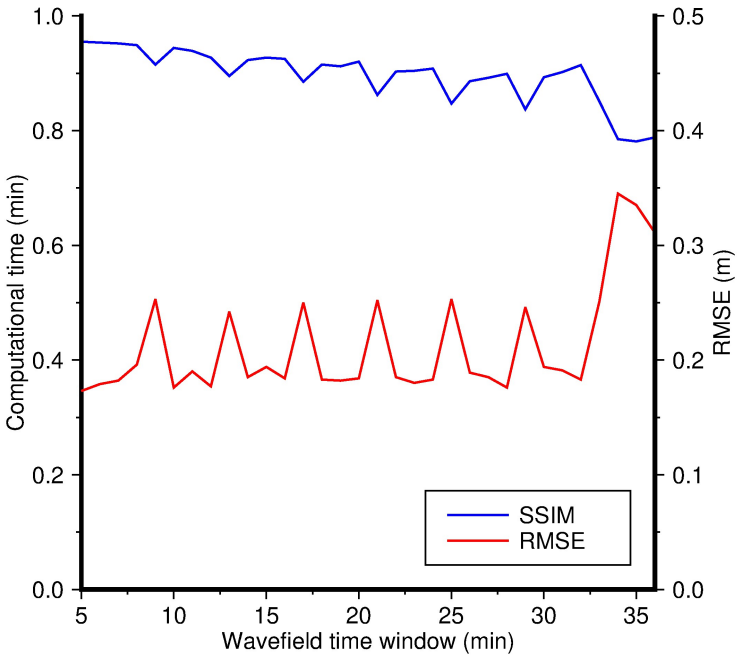


Figure 5.13: The SSIM and RMSE results over the time step for the 2011 Tohoku tsunami case

5.9a, and 5.13 that the SSIM and RMSE tend to degrade over the time steps. The degradation is also shown in Q-Q plots (Fig. 5.10), where the outliers are more apparent at the longer time steps of the predictions. Overall, based on the results, the proposed network shows promise for integration with DA to reduce the computational cost.

## 5.5 Summary

We conducted a study using a deep predictive coding network along with the DA to forecast a tsunami wavefield in real-time. The objective of this research was to assess whether the application of a deep predictive coding network combined with the DA could be implemented for a real-time warning system. We conducted two study cases: simple bathymetry and the 2011 Tohoku tsunami. The results showed that only utilizing four frames of the assimilated wavefields enabled the model to satisfactorily forecasted the next four frames of the wavefield with SSIM values in the range 0.891–0.960, and up to 32 future frames with SSIM values in the range 0.781–0.955 for the simple bathymetry and the 2011 Tohoku tsunami, respectively. With a quick computational time and reasonably accurate results, it is concluded that the proposed method is applicable for a real-time warning

system. In the future, a more advanced GPU with a higher memory capacity should be used to accommodate finer bathymetry, so that the higher prediction accuracy can be obtained.

# References

Baba, T., Takahashi, N., and Kaneda, Y. (2014). Near-field tsunami amplification factors in the Kii Peninsula, Japan for Dense Oceanfloor Network for Earthquakes and Tsunamis (DONET). *Marine Geophysical Research*, 35(3):319–325.

Clevert, D.-A., Unterthiner, T., and Sepp, H. (2016). Fast and accurate deep network learning by exponential linear units (ELUs). In *International Conference on Learning Representations*.

Friston, K. and Kiebel, S. (2009). Predictive coding under the free-energy principle. *Philosophical Transactions of the Royal Society B: Biological Sciences*, 364:1211–1221.

Gusman, A. R., Sheehan, A. F., Satake, K., Heidarzadeh, M., Mulia, I. E., and Maeda, T. (2016). Tsunami data assimilation of Cascadia seafloor pressure gauge records from the 2012 Haida Gwaii earthquake. *Geophysical Research Letters*, 43(9):4189–4196.

Gusman, A. R., Tanioka, Y., Macinnes, B. T., and Tsushima, H. (2014). A methodology for near-field tsunami inundation forecasting: Application to the 2011 Tohoku tsunami. *Journal of Geophysical Research: Solid Earth*, 119(11):8186–8206.

Gusman, A. R., Tanioka, Y., Matsumoto, H., and Iwasaki, S. I. (2009). Analysis of the Tsunami generated by the great 1977 Sumba earthquake that occurred in Indonesia. *Bulletin of the Seismological Society of America*, 99(4):2169–2179.

Gusman, A. R., Tanioka, Y., Sakai, S., and Tsushima, H. (2012). Source model of the great 2011 Tohoku earthquake estimated from tsunami waveforms and crustal deformation data. *Earth and Planetary Science Letters*, 341-344:234–242.

Hayes, G. P., Moore, G. L., Portner, D. E., Hearne, M., Flamme, H., Furtney, M., and Smoczyk, G. M. (2018). Slab2, a comprehensive subduction zone geometry model. *Science*, 362(6410):58–61.

Heidarzadeh, M., Wang, Y., Satake, K., and Mulia, I. E. (2019). Potential deployment of offshore bottom pressure gauges and adoption of data assimilation for tsunami warning system in the western Mediterranean Sea. *Geoscience Letters*, 6(19).

Hinton, G. E., Srivastava, N., and Swersky, K. (2012). Neural Networks for Machine Learning Lecture 6a Overview of mini-batch gradient descent.

Hochreiter, S. and Schmidhuber, J. (1997). Long Short-Term Memory. *Neural Computation*, 9(8):1735–1780.

Hossen, M. J., Cummins, P. R., Dettmer, J., and Baba, T. (2015). Time reverse imaging for far-field tsunami forecasting: 2011 Tohoku earthquake case study. *Geophysical Research Letters*, 42(22):9906–9915.

Kalnay, E. (2002). *Atmospheric Modeling, Data Assimilation and Predictability.*

Kaneda, Y., Kawaguchi, K., Araki, E., Matsumoto, H., Nakamura, T., Kamiya, S., Ariyoshi, K., Hori, T., Baba, T., and Takahashi, N. (2015). Development and application of an advanced ocean floor network system for megathrust earthquakes and tsunamis. In *Seafloor Observatories: A New Vision of the Earth from the Abyss.*

Lotter, W., Kreiman, G., and Cox, D. (2017). Deep predictive coding networks for video prediction and unsupervised learning. In *5th International Conference on Learning Representations, ICLR 2017 - Conference Track Proceedings.*

Maeda, T., Obara, K., Shinohara, M., Kanazawa, T., and Uehira, K. (2015). Successive estimation of a tsunami wavefield without earthquake source data: A data assimilation approach toward real-time tsunami forecasting. *Geophysical Research Letters*, 42:7923–7932.

Mulia, I. E., Asano, T., and Nagayama, A. (2016). Real-time forecasting of near-field tsunami waveforms at coastal areas using a regularized extreme learning machine. *Coastal Engineering*, 109:1–8.

Mulia, I. E., Gusman, A. R., and Satake, K. (2018). Alternative to non-linear model for simulating tsunami inundation in real-time. *Geophysical Journal International*, 214:2002–2013.

Mulia, I. E., Inazu, D., Waseda, T., and Gusman, A. R. (2017). Preparing for the Future Nankai Trough Tsunami: A Data Assimilation and Inversion Analysis From Various Observational Systems. *Journal of Geophysical Research: Oceans*, 122(10):7924–7937.

Murotani, S., Satake, K., and Fujii, Y. (2013). Scaling relations of seismic moment, rupture area, average slip, and asperity size for M-9 subduction-zone earthquakes. *Geophysical Research Letters*, 40(19):5070–5074.

Okada, Y. (1985). Surface deformation due to shear and tensile faults in a half-space. *Bulletin of the Seismological Society of America*, 75(4):1135–1154.

Rao, R. P. and Ballard, D. H. (1999). Predictive coding in the visual cortex: A functional interpretation of some extra-classical receptive-field effects. *Nature Neuroscience*.

Saito, T., Satake, K., and Furumura, T. (2010). Tsunami waveform inversion including dispersive waves: The 2004 earthquake off Kii Peninsula, Japan. *Journal of Geophysical Research: Solid Earth*, 115(B6).

Satake, K. (1989). Inversion of tsunami waveforms for the estimation of heterogeneous fault motion of large submarine earthquakes: the 1968 Tokachi-oki and 1983 Japan Sea earthquakes. *Journal of Geophysical Research*, 94(B5):5627–5636.

Satake, K. (1995). Linear and nonlinear computations of the 1992 Nicaragua earthquake tsunami. *Pure and Applied Geophysics*, 144((3-4)):455–470.

Satake, K. (2015). Geological and historical evidence of irregular recurrent earthquakes in Japan.

Setiyono, U., Gusman, A. R., Satake, K., and Fujii, Y. (2017). Pre-computed tsunami inundation database and forecast simulation in Pelabuhan Ratu, Indonesia. *Pure and Applied Geophysics*, 178(8):3219–3235.

Shi, X., Chen, Z., Wang, H., Yeung, D. Y., Wong, W. K., and Woo, W. C. (2015). Convolutional LSTM network: A machine learning approach for precipitation nowcasting. In *Advances in Neural Information Processing Systems*.

Theis, L., Van Den Oord, A., and Bethge, M. (2016). A note on the evaluation of generative models. In *4th International Conference on Learning Representations, ICLR 2016 - Conference Track Proceedings*.

Titov, V. V., González, F. I., Bernard, E. N., Eble, M. C., Mofjeld, H. O., Newman, J. C., and Venturato, A. J. (2005). Real-time tsunami forecasting: Challenges and solutions. In *Developing Tsunami-Resilient Communities: The National Tsunami Hazard Mitigation Program*, pages 41–58.

Tsushima, H., Hirata, K., Hayashi, Y., Tanioka, Y., Kimura, K., Sakai, S., Shinohara, M., Kanazawa, T., Hino, R., and Maeda, K. (2011). Near-field tsunami forecasting using offshore tsunami data from the 2011 off the Pacific coast of Tohoku Earthquake. *Earth, Planets and Space*, 63(56):821–826.

Wang, X., Zhang, W., Wu, X., Xiao, L., Qian, Y., and Fang, Z. (2019). Real-time vehicle type classification with deep convolutional neural networks. *Journal of Real-Time Image Processing*, 16(1):5–14.

Wang, Y., Satake, K., Maeda, T., and Gusman, A. R. (2017). Green's Function-Based Tsunami Data Assimilation: A Fast Data Assimilation Approach Toward Tsunami Early Warning. *Geophysical Research Letters*, 44(10):10282–10289.

Wang, Z., Bovik, A. C., Sheikh, H. R., and Simoncelli, E. P. (2004). Image quality assessment: From error visibility to structural similarity. *IEEE Transactions on Image Processing*, 13(4):600 – 612.

Yamamoto, N., Aoi, S., Hirata, K., Suzuki, W., Kunugi, T., and Nakamura, H. (2016). Multi-index method using offshore ocean-bottom pressure data for real-time tsunami forecast 4. Seismology. *Earth, Planets and Space*, 68.

Yang, Y., Dunham, E. M., Barnier, G., and Almquist, M. (2019). Tsunami Wavefield Reconstruction and Forecasting Using the Ensemble Kalman Filter. *Geophysical Research Letters*, 46(2):853–860.

# Chapter 6

# Discussion and Conclusion

This study evaluates the applications of the database and machine learning algorithms to forecast tsunami inundation, waveforms, and wavefields. Currently, conducting numerical tsunami simulation in real-time shortly after a submarine earthquake occurs is still the best method to estimate the tsunami. However, during a short golden period, conducting forward modeling is numerically expensive. Several approaches have been developed and investigated here to minimize the computational cost of predicting the tsunami and therefore to speed-up the early-warning process in TEWS. The first part of this study (Chapter 2) presents the early development of the database-based tsunami inundation forecasting system. The proposed methods in the second part of the thesis (Chapter 3) improves the matching algorithm in the first proposed method in Chapter 2 by integrating machine learning frameworks into the system. The proposed methods in Chapter 2 and Chapter 3 have the same aim that is to forecast tsunami inundation. The proposed methods in the third part of the thesis (Chapter 4) uses a variant of ELM and SVM as alternatives to TWI method to predict tsunami waveforms. The last part of the thesis (Chapter 5) introduces a hybrid data assimilation and deep predictive coding network for spatiotemporal prediction of tsunami wavefield. Overall, all of the proposed methods are strong candidates for TEWS to provide quick information of tsunami inundation, waveforms, and wavefields in a real event.

All proposed methods are not intended to be compared with each other, but as integral parts of TEWS. The first part of this study (Chapter 2) discussed the possibility of utilizing tsunami inundation and tsunami waveforms to forecast tsunami inundation in real-time. A database that consists of tsunami inundation

and waveforms from 328 predefined fault scenarios has been developed. Three earthquake models: one past earthquake and two predicted future earthquakes, are used to test the model performance. The 1944 Tonankai earthquake represents the past earthquake, and the Tokai-Tonankai and Nankai Megathrust earthquakes represent the predicted future earthquakes. The Stage 1 of the proposed method can quickly predict the tsunami inundation, because it only requires the information of earthquake magnitude and epicenter location, which can be obtained in a short time after an earthquake occurs. Even though it can be done quickly, the tsunami inundation prediction from Stage 1 overestimates the forward modeling as exhibited in the 1944 Tonankai case. It indicates that only by using the earthquake magnitude and location is not enough to generate a reliable tsunami inundation forecast. Nevertheless, the Stage 1 is important in a real event to provide a quick tsunami estimation. As the earthquake information is usually revised over the time until seismologist determine the fixed information, the Stage 1 can be conducted repeatedly when a new preliminary earthquake information is available. In the Stage 2, linear tsunami simulation is performed when fixed earthquake information or source model is available. The best-fit scenario is selected by minimizing error between simulated and precomputed waveforms, then the corresponding tsunami inundation is assummed to be the inundation prediction. For the 1944 Tonankai earthquake case, the Stage 2 successfully improves the accuracy of the prediction from the Stage 1. The predicted maximum tsunami inundation depth (2.74 m) is very similar to the field survey (2.80 m) as well as forward modeling (2.62 m).

In the second part of the study (Chapter 3), two machine learning models (CNN and MLP) are proposed to improve the matching algorithm in Chapter 2 and also in previous studies (Gusman et al., 2014, Mulia et al., 2018). In the previous part, manual time shifting procedure is necessary due to the difference of wave-phase between simulated and precomputed waveforms in order to find the best-fit scenario. The concept of the CNN is similar to the method proposed by Mulia et al. (2018), which selects the best-fit scenario in the database based on similarity pattern between computed and precomputed maximum tsunami amplitude in the low-resolution grid. The difference is that the pattern recognition in the previous study is conducted by using principal component analysis, a conventional dimensionality reduction algorithm, while the dimensionality reduction is performed within the convolutional and pooling layers of a CNN in this study. Because the database is developed from limited simple fault scenarios, there is a possibility that the CNN is unable to find the appropriate best-fit scenario, as shown for Owase. However, the MLP, which is purposed for the regression task,

is able to yield a more acceptable forecast than CNN when there is no scenario in the database that has a pattern similar to that produced by direct forward modeling. Both methods are faster (0.069 and 0.084 for CNN and MLP, respectively) than the matching algorithm in Chapter 2, which requires several seconds due to the time-shifting procedure.

In Chapter 2 and Chapter 3, an accurate and reliable tsunami source models is necessary as the input for linear forward modeling in order to find the best-fit scenario in database. Based on the 2011 Tohoku earthquake, fixed earthquake information can be obtained at 20 min after the earthquake. In the case of Nankai region, this required time is too long because it is expected that tsunami induced by Nankai Megathrust would reach the coast of Owase within less than 20 min. Due to the short distance between the Nankai Trough and the nearby Japanese coast, a fast and reliable tsunami source model is needed. Tsunami source estimation from Real Time Kinematic (RTK) GPS (Ohta et al., 2012), waveform inversion (Tsushima et al., 2009), and W-phase inversion Gusman and Tanioka (2013) are promising methods for integration with the proposed methods. In the future, further development should focus on improving the reliability of the database by incorporating more scenarios. This can be done by including well-verified tsunami sources from previous events, such as the 1701 Hoei (Furumura et al., 2011), the 1944 Tonankai (Baba et al., 2006), and the 1946 Nankai earthquake (Murotani et al., 2015). Incorporating the influence of tides (Lee et al., 2015) and uncertainties from stochastic earthquake source models (Goda et al., 2018) are also suggested. Despite of the high computational cost, dispersive tsunami model successfully reproduce the soliton fission along Sendai coast during the 2011 Tohoku earthquake (Baba et al., 2015). With U-shape topography, Owase is also subjected to experience soliton effect (Yamanaka et al., 2016); therefore, applying dispersive terms in nonlinear tsunami tsunami model may enhance the quality of the database. The network architecture of CNN and MLP may also need to be improved to accommodate more input variables, such as tsunami height at observation stations, to produce a better forecast.

The third part of this study (Chapter 4) presents an application of data-driven models including, PRELM, PRELM-FT, and SVM for robust forecasting of tsunami waveform in real-time. The proposed methods are purposed to provide a quick estimation of tsunami waveforms at observational stations. Furthermore, the estimated waveforms is useful as the input of the matching algorithm in Stage 2 in Chapter 2. The basic idea of the PRELM is similar to the method proposed by Mulia et al. (2016), which also uses an ELM variant. The difference

is that the input parameters of the previous study are randomly assigned, while the input parameters in this study are then iteratively-optimized by using Adam optimizer. Consequently, in the previous study, each model run would produce a different prediction which may not be suitable for early warning tasks. In addition to producing a quick and accurate prediction, the TEWS also requires a consistent prediction to avoid confusion during a real event. With fully-trained network parameters, the PRELM-FT can yield a better forecast with a significant improvement than PRELM. PRELM-FT is also superior to TWI and another popular data-driven model, SVM, indicated by the highest rank in two earthquake cases. However, due to the iteration procedure during the optimization, the PRELM-FT requires more computational time. In terms of waveform forecasting accuracy, PRELM shows the best performance; however, in terms of maximum tsunami height accuracy, SVM outperforms the other methods. Therefore, with faster training time than PRELM-FT, SVM is also a promising method for future tsunami waveform forecasting tool. Overall, PRELM-FT and SVM are strong candidates for the future TEWS tool by considering its good approximation. In the future, we should focus on improving the performance of the method by using a more sophisticated procedure in selecting and developing the Green's function. In this study, the unit sources included in the inversion are determined by limiting the unit sources with a certain radius with the earthquake coordinate as the center. However, this method may not represent the actual coseismic deformation as the epicenter of the earthquake is not always at the center of the deformation area. Therefore, incorporating a fast optimization procedure to select the unit sources is suggested for future development. Both of the 2004 Kii and 2011 Tohoku earthquake exhibit dispersive effects, as presented in the previous study (Saito et al., 2014, 2010). Even though it requires a high computational load, applying a dispersive model in developing the Green's function database may provide more accurate predictions.

In the last part of this study (Chapter 5), a hybrid DA and deep predictive coding network is proposed for real-time spatiotemporal tsunami wavefields prediction. Tsunami wavefields can be assummed as tsunami source for linear tsunami model, which is essensial for the proposed methods in Chapter 2 and Chapter 3. The extracted waveforms from tsunami wavefields also useful as the input of matching algorithm in the Stage 2 (Chapter 2). Therefore, a quick estimation of tsunami wavefield is a step forward for real-time tsunami inundation forecasting. Currently, DA is a promising tool to estimate tsunami in real-time, as it directly assimilates tsunami wavefields from the observed tsunami height at dense observational stations. However, DA requires a high computational load due to

the direct tsunami simulation within the model. Therefore, in this study, DA is coupled with the deep predictive coding network to speed-up the spatiotemporal predictions of tsunami wavefields. The idea is that by using a short sequence of DA-assimilated wavefield, then the predictive coding can forecast the future sequence of tsunami wavefields. To be noted that the tsunami wavefields predicted by the deep predictive coding network are independent from the DA. Similar to the CNN and MLP methods, the deep predictive coding network should be trained in advance with multiple predefined scenarios. We conducted two study cases: simple bathymetry and the 2011 Tohoku tsunami. At first, the deep predictive coding network is trained, in which with four frames of input, the model will able to predict the next four frames. The results showed that only utilizing four frames of the assimilated wavefields enabled the model to satisfactorily forecasted the next four frames of the wavefield with SSIM values in the range 0.891–0.960 for the simple bathymetry case. However, the length of the predictions are not sufficient for TEWS as longer predictions is better to estimate tsunami characteristics (height and propagation) near the coasts. Furthermore, by recursively feeding back the predictions as the input, the model is able to forecast longer sequence of tsunami wavefields. By using four frames of assimilated wavefields, the model successfully estimates up to 32 future frames with SSIM values in the range 0.781–0.955 for the 2011 Tohoku tsunami case. The predictions of 32 frames can be conducted quickly (1.6 s), while the original DA requires computational time of about 30 min. With a quick computational time and reasonably accurate results, it is concluded that the proposed method is applicable for a real-time warning system. In the future, a more advanced GPU with a higher memory capacity should be used to accommodate finer bathymetry, so that the higher prediction accuracy can be obtained.

Principally, the concept of TEWS in this study is similar to the JMA's system. Kamigaichi (2015) explained that JMA's TEWS utilizes rapid estimation of seismic waves recorded at seismic network to calculate preliminary earthquake parameters (magnitude, depth, latitude, and longitude). The earthquake parameters then are used as the input of the system, in which tsunami estimation (maximum tsunami amplitude and arrival time) is conducted by linearly interpolated precomputed tsunami database from a large set of fault scenarios. This procedure takes a computational time as quick as 3 min. When a fixed earthquake parameters are available, the tsunami prediction is revised. These procedures are similar to the Stage 1 and Stage 2 in Chapter 2. To find out the best-fit scenario, JMA's system interpolates the adjacent scenarios around the epicenter. In this study, the best-fit scenario can be selected by conducting two procedures. The

first one is by comparing simulated and precomputed tsunami waveforms at virtual observational stations (Chapter 2), and by using CNN to find the maximum tsunami amplitude in database that similar to the simulated one (Chapter 3). However, tsunami generation is an uncertainty process, in which it is strongly influenced by topography and initial seafloor deformation. By only considering simple fault scenarios in developing the database, the selected tsunami inundation may not provide a reliable result. This problem is also exhibited in Chapter 3, in which the selected best-fit scenario by CNN is underestimate the forward modeling due to the limited tsunami database. To solve this problem, MLP is used. Unlike CNN and matching algorithm in Chapter 2 which select the best-fit scenario in database as a tsunami inundation forecast, MLP generates the tsunami inundation based on learned knowledge during the training process. Therefore, the prediction results are unique and independent from the database.

Finally, all the proposed methods are promising forecasting tools to be integrated in TEWS. The database-based tsunami inundation forecasting system developed in Chapter 2 is able to generate tsunami inundation forecast which shows a good agreement with the field survey, even though a more scenarios in database is required for more reliable prediction. Furthermore, CNN in Chapter 3 is proposed as a subsitute of matching algorithm in the Chapter 2 with a faster computational time. Since the tsunami database is developed based on simple rectangular fault scenarios, and by the fact that the seafloor deformation caused by a submarine earthquake is strongly nonlinear, the best-fit scenario selected from the database may not represent the actual condition of tsunami inundation. In such a condition, MLP successfully produce a more reliable forecast, because MLP learns the characteristics of tsunami inundation during the training process. Therefore, even though the database is limited, the MLP may produce a better forecast than CNN and matching algorithm in Chapter 2. To provide tsunami waveforms at the virtual observational points in Chapter 2, PRELM-FT and SVM are proposed in Chapter 4. Both methods outperforms TWI in terms of computational time and waveforms accuracy. In Chapter 5, a coupled method between DA and deep predictive coding network may provide tsunami waveforms at virtual observation points, which is necessary in Chapter 2, and maximum tsunami amplitude at low-resolution grid, which is required in Chapter 3. Combining the deep predictive coding network with the DA has successfully reduce the computational cost required for spatiotemporal tsunami wavefields prediction with a satisfactorily results.

# References

Baba, T., Cummins, P. R., Hori, T., and Kaneda, Y. (2006). High precision slip distribution of the 1944 Tonankai earthquake inferred from tsunami waveforms: Possible slip on a splay fault. *Tectonophysics*, 426:119–134.

Baba, T., Takahashi, N., Kaneda, Y., Ando, K., Matsuoka, D., and Kato, T. (2015). Parallel Implementation of Dispersive Tsunami Wave Modeling with a Nesting Algorithm for the 2011 Tohoku Tsunami. *Pure and Applied Geophysics*, 172(12):3455–3472.

Furumura, T., Imai, K., and Maeda, T. (2011). A revised tsunami source model for the 1707 Hoei earthquake and simulation of tsunami inundation of Ryujin Lake, Kyushu, Japan. *Journal of Geophysical Research: Solid Earth*, 116(B02308).

Goda, K., Yasuda, T., Mai, P. M., Maruyama, T., and Mori, N. (2018). Tsunami simulations of mega-thrust earthquakes in the Nankai–Tonankai Trough (Japan) based on stochastic rupture scenarios. *Geological Society, London, Special Publications*, 456.

Gusman, A. R. and Tanioka, Y. (2013). W Phase Inversion and Tsunami Inundation Modeling for Tsunami Early Warning: Case Study for the 2011 Tohoku Event. *Pure and Applied Geophysics*, 171(7):1409–1422.

Gusman, A. R., Tanioka, Y., Macinnes, B. T., and Tsushima, H. (2014). A methodology for near-field tsunami inundation forecasting: Application to the 2011 Tohoku tsunami. *Journal of Geophysical Research: Solid Earth*, 119(11):8186–8206.

Kamigaichi, O. (2015). Tsunami Forecasting and Warning. In *Encyclopedia of Complexity and Systems Science*.

Lee, H. S., Shimoyama, T., and Popinet, S. (2015). Impacts of tides on tsunami propagation due to potential Nankai Trough earthquakes in the Seto Inland Sea, Japan. *Journal of Geophysical Research: Oceans*, 120(10):6865–6883.

Mulia, I. E., Asano, T., and Nagayama, A. (2016). Real-time forecasting of near-field tsunami waveforms at coastal areas using a regularized extreme learning machine. *Coastal Engineering*, 109:1–8.

Mulia, I. E., Gusman, A. R., and Satake, K. (2018). Alternative to non-linear model for simulating tsunami inundation in real-time. *Geophysical Journal International*, 214:2002–2013.

Murotani, S., Shimazaki, K., and Koketsu, K. (2015). Rupture process of the 1946 Nankai earthquake estimated using seismic waveforms and geodetic data. *Journal of Geophysical Research: Solid Earth*, 120(8):5677–5692.

Ohta, Y., Kobayashi, T., Tsushima, H., Miura, S., Hino, R., Takasu, T., Fujimoto, H., Iinuma, T., Tachibana, K., Demachi, T., Sato, T., Ohzono, M., and Umino, N. (2012). Quasi real-time fault model estimation for near-field tsunami forecasting based on RTK-GPS analysis: Application to the 2011 Tohoku-Oki earthquake (Mw9.0). *Journal of Geophysical Research: Solid Earth*, 117:B02311.

Saito, T., Inazu, D., Miyoshi, T., and Hino, R. (2014). Dispersion and nonlinear effects in the 2011 Tohoku-Oki earthquake tsunami. *J. Geophys. Res. Oceans*, 119:5160–5180.

Saito, T., Satake, K., and Furumura, T. (2010). Tsunami waveform inversion including dispersive waves: The 2004 earthquake off Kii Peninsula, Japan. *Journal of Geophysical Research: Solid Earth*, 115(B6).

Tsushima, H., Hino, R., Fujimoto, H., Tanioka, Y., and Imamura, F. (2009). Near-field tsunami forecasting from cabled ocean bottom pressure data. *Journal of Geophysical Research: Solid Earth*, 114:B06309.

Yamanaka, Y., Sato, S., Tajima, Y., and Shimozono, T. (2016). A study on soliton fission of Nankai trough tsunami. *Journal of Japan Society of Civil Engineers, Ser. B2.*, 72(2):I_403–I_408.